INVESTIGATION OF THE MECHANISMS OF FLASH SINTERING IN OXIDE

CERAMICS

by

HARRY CHARALAMBOUS

A dissertation submitted to the

School of Graduate Studies

Rutgers, The State University of New Jersey

In partial fulfillment of the requirements

For the degree of

Doctor of Philosophy

Graduate Program in Materials Science and Engineering

Written under the direction of

Professor Thomas Tsakalakos

And approved by

—————————————————

—————————————————

—————————————————

—————————————————

—————————————————

New Brunswick, New Jersey

OCTOBER, 2018

ABSTRACT OF THE DISSERTATION

Investigation of the mechanisms of flash sintering in oxide ceramics

By HARRY CHARALAMBOUS

Dissertation Director:

Thomas Tsakalakos

Flash Sintering (FS), has been the subject of intense study by the ceramics community in recent years. Discovered by Cologna, et al. in 2010, flash sintering utilizes the non-equilibrium rise in current under applied electric field to densify ceramic green body compacts in seconds. The model materials used in this thesis were ZnO, TiO_2, and CeO_2 as they are simple binary oxides which avoids the complication of atomic segregation of multi-cation compositions such as 3 and 8 mol% yttria stabilized zirconia (3YSZ and 8YSZ). This work analyzes the proposed mechanisms for the onset of the flash, the cause of the enhanced sintering kinetics during FS, and the temperature approximation methods used as supporting evidence for each theory.

A new temperature approximation technique, referred to as EDXRD temperature calibration, utilizes white beam energy dispersive x-ray diffraction (EDXRD) from a synchrotron source to track the lattice expansion during FS compared to the lattice expansion during conventional sintering (CS). The temperature has been measured as the

rise in temperature causes a proportional lengthening of the bonds, which increases the unit cell volume. For all three test materials the FS temperature has been shown to be comparable to the CS temperature. To estimate average temperature a modification of the blackbody radiation model is presented, which incorporates non-ideal emissivity ($\varepsilon<1$) and cooling due to thermal conduction.

A new procedure to conduct flash sintering experiments was developed using ZnO as a test case. Rather than allowing an uncontrolled rise in current followed by an abrupt limit to constant current, the current was ramped up linearly. Using impedance spectroscopy, it was determined that the conductivity of ZnO increased with an increasing rate of the current ramp and the highest conductivity was measured for the sample densified using conventional FS. This effect was attributed to the increasing loss of oxygen at higher current ramp rates due to the higher driving force for current flow.

Oxygen reduction of TiO_2 was observed in situ using EDXRD, where secondary peaks were formed at higher d-spacing. Consistent with the understanding of ionically bonded ceramics, the creation of oxygen interstitials requires oxidation of metal cations to maintain charge neutrality, which resulted in a lattice expansion with secondary peaks forming at higher d-spacing. Upon further analysis, utilizing Raman Spectroscopy and X-ray Photoelectron Spectroscopy, a remnant reduction of TiO_2 remained even after the electric field was turned off and the specimen was cooled to room temperature. The greater reduction of the anode in comparison to the cathode corresponded to increased densification and grain growth in the anode region, which suggests that the reduction is accelerated by the decrease in the number of vacancy blocking grain boundaries due to grain growth.

In situ EDXRD indicated a significant difference in the lattice expansion for CeO_2 when platinum paste is applied to both ends compared to no platinum paste applied on the faces of the sample adjacent to the electrical contacts. For specimens with platinum paste, a large lattice expansion as well as peak splitting was observed towards the cathode of the pellet facing the negative electrode. This effect disappeared when no platinum paste was applied and a somewhat asymmetrical lattice expansion towards the anode was observed as with the case of TiO_2. The lattice expansion in the platinum coated sample did not match with the expected microstructure: grain growth was promoted towards the anode and suppressed towards the cathode. Thus, while the lattice expansion was dominated by the production of oxygen interstitials as with the case of TiO_2, this was unrelated to the enhanced sintering and grain growth towards the anode.

TEM-EDS analysis indicated a significant difference in stoichiometry between grain boundary and bulk regions at the anode. Significantly higher oxygen content was found at thick grain boundaries (~2nm) at the anode, indicating oxygen ion diffusion along the grain boundaries which were trapped due to the blocking effect of the platinum paste. At the cathode the grain boundaries were clean with negligible thickness and similar atomic composition to the bulk. Inhomogeneity in the lattice expansion and microstructure was not observed when FS is performed using an AC power supply.

Microstructural inhomogeneity was observed for all three materials in the direction of the electric field. The inhomogeneity in microstructure agreed with EDXRD profile inhomogeneity indicating an inhomogeneous temperature profile. The data was fitted to a new model incorporating the Peltier effect, which should occur under DC electric field for p-type and n-type semiconductors. As ZnO, TiO_2, and CeO_2 are all n-type semiconductors

the grain growth towards the anode in all cases agrees with temperature inhomogeneity due to the Peltier effect as increased temperature leads to grain growth.

As the microstructural (grain size and porosity) inhomogeneity was dominated by the Peltier effect, a Joule heating phenomenon, it was determined that the sintering behavior is dominated by Joule heating. The nucleation and avalanche of Frenkel defects are not required to explain the sintering as the sample temperature was not below CS temperatures. In addition, as no experimental evidence for the generation of metal vacancy-interstitial pairs has been produced to date a simpler explanation should be found. The enhanced sintering and grain growth kinetics can also be explained as a result of rapid heating due to the internal heat generation, which is a known effect in CS.

Acknowledgements

Finally, I would like to express my deepest appreciation to my wife, Jennifer, for supporting me as I follow my dreams and to my parents Pavlos and Anthoula for always encouraging me to be my best.

Contents

List of Tables

List of Figures

xiv

1. Literature Review

1.1 Field Assisted Sintering Techniques (FAST)

1.1.1 Spark Plasma Sintering

Spark plasma sintering (SPS) is a field assisted sintering technique as a DC pulse of current is applied through graphite tooling. The name spark plasma sintering is likely a misnomer (1). The "spark plasma" is a theorized mechanism to explain the enhanced diffusion during SPS, which predicts that the rapid pulsing induces momentary sparks in the sample which generate a plasma phase. However, this theory has fallen out of favor in the materials science community in recent years as it has not been observed.

For most SPS setups, a graphite die and graphite pushrods are used to pass current mostly or entirely through the pushrods and surrounding die, providing Joule heating to the specimen. The current passing through the die is generally quite large, up to several kA so the heating rate can be substantial, on the order of $100°C \cdot min^{-1}$. This allows for rapid densification in comparison to a hot press, whose heating rate is much lower. The cooling rate is also rapid as the stainless steel rams are water cooled so when the power is turned off the rams quickly cool the graphite tooling.

A pressure between 50 and 250kN is applied uniaxially during the heating. This pressure adds a driving force to the sintering in addition to the sintering pressure for green body compacts and, in combination to the fast heating, lowers the sintering temperature and obtains fine microstructure at near full theoretical density.

The Peltier effect is apparent in semiconductor sintering using SPS (2, 3). This effect is caused by a heating in the same direction as the charge carriers. For n-type semiconductors the charge carriers are negatively charged and travel towards the anode, which is in contact with the positive electrode. For p-type semiconductors the situation is reversed and so it the temperature gradient. This effect is not observed in metals or other conductors.
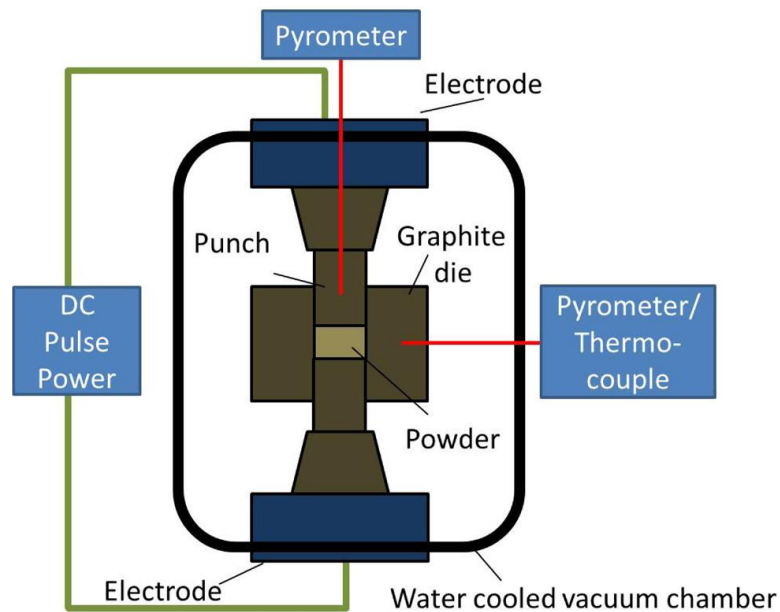
Figure 1: Schematic representation of SPS (4).

1.1.2 Microwave Sintering

Microwave sintering is a contactless FAST technique where microwave radiation, ranging from 1 mm to 1 m in wavelength, is applied to the ceramic material, which absorbs the microwave radiation and heats itself in the process. Characteristics of microwave sintering include high heating rates, lower sintering temperature, and finer microstructure (5). The heating is internal due to the absorption of microwave radiation within the bulk rather than

external, as with conventional heating. Thus, the sample tends to be surrounded with insulation to keep the heat from escaping from the specimen (see Fig. 2).
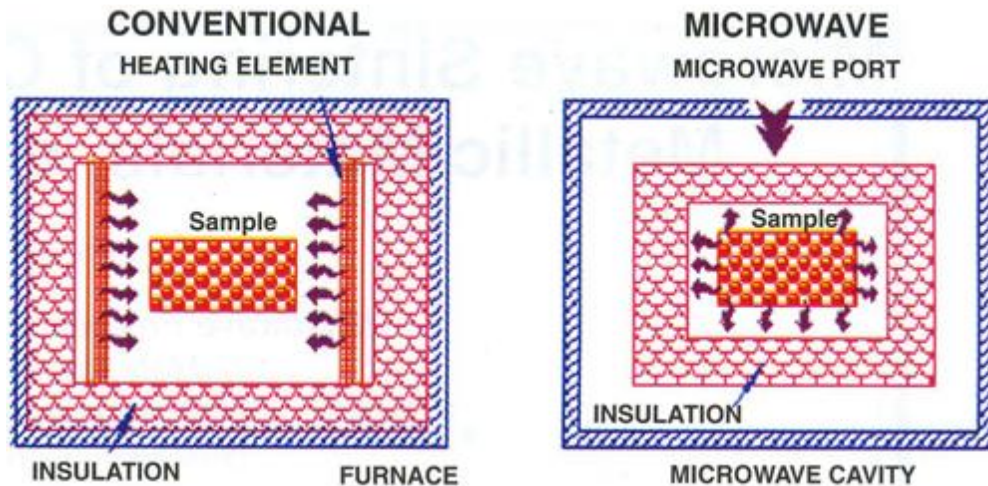
Figure 2: Microwave sintering comparison to conventional sintering (5).

1.1.3 Flash Sintering

Flash sintering (FS) was first published by Cologna, et al., analyzing the effect of electric field on densification of 3 mol% yttria stabilized zirconia (6). The "flash" effect occurs with a nonlinear rise in current flowing through the sample as the furnace temperature rises. Differentiation was made between field assisted sintering technique, FAST, and the sudden rise in current with corresponding electroluminescence, FS. At lower electric fields a small current will gradually rise in the specimen with corresponding enhancement of the densification kinetics compared with conventional sintering (CS) from heating. FAST for 3YSZ was concurrently studied by Conrad, et al. (7-10).

Since this discovery, researchers from across the world have studied the effect of flash sintering on a large range of polycrystalline ceramics: 3 mol% yttria stabilized

zirconia (3YSZ) (6-42), Al_2O_3 (43-48), 8 mol% yttria stabilized zirconia (8YSZ) (12, 41, 49-65), Co_2MnO_4 (66), Gd-doped CeO_2 (GDC) (41, 67-69), $SrTiO_3$ (70-72), $BaCe_{0.8}Gd_{0.2}O_{3-\delta}$ (73), NiO-8YSZ (54), SiC (74, 75), $MnCo_2O_4$ (76, 77), $La_{0.6}Sr_{0.4}Co_{0.2}Fe_{0.8}O_3$ (68, 78), TiO_2 (79-85), TiO_2-Al2O3 (80, 85, 86), $BaTiO_3$ (87-89), SnO_2 (90), SnO_2+MnO_2 (61, 90), 3YSZ-Al_2O_3 (91-93), ZnO (94-101), Y_2O_3 (102), β-alumina (26, 103), $La_{0.2}Sr_{0.7}TiO_3$-Ni/YSZ (104), Sm-doped CeO_2 (SDC) (69), $Li_{1.3}Al_{0.3}Ti_{1.7}(PO_4)_3$ (LATP) (105), $KNbO_3$ (KNN) (106, 107), ZnO-Bi_2O_3 (95), hydroxyapatite (HA) (108), $CaCu_3Ti_4O_{12}$ (CCTO) (109), SiC whisker reinforced 3YSZ (110), Al_2O_3–$Y_3Al_5O_{12}$–ZrO_2 (111), $KNbO_3$ doped $SrTiO_3$ (71), TiB_2–TiO_2–$TiBO_3$ (112), $MgAl_2O_4$ (113), $La_{0.8}Sr_{0.2}Ga_{0.8}Mg_{0.2}O_{3-\delta}$ (LSGM) (114), Ni-doped Y_2O_3 (115), V-doped and N-doped TiO_2 (83), SiC + YAG (116), $BiFeO_3$ (117, 118), ZrO_2 (119), ZrO_2 10 mol% Sc_2O_3 1 mol% CeO_2 (10Sc1CeSZ) (120), UO_2 (121, 122), Al_2O_3-$MgAl_2O_4$-8YSZ (123), $SrTi_{1-x}Fe_xO_{3-\delta}$ (STFO) (124), Gd/Sm-doped ceria (125), TCP (126), CeO_2+$MnCo_2O_4$ (127), $LiNi_{1/3}Co_{1/3}Mn_{1/3}O_2$ (128), and PZT (129).

FS experiments can be performed either isothermally or non-isothermally. In non-isothermal experiments the temperature of the furnace is heated and an electric field is applied. As the temperature rises the specimen becomes more conductive until a nonlinear rise in current occurs. In isothermal experiments the furnace is heated up to a predefined temperature and held at that temperature while an electric field is applied. If the electric field is sufficiently high, then a nonlinear rise in current occurs.

Three stages of flash are generally defined in both cases. A schematic showing the change in E ($V \cdot cm^{-1}$), J ($A \cdot cm^{-2}$), P ($W \cdot cm^{-3}$), and $\rho/\rho_{theoretical}$ (unitless) is given in Fig. 3.

Furnace Temp. 900°C

Stage I | Stage II | Stage III

current control

DC Field — Vcm^{-1}

100 — E$_o$

50 — E$_{equil.}$

0

Current Density — mAmm^{-2}

j$_{max}$

60

40

20

0

Power Density — mWmm^{-3}

P$_{max}$

600

400

200

0

Relative Density

1.0

0.8

0.6

0   20   40   60   80

Time, s
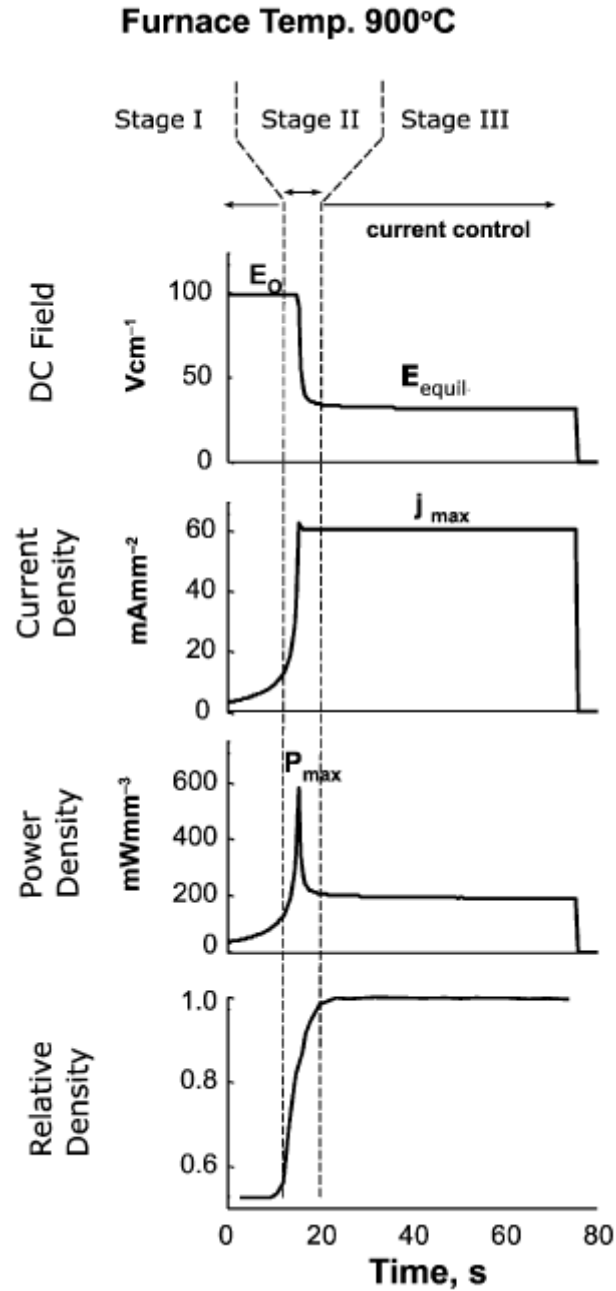
Figure 3: Flash sintering is divided into three distinct stages. Stage I, II, and III along with relative changes to E, J, P, and $\rho/\rho_{theoretical}$ in each stage are shown (31).

In stage I, referred to as the incubation time, a gradual rise in current through the specimen occurs. The current density is usually too low to cause significant sintering, with

necking and the beginning stages of densification occurring. The end of this stage is not clearly defined, but can be taken as the point where the concavity in the current rise changes. A power density in the range of $10 - 40 \ W \cdot cm^{-3}$ is sometimes defined as the end of stage I.

In stage II, referred to as the onset time, the current rises nonlinearly due to a feedback loop between current and conductivity, where higher current increases conductivity which further increases the current. In order to avoid catastrophic runaway of the current and melting of the sample a current limit is set which begins current-control mode, where the electric field reduces to maintain the constant current. The resulting rise and drop in power causes a power spike through the specimen. Most of the densification occurs in this stage, with modest grain growth. The end of this stage is sometimes defined as the setting of the current limit, but more often at the end of the power spike.

In stage III, referred to as the steady state, the electric field levels off to a constant value. Since the power density through the specimen is given by $P = EJ$ the power density also levels off to an approximately constant value. Remaining densification occurs until the closure of the pores and then grain growth takes over, depending on the time allowed for stage III. The electric field can be turned off at any time depending on the desired microstructure.

Flash Spark Plasma Sintering

Flash spark plasma sintering (FSPS), an offshoot of FS, has been used to sinter a number of non-oxide ceramics in addition to oxide ceramics. FSPS has two benefits to conventional FS: sophisticated SPS machines are already commercially available, which can apply huge currents, on the order of several kA, and are additionally configured to

provide high pressures, on the order of 10-100 MPa. A series of FSPS experiments have been published including ZrB_2 (130), SiC (131-133), B_4C (134), 3YSZ (135), $Mg_{2.1}Si_{0.487}Sn_{0.5}Sb_{0.013}$ (MSS) (136), all materials (137), TiB_2-Hbn (138), titanium suboxide (Ti_xO_y) (139), and 50:50wt% B_4C/TiB_2 (140). However, great care must be taken when analyzing "flash" spark plasma sintering to ensure that this is, indeed, a flash phenomenon. SPS machines typically apply low voltages on the order of 10 V, and high currents. This is the reverse situation of what is conventionally seen in FS, where high voltages and low currents are applied. While the low voltage applied conductors and low bandgap semiconductors can be sufficient to initiate a current directly through the specimen, for other materials, such as 3YSZ and Al_2O_3 (137), this claim is dubious at best. FSPS has also been claimed for nickel and other metals. As the conductivity of metals (conductors) actually decreases with temperature the runaway heating effect of flash is not possible.

For these types of initially non-conducting ceramics, external Joule heating can be provided through the normal SPS procedure until the sample becomes sufficiently conductive for the current to flow through it. Some attempts have been made, such as using graphite felt instead of the graphite die (75, 132, 135, 138). However, it's difficult to determine how much, if any current is actually passing through the sample. Another approach used a copper collar (which was not in contact with the sample), and had the current initially pass through the collar to provide external Joule heating. Eventually the copper melted away, which caused the graphite pushrod to come into contact with the SiC green body at higher temperature. At higher temperature the SiC was sufficiently conductive for the small electric field to push current directly through the sample (133).

An approach to oxide ceramics has been to initially reduce the oxide in conventional SPS. This occurs due to the heating in an inert environment in the presence of reducing graphite pushrods and die. The specimen could then be placed again with no graphite die with the current flowing directly through the specimen (139). While this may be a useful approach to producing conducting oxides of differing stoichiometries, densifying the initial stoichiometric oxide is not possible in this way. In addition, the inert environment is generally problematic for oxide ceramics in SPS as they tend to reduce and must be annealed, post sintering to re-oxidize them.

Contactless Flash Sintering

Another offshoot of FS involves the use of contactless FS through the arcing of plasma through the specimen. This approach has been used to densify B_4C, SiC, and SiC:B_4C composites (141) by placing the ceramic between welding electrodes and arcing the current through the specimen as shown in Fig. 4. The technique causes rapid heating, which is high enough to cause melting if not controlled. The arc itself provides the heating as well as the flash so the process can be automated such that a long ceramic specimen can be fed through for continuous sintering. In addition, this technique was further used in the synthesis of SiC platelets, which could be ground up relatively easily for use in other applications (142).
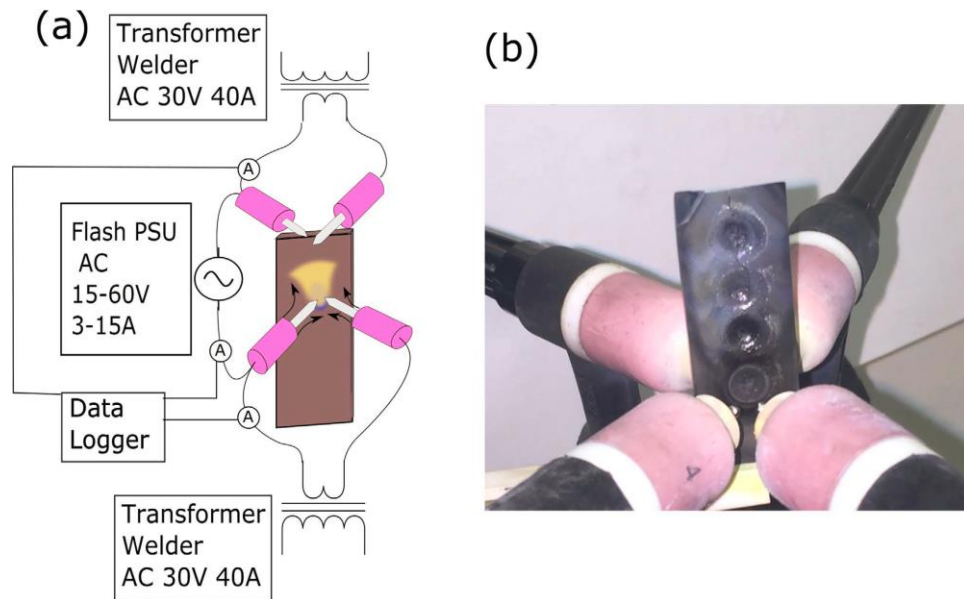
Figure 4: Schematic diagram (a) and picture (b) of contactless flash sintering using plasma electrodes. (141)

This process was taken a step further by nGimat LLC, where a flame initially heats a ceramic film, such as 8YSZ, which has been deposited onto a conducting substrate such as stainless steel through a simple drip coating procedure (143, 144). A large potential bias is applied simultaneously with the flame such that the stainless steel substrate provides the grounding. This causes the arcing of plasma through the film, which leads to both densification and adherence of the film onto the substrate. Over multiple passes the parts of the film exposed to the arc increasingly densify while the surrounding areas do not, allowing for a type of lithography of the film on the substrate.

Flash Effect on Amorphous Ceramics

Interesting effects of flash on glass ceramics have also been shown, both as a pure glass phase and mixed with polycrystalline ceramics to promote liquid phase flash sintering. For example, flash sintering of Al_2O_3 is difficult due to the high resistance of

Al_2O_3, which results in channeling of current into preferred pathways and local melting when sufficiently high electric field is applied to conduct current through the specimen. By mixing with a glass phase such as calcium–aluminum–silicate glass (145), or SiO_2-MgO (47, 146), the glass allows conduction at lower electric field and the liquid phase enhances the sintering similarly to conventional liquid phase sintering.

Additionally, glass phases themselves can be flashed with glass softening occurring, such as sodium silicate and lithium-sodium mixed alkali silicate glasses (147), soda lime silicate glass (148), lead selenide quantum dots in borosilicate glass (149), alkali silicate glass (150). A significant electrode effect is observed using an infrared thermo-camera (148) with a large temperature difference from anode (higher temperature) to cathode (lower temperature). Post flash analysis of the chemistry showed the depletion of sodium at the anode. This was also observed for sodium silicate and lithium-sodium mixed alkali silicate glasses where alkali metals sodium and lithium are depleted at the anode. McLaren, et al. showed that this ion transport is caused by the DC electric field and disappears when an AC electric field is applied instead (150).

1.2 Onset Mechanisms of Flash Sintering

1.2.1 Thermal Runaway

Thermal runaway induced by the feedback loop of current and conductivity is proposed as the mechanism for the onset of flash (44, 49, 95, 96, 126, 151-153). Under a model developed by Todd, et al. (30), the onset of flash sintering occurs only when a critical condition is satisfied, i.e. when the power input into the specimen due to the current flow,

$P = IV$, is greater than the power dissipation out of the specimen due to thermal radiation, conduction, convection, etc. As Joule heating due to the rise in temperature will further increase the specimen conductivity in a feedback loop, this mechanism is referred to as runaway Joule heating or thermal runaway. The material studied in this work was 3YSZ pressed into 55% of theoretical density bars with two holes near either end, similar to dogbone specimen, of 1cm length, and 0.5cm x 0.15cm cross sectional area.

Todd's simplifies this relation by considering only radiative heat loss, W_- , reduced to a quasi-1D heat loss per unit length based on the radius of the cylinder, and the power dissipation per unit length, W_+ , assuming uniform specimen temperature. The following derivation is largely reproduced from (30) in order to determine the thermal runaway condition proposed by Todd.

The power dissipation into the sample due to Joule heating, per unit length ($W \cdot cm^{-1}$), is given as

$$W_+ = \frac{E^2 \pi r_0^2}{\rho_0} exp\left(-\frac{Q}{R(T_0 + \Delta T)}\right),$$ (1.2.1.1)

where E is the applied electric field, r_0 is the original sample radius (cm), ρ_0 is the resistivity pre-exponential term ($\Omega \cdot cm$), Q is the activation energy for the resistivity ($kJ \cdot mol^{-1}$), R is the gas constant ($R = 8.314 \, J \cdot mol^{-1} \cdot K^{-1}$), T_0 is the original furnace temperature (K), and $\Delta T = T - T_0$ is the difference between the specimen and furnace temperature (K).

The heat lost by a grey body, an imperfect black body, is generally given as

$$P_{gbr} = \sigma \varepsilon (T^4 - T_0^4) \,,$$ (1.2.1.2)

where P_{gbr} is the heat lost per unit surface area $(W \cdot cm^{-2})$ to thermal radiation due to grey body radiation (gbr), σ is the Stefan-Boltzmann constant (5.67 x 10^{-12} W·cm^{-2}·K^{-4}), and ε is the material emissivity such that $0 < \varepsilon < 1$. In the approximation of a perfect black body $\varepsilon = 1$ and

$$P_{bbr} = \sigma(T^4 - T_0^4) .$$ (1.2.1.3)

As the surface area of a cylinder is given by $= 2\pi r_0 h_0$, with initial height h_0 , Eq. (1.2.1.2) can be rearranged to give

$$W_- = 2\pi r_0 \sigma \varepsilon((T_0 + \Delta T)^4 - T_0^4)$$ (1.2.1.4)

Before the critical temperature is reached, the heat dissipated due to radiation prevents thermal runaway. However, at the critical point power dissipation due to Joule heating from the current flow the two equations balance such that

$$\frac{dW_+}{dT} = \frac{dW_-}{dT} .$$ (1.2.1.5)

If the temperature or electric field are higher the heating cannot be balanced by the cooling. This results in a significant increase of the specimen temperature which increases the conductivity due to the temperature rise as well as densification at this higher temperature which creates a feedback loop, causing uncontrolled thermal runaway.

The critical applied electric field at the critical temperature can be derived by plugging in the expressions for W_+ and W_- from Eq. (1.2.1.1) and (1.2.1.4) into Eq. (1.2.1.5) and rearranging to give Eq. (1.2.1.6),

$$E_{crit}^2 = \frac{8\varepsilon\sigma\rho_0 R}{r_0 Q}(T_0 + \Delta T_{crit})^5 \, exp\left(\frac{Q}{R(T_0 + \Delta Tcrit)}\right) ,$$ (1.2.1.6)

where E_{crit} is the critical electric field and ΔT_{crit} is the critical change in temperature from furnace temperature. Using an approximation that assumes $\Delta T_{crit} \ll T_0$, we can approximate this expression to give a value for the critical temperature,

$$\Delta T_{crit} \approx \frac{RT_0^2}{Q - 5RT_0} \qquad\qquad (1.2.1.7)$$

A dynamic, non-uniform model was also used with numerical approximation of the temperature and electric field conditions done in Fortran 77. Their results for the above uniform specimen temperature model (SU), dynamic, non-uniform specimen temperature model (DNU) and experimentally obtained values are given in Fig. 5.
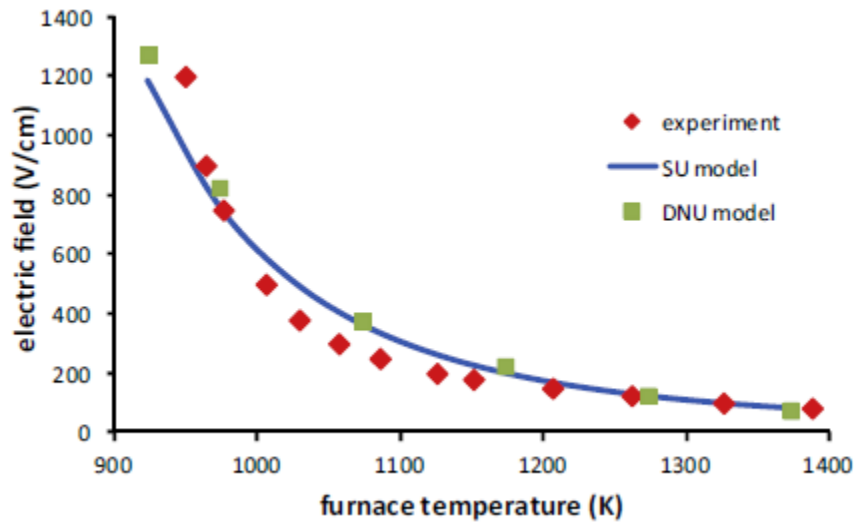
Figure 5: Todd, et al. comparison of thermal runaway predictions to experimental values for 3YSZ (30).

Luo's group come to the same conclusion (83, 95, 99, 100), with the thermal runaway condition written as

$$\frac{d\sigma}{dT}\Big|_{T_S} > \frac{\alpha}{E^2 V_S} , \qquad\qquad (1.2.1.8)$$

where the left side of the equation depends on the material characteristics and microstructure and the right side is made up of experimental conditions. On the left side

the $\frac{d\sigma}{dT}$ term is the rate of change in electrical conductivity of the specimen with respect to temperature. On the right side $\alpha = \frac{\partial \dot{Q}(T_S, T_F)}{\partial T_S} = 4\sigma_{Stefan} T_S^3 A_S$ is the change in power dissipation with respect to specimen temperature, T_S. This term can be calculated using the Stefan-Boltzmann constant $(\sigma_{Stefan} = 5.67 \ x \ 10^{-12} W \cdot cm^{-2} \cdot K^{-4})$, specimen temperature, and surface area from which the thermal radiation can be released. E is the electric field applied and V_S is the specimen volume. As $\sigma = \frac{J}{E}$ and these values are tracked during flash sintering the actual specimen temperature can be approximated at the onset of flash since flash will occur in a non-isothermal experiment at the minimum value for electric field at that temperature.

1.2.2 Defect Nucleation

When a liquid is cooled to its crystallization temperature the solidification requires a starting nucleus of crystalline material to grow around (154). The formation of a critical nucleus size with critical radius is required. When the crystallized region is smaller than the critical radius it is referred to as an embryo and will re-dissolve into the melt. However, when reaching the size of the critical radius it becomes a nucleus around which crystal growth occurs.

According to the "nucleation" theory, developed by Naik, Sglavo, and Raj, the mechanism responsible for the flash event is the nucleation of embryos within the material which transition from insulating to conducting (91). Small polarized (vacancy-interstitial dipoles) regions are formed under the influence of the electric field, with high permittivity on the order of $\sim 10^5 - 10^6$.

These embryos grow gradually during the slow incubation time of stage I of flash until reaching a supercritical size with a critical radius calculated in the same way as the nucleation of a new phase out of solid solution in conventional ceramic kinetics. Following the same derivation as Naik (91), the driving force ($J \cdot cm^{-3}$) is determined by

$$\Delta G_V = \frac{1}{2}\varepsilon_0 \varepsilon_E E^2,$$
(1.2.2.1)

where ε_0 is the permittivity of free space $8.854 * 10^{-14} J \cdot V^{-2} \cdot cm^{-1}$, ε_E is the dielectric constant (unitless) of the nucleation embryo, and E is the applied electrical field ($V \cdot cm^{-1}$).

This Gibbs free energy for a spherical nucleus of radius, r (cm^{-1}), is determined by

$$\Delta G = -4\pi r^3 \Delta G_V + 4\pi r^2 \gamma_E ,$$
(1.2.2.2)

where γ_E is a kinetic barrier formed by the interfacial energy with the un-nucleated surrounding lattice. At the critical size of the nucleus the Gibbs free energy is minimized with respect to radius,

$$\left(\frac{\partial \Delta G}{\partial r} = 0\right)_{r=r*}.$$
(1.2.2.3)

This gives a critical radius, $*$,

$$r *= \frac{2\gamma_E}{\Delta G_V} = \frac{4\gamma_E}{\varepsilon_0 \varepsilon_E E_j^2},$$
(1.2.2.4)

which can be plugged into the Gibbs free energy expression giving

$$\Delta G *= \frac{1}{2}\left(\frac{4\pi}{3}r *^3\right)\Delta G_V$$
(1.2.2.5)

The higher the applied field, the higher the driving force, the lower the critical radius required for the flash event. Thus, a higher electric field lowers the incubation time. The rise in temperature as a result of the small rise in current through the sample in stage I of flash is either independent of the electric field induced nucleation of polarized regions

or may aid in further lowering the incubation time by raising the dielectric constant and, thus further lowering the critical radius.

1.3 Flash Sintering Mechanisms

1.3.1 Joule (over)Heating

One theory for the enhanced sintering kinetics caused by the flow of current due to the applied electric field is the simplest one. The power dissipated in the sample due to the material resistance causes a large heating effect, increasing the temperature above conventional sintering temperature up to a temperature where the sintering kinetics are enhanced in the same way as heating conventionally to high temperature. This has been supported by works on 3YSZ (from 850 to 1600°C in 3s) based on simulation (16), 8YSZ (>2100-2500°C) based on in situ thermometry (56), Gd-doped CeO_2 (67), general ceramics based on use of a blackbody radiation model (see section 2.5.1) (151), ZnO (1772 °C < T_{flash} < 1975 °C) based on partial melting of the sputtered platinum on the pellet faces, $MgAl_2O_4$ (113), $SrTiO_3$ based on blackbody radiation model (72), and β-TCP (126).

1.3.2 Avalanche of Frenkel Defects

According to Cologna, et al. (43) and others (17) (155) (102) the temperature rise caused by Joule heating is too low for explain the enhanced sintering kinetics to be caused by heating alone. In fact, the temperature rise tends to be lower than the conventional sintering temperature, which has much slower kinetics. Instead, it is suggested that Frenkel pairs, i.e. vacancy-interstitial pairs are created for both the oxygen anions and metal cations. Each Frenkel pair has electrons and holes associated with them, such as two extra

electrons held by oxygen interstitials and two extra holes held by oxygen vacancies. Due to the force applied by the electric field, Cologna suggests that the electrons and holes are stripped from the Frenkel pair, which travel along the direction of the electric field. The remaining vacancy-interstitial pair are now both neutral and are more mobile due to their charge neutrality. The sintering pressure causes the interstitials to travel to the pores while the vacancies travel to the grain boundaries, which enhances the sintering kinetics.

One of the main points supporting the theory that the nucleation of defects under the electric field is required to explain the enhanced kinetics is the claim that the temperatures of the specimens during flash sintering is below the conventional sintering temperatures. Three pieces of evidence are presented, primarily by Raj's group, to support the claimed insufficient temperatures: infrared pyrometry, a blackbody radiation model, and in situ XRD calibration using synchrotron radiation.

1.3.3 Local Heating at the Grain Boundaries

Similar to the enhanced diffusion during liquid phase sintering, the enhanced diffusion during flash sintering has been proposed to be the effect of local melting at the grain boundaries (156-158). According to Narayan defects and impurities that segregate near the grain boundaries and under high applied fields Joule heating occurs due to electronic and ionic conduction (156). The preferential flow of current along the grain boundaries causes melting which results in kinetics on the order of $10^{-4} - 10^{-5} cm^2 \cdot s^{-1}$. According to Chaim, higher current concentration at the particle contacts causes melting at the contacts (157). Capillary forces then cause the liquid phase to spread along the entire grain boundary, which causes full wetting as the liquid and solid are the same chemical composition.

Alternatively, preferential heating at or near the grain boundaries may not be sufficient to cause melting, but will raise the temperature considerably with respect to the overall sample temperature (6, 13, 49, 73). This approach is more plausible as the temperature gradient can be less severe than melting. A potential cause is higher resistance at the space charge layers, which have slightly different stoichiometries from the bulk, which results in local heating near the grain boundaries. The energy at the grain boundaries,

$$\gamma_W = \Delta H_W - T \Delta S_W , \qquad\qquad (1.3.3.1)$$

would be a minimum since $T\Delta S_W$ would be maximized. This would help reduce bulk diffusion characteristic of grain growth.

$$\gamma_w = \Delta H_w - T\Delta S_w$$

Decreasing Temp   Decreasing Temp

γ_w

PINNED BY INTERFACIAL
JOULE HEATING
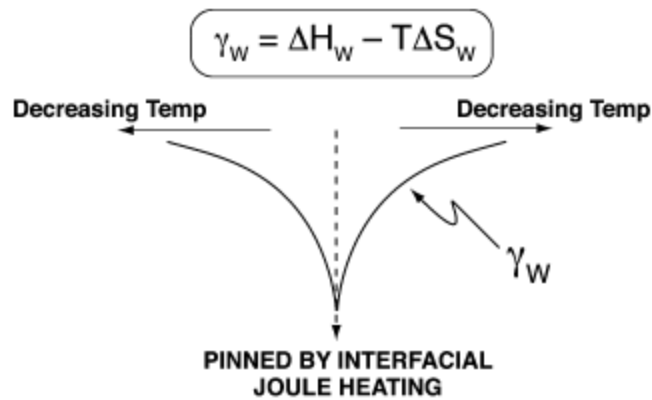
Figure 6: Minimization of the interfacial energy due to preferential heating of the space charge layers. (13)

There are a number of issues with this theory. First, the heat will distribute and as the distance between the grain boundary and the grain center is very small the heat will distribute rapidly, making a significant temperature gradient difficult to sustain. This is especially the case in the steady stage during stage III, when the overall temperature

remains constant or even declines as the sample becomes less resistive during sintering. Local heating is more likely to play a role at the onset of flash in stage II when the temperature is rising rapidly, on the order of $100 \, °C \cdot s^{-1}$.

In addition, local heating at the grain boundaries will increase conductivity at the grain boundaries, which will dampen the Joule heating to some limit. As melting creates a liquid phase, which is much more conductive than the solid grains, the liquid phase is unsustainable. In addition, achieving a local heating effect sufficient to cause melting while the grain bulk is at or below the conventional sintering temperature is unlikely as this typically requires a huge temperature difference of several hundred degrees.

For the case of a smaller local heating effect in stage II we can approximate the time needed for the temperature to equilibrate between grain boundary and bulk assuming a sudden heating. Continuous internal heating will complicate matters, but this simplification should give an approximate picture of the thermal gradient. This procedure was also used by Ji, et al. (37). The thermal diffusivity of a material is given by

$$\alpha = k/\rho c_p \, , \tag{1.3.3.1}$$

where α is thermal diffusivity $(cm^2 \cdot s^{-1})$, k is thermal conductivity $(W \cdot cm^{-1} \cdot K^{-1})$, ρ is density $(g \cdot cm^{-3})$, and c_p is specific heat capacity $(J \cdot g^{-1} \cdot K^{-1})$. The time, t (s), taken for the temperature to reach equilibrium is on the order of

$$t \propto x^2/\alpha \, , \tag{1.3.3.2}$$

where x is the average distance between grain boundary and center of the grain.

The specific heat capacity of some select ceramics are listed in the table below with sample temperature $T = 1000\,°C$ and grain size $G \sim 1\,\mu m$ assumed for simplicity. In addition, the density of each material is taken as the theoretical density. All of these cases have similar times to reach thermal equilibrium. Even assuming a rise in the temperature on the order of $100\,°C \cdot s^{-1}$ the equilibrium would still be reached by 3 orders of magnitude faster than the temperature is rising.

Table 1: Estimate of times required to reach thermal equilibrium for select materials.

	Thermal Conductivity $(W \cdot cm^{-1} \cdot K^{-1})$	Density $(g \cdot cm^{-3})$	Specific Heat Capacity $(J \cdot g^{-1} \cdot K^{-1})$	Thermal Diffusivity $(cm^2 \cdot s^{-1})$	Thermal Equilibrium time (μs)
ZnO	0.04 (159)	5.6 (160)	0.6658 (161)	0.010	1
TiO$_2$	0.0335 (162)	4.23	0.961 (163)	0.0082	1.2
CeO$_2$	0.0126 (162)	7.21 (127)	0.441 (162)	0.0040	2.5
3YSZ	0.027 (164)	6.05 (37)	0.69 (164)	0.0065	1.5
8YSZ	0.0222 (162)	5.9 (63)	0.63 (165)	0.0060	1.7
Al$_2$O$_3$	0.062 (162)	3.99 (43)	0.88	0.0179	0.6

1.3.4 Pore migration and Electro-Sintering

I-Wei Chen's group have written a series of papers elucidating the theory that pore ionomigration and electro-sintering are the predominant mechanism in flash sintering (50, 55-58). The pore migration is induced by the electric field and is controlled by surface diffusion. In their first work of this series Kim, et al. found that there is a bimodal grain size distribution from anode to cathode in 8YSZ with an abrupt transition from small to large grains (50). The sample temperature during the steady state of flash was measured using an infrared pyrometer.

Using SEM the average grain size was calculated at the anode $D_{anode} = 1.22 \pm 0.02$ μm and at the cathode $D_{cathode} = 21.7 \pm 0.33$ μm. The transition was abrupt with little to no gradient of grain size at the transition region. The large grains at the grain boundary were observed to be elongated, which may be the result of larger grains absorbing smaller grains at the other side of the divide. A summary of the findings is given in Fig. 7. Of note, inspection of the grain size from the picture indicates that the very end of the cathode has smaller grains compared to near the end of the cathode.
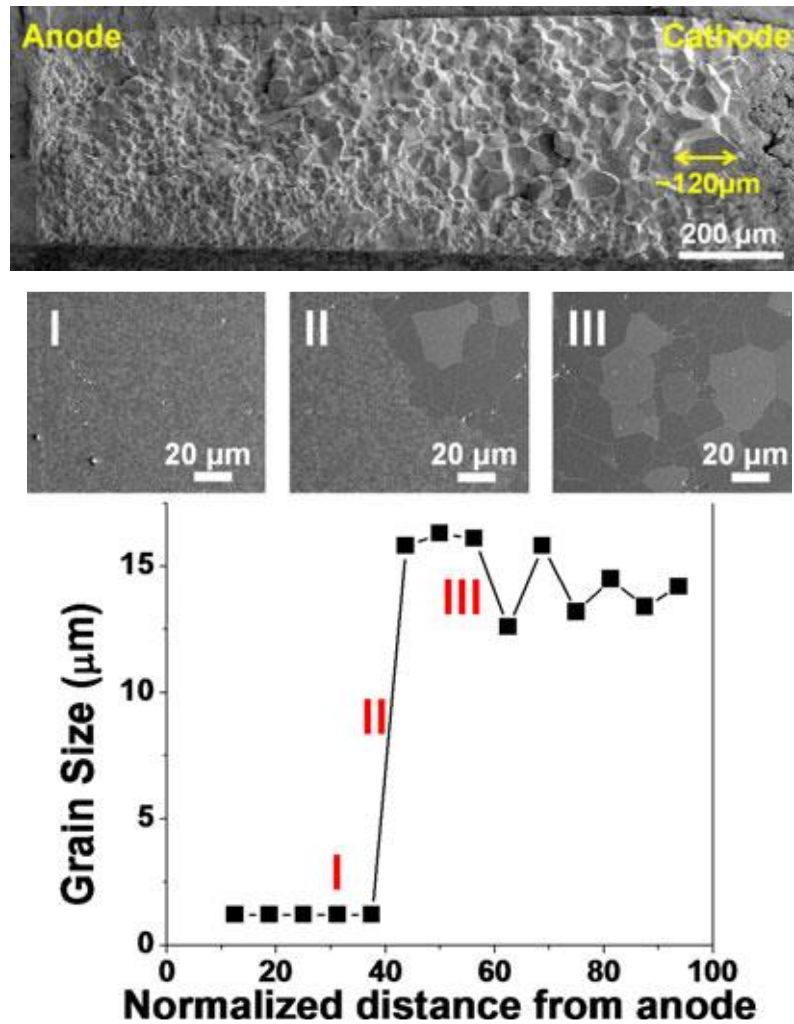
Figure 7: Microstructural variation from anode to cathode for 3YSZ. There is an abrupt transition from smaller to larger grains in the central region towards the anode. (50)

A specimen conventionally sintered to high density was later flashed, showing a less abrupt and less extreme grain size transition with $D_{anode} = 1.35 \pm 0.13$ µm and $D_{cathode} = 16 \pm 1.31$ µm. In addition, they reported increase from ~90% of theoretical density at the anode to ~100% of theoretical density at the cathode. Since the initial specimen density was approximated to 95%, this suggests that the porosity actually increased at the anode while decreasing at the cathode. This phenomenon was explained as a result of pore migration away from the negative electrode towards the positive electrode, which accumulated around the anode.

The pores are not migrating under the direct influence of the electric field. Instead the accumulation of V_O'' due to the electric field, as 8YSZ is an excellet oxygen ion conductor at high temperatures, causes the reduction cations (mostly Zr). The reduced Zr have higher mobility compared with stoichiometric 8YSZ, which leads to surface diffusion of Zr^{4+} ions towards the cathode. This surface diffusion drives pore migration in the opposite direction, towards the anode, but only at high density as at lower densities the pores have more room to move in other directions.

Further work exploring the ionomigration of pores in 8YSZ (57) showed inhomogeneity in the concentration of pores, both intergranular and intragranular, correlated to distorted grain boundaries. This is attributed to either pore migration through the grains, which distorts the grain boundaries, or to grain boundary migration.

The anode shows both less sintering (higher concentration of pores) and less grain growth compared to the cathode for 8YSZ (55). For thinner samples the difference is less extreme compared with thicker samples. The grain growth is somewhat suppressed until reaching high density and tends only for furnace temperatures >1250 °C at the onset of

flash. Also explained by this work there appears to be a porosity redistribution towards the center as a result of the electric field. Pores from the cathode migrate to the center on their way to the anode while pores at the anode migrate to the edge and the gas escapes to the environment. However, as the pores move they tend to combine into larger pores, which move slowly until they become large enough to be effectively pinned. Therefore, pores tend to build up around the center of the specimen.

In their seminal work theorizing the ionomigration of pores and gas bubbles in yttria-stabilized cubic zirconia Wan, et al. studied the fraction of these "distorted" grain boundaries with respect to normalized distance from the anode (58). They determined that the fraction of distorted grain boundaries increased near the edge of the anode (Fig. 8). Pore breakaway was also observed (Fig. 8), which was attributed to gradual movement of pores, through the grains, towards the anode.
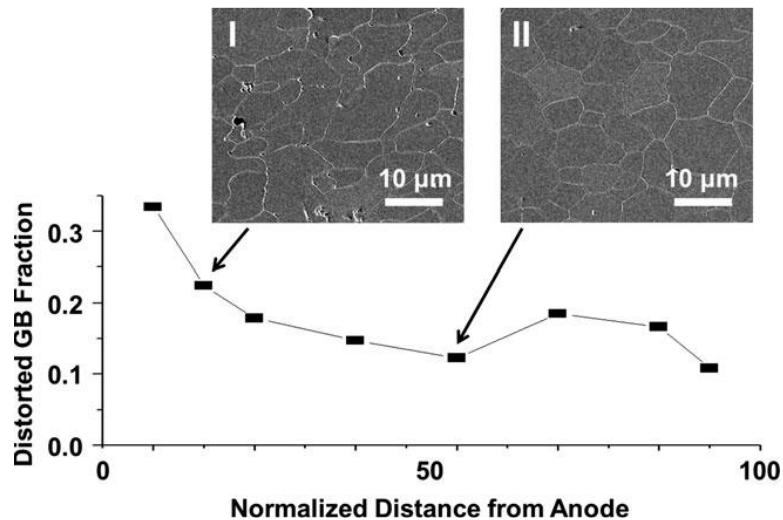
Figure 8: Fraction of distorted grain boundaries in 8YSZ with respect to position (58).
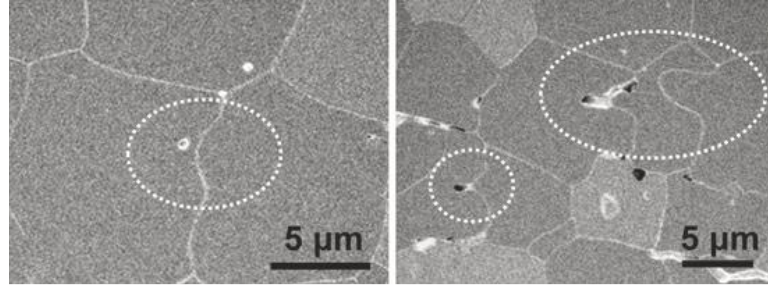
Figure 9: Observation of pores near the grain boundary in 8YSZ with evidence of bubble migration evidence through the distortion of the grain boundary. (58)

1.3.5 Ultra-Fast Heating

Fast firing is an enhancement of the sintering kinetics due to rapid heating of the ceramic green body. Gomez, et al. determined that fast firing at a rate of $500 \, °C \cdot min^{-1}$ of 3YSZ and 8YSZ reduces grain growth while achieving similar density in comparison to slow firing at $10 \, °C \cdot min^{-1}$ (166, 167). This was attributed to avoiding some of the grain coarsening that occurs during heating to maximum temperature. According to a study by Zhang, et al. (168) the fast firing of alumina creates diffuse, open grain boundaries, from which they suggested that the enhanced sintering kinetics are caused by the destabilization of the grain boundaries from equilibrium due to the rapid influx of heating.

Flash sintering can be considered an ultra-fast firing technique, with heating rate on the order of $100 \, °C \cdot s^{-1}$. Destabilization of the grain boundaries would be even more prominent here with such a rapid change in temperature. Two papers analyzed the effect of conventional fast firing to flash sintering for the cases of 3YSZ (37) and ZnO (99).

For 3YSZ two fast firing experiments were devised to compare with flash-fast firing. In order to heat to similar temperatures as FS a non-equilibrium blackbody

(greybody) radiation model was given to determine the temperature at the power spike where $\frac{dT}{dt} \neq 0$, such that

$$\frac{dT_s}{dt} = \frac{VI - A\sigma\varepsilon(T_s^4 - T_f^4)}{mc_p} \, , \qquad\qquad (1.3.5.1)$$

where $P = VI$, the power dissipated in the specimen, A is the surface area, σ is the Stefan-Boltzmann constant (5.67 x 10^{-12} W·cm^{-2}·K^{-4}), ϵ is the unitless emissivity of the material such that $0 < \epsilon < 1$, T_s is the specimen temperature, T_f is the furnace temperature, m is the mass of the specimen, and $c_p = 600J \cdot kg^{-1} \cdot K^{-1}$ is the specific heat capacity of 3YSZ. Integrating this equation gives

$$T_s = T_f + \int_0^t \frac{VI - A\sigma\varepsilon(T_s^4 - T_f^4)}{mc_p} dt \, . \qquad\qquad (1.3.5.2)$$

The first fast firing experiment involved a simple insertion of the specimen into the hot zone. This method heats more slowly than FS as the sample temperature must reach thermal equilibrium with the furnace. As a result, the dwell time is lowered with respect to conventional heating (CH), but is still longer than FS. Another technique, referred to as self-propagating high temperature synthesis (SHS) uses the exothermic reaction between nickel and aluminum powders to rapidly heat the specimen, producing a rapid heating of the specimen with enhanced sintering kinetics similar to FS. The heating and densification rates are summarized in Fig. 10 and 11.
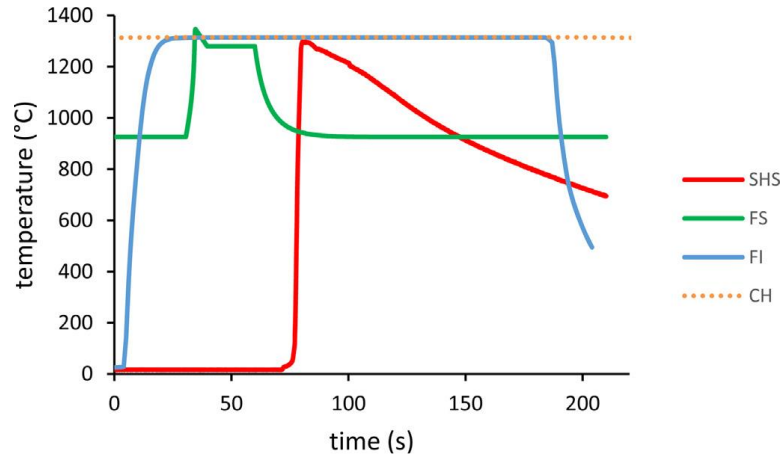
Figure 10: Temperature profiles of 3YSZ with respect to time for fast heating methods, flash sintering (FS), furnace insertion (FI), and self-propagating high temperature synthesis (SHS), explored by Ji, et al. with baseline temperature given for conventional heating (CH) (37).
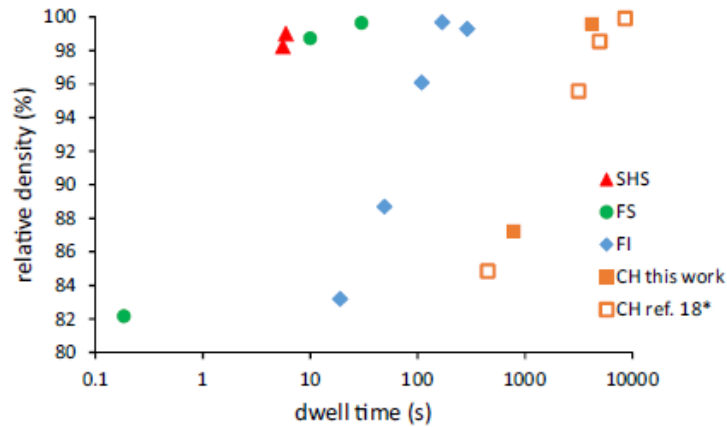
Figure 11: Densification of 3YSZ as a function of dwell temperature for conventional heating (CH), flash sintering (FS), furnace insertion (FI), and self-propagating high temperature synthesis (SHS) (37).

They have explained two potential mechanisms for the rapid sintering kinetics. The first is the known fast firing effect where rapid heating avoids grain and neck growth, which slow the densification as the sintering rate is inversely proportional to the grain size by $1/D^4$. Alternatively, the grain boundaries may become destabilized, which enhances the diffusion as the activation for mass transport along the grain boundaries is lowered.

Zhang, et al. explored the same effect using ZnO as the model system (99). Using a rapid thermal annealing apparatus a temperature rise of $200\,°C \cdot s^{-1}$ to $1000\,°C$ and $1100\,°C$. Rapid densification is followed by rapid grain growth with no applied electric field, indicated that the enhanced kinetics are related to the rapid rise in temperature alone.
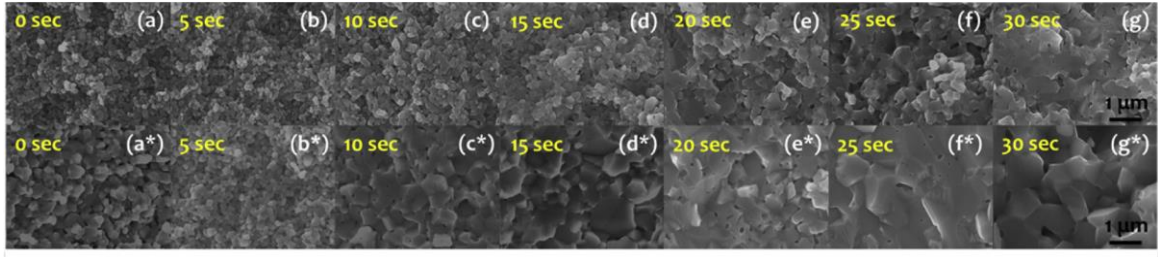
Figure 12: Rapid grain growth in rapid thermal annealing experiments of ZnO to 1000°C (a-g) and 1100°C (a*-g*) with dwell times from 0-30s (99).

The fast firing effect, whether it is caused by the avoidance of grain coarsening due to rapidly reaching the sintering temperature or by the destabilization of the grain boundaries, is a known effect. There is certainly Joule heating at a rapid rate during FS so this mechanism is plausible and is not limited to specific compositions. The main concern is that many temperature approximations using a blackbody radiation (1.4.1), infrared pyrometry (1.4.2), or XRD calibration from a platinum standard (1.4.4) suggest that the temperature during FS is considerably lower than the CS temperature.

1.4 Temperature Approximation Methods

1.4.1 Blackbody Radiation Model

According to the blackbody radiation model, introduced for use in calculating specimen temperature during flash, in the steady state of Stage III of FS the specimen temperature will equilibrate with internal power due to Joule heating balancing external heat loss due to black body (or grey body) radiation. The derivation is derived in the following, similarly to Yang, et al. (8) as well as Raj (155)

The power expended by the sample due to thermal radiation is given as

$$I = \epsilon\sigma(T^4 - T_0^4) , \qquad\qquad (1.4.1.1)$$

where I is the blackbody radiation expended over the surface of the sample ($W \cdot cm^{-2}$), ϵ is the unitless emissivity of the material such that $0 < \epsilon < 1$, σ is the Stefan-Boltzmann constant (5.67 x 10^{-12} W·cm^{-2}·K^{-4}), T is the sample temperature in the steady state, and T_0 is the starting temperature before flash, i.e. the temperature of the furnace. The thermal radiation of the specimen with no current is

$$I_0 = \epsilon\sigma T_0^4 \qquad\qquad (1.4.1.2)$$

Assuming the power dissipation is determined by the current density, J ($A \cdot cm^{-2}$) and electric field, E ($V \cdot cm^{-1}$), values measured during the flash sintering event, due to sample resistance then $I = \frac{P}{A}$. For a cylindrical specimen $A = \pi dh$ with sample diameter, d, and sample height, h. The top and bottom faces are ignored since they are in contact with the electrodes rather than exposed to the atmosphere. For a dogbone specimen the heating dissipation is concentrated in the rectangular gauge section so $A = 2ah + 2bh$, with cross

sectional area, $a \times b$ and electrode separation, h. Eq. (1.4.1.2) can be rearranged to give an expression for T,

$$T = \left(T_0^4 + \frac{P}{\epsilon \sigma A}\right)^{1/4}, \qquad (1.4.1.3)$$

which is used in blackbody radiation temperature calculations assuming either $\epsilon = 1$ for the ideal case or $\epsilon \neq 1$ for real materials.

The blackbody radiation model is a theoretical model and not experimental evidence so it must be used carefully to avoid erroneous conclusions. For example, if the author is a proponent of defect generation which enhances diffusion kinetics (155) then the blackbody radiation model proves that the temperature of 3YSZ is below the conventional sintering temperature. However, if the author is a proponent that Joule heating at a fast rate, i.e. fast firing, is responsible for the enhanced sintering kinetics then the temperature of 3YSZ during flash is comparable to the conventional sintering temperature (30).

In addition, the model must be modified depending on the experimental conditions. Depending on the material properties the value of the emissivity, ε, the thermal radiation can vary significantly. Assuming a perfect blackbody will cause underestimation of the specimen temperature. The specimen geometry and experimental apparatus will affect the specimen temperature. For example, while minimal thermal conduction occurs for dogbone shaped specimen as it is suspended by two platinum wires, pellets that are wedged between electrodes will have significant cooling and the effect of thermal conduction must be taken into account.

The following derivation of a greybody radiation model with thermal conduction has been derived in a previous work (169). We start with the greybody radiation,

$$I_o + I = \epsilon\sigma T^4, \tag{1.4.1.4}$$

with $I_o = \epsilon\sigma T_o^4$ is the blackbody radiation generated by the sample in the furnace without flash (W·cm⁻²), I is the extra blackbody radiation generated due to the power dissipation during flash (W·cm⁻²), ϵ is the material emissivity (unitless), σ is the Stefan-Boltzmann constant (5.67 x 10⁻¹² W·cm⁻²·K⁻⁴), and T is the sample temperature (K). This results in a modest increase in the temperature approximation.

We add a thermal conduction factor to modify this equation,

$$I_o + I = \epsilon\sigma T^4 + I_{conduction}(t, x) , \tag{1.4.1.5}$$

where $I_{conduction}$ is the power loss per unit area (W·cm⁻²) due to conduction to the electrodes. In the case of the steady state of flash there are constant specimen and stage temperatures and constant cross sectional area. The temperature gradient reduces to

$$I_{conduction} \sim \frac{k}{L/2}\Delta T , \tag{1.4.1.6}$$

where k is the material dependent thermal conductivity factor (W·cm⁻¹·K⁻¹), L is the thickness of the pellet, and $\Delta T = T - T_c$, T_c is the temperature at the contacts. The final temperature can be computed using a greybody radiation and thermal conduction model,

$$I_o + I = \epsilon\sigma T^4 + \frac{2k}{L}\Delta T. \tag{1.4.1.7}$$

1.4.2 Infrared Pyrometry

Infrared pyrometers operate by using focusing the infrared energy emitted by the sample into a detector and inferring the temperature by the intensity of the infrared energy. Infrared pyrometry has been used to estimate the specimen temperature in a number of flash sintering works (18, 25, 30, 43, 56, 62, 76, 78, 102, 148). In almost all cases the conclusion is that the specimen temperature is below CS temperatures despite similar densification or the specimen temperature is comparable to CS temperatures with higher densification and grain growth. However, this conclusion is erroneous as it is well known that internal heating with thermal radiation will result in a cooler surface in comparison to the interior.

Using a finite element simulation, da Silva showed a substantial temperature gradient of several hundred degrees between the surface and center of the gauge (Fig. 13) (62). Experimental measurements using pyrometer matched the predicted temperature from this simulation. Even if the temperature gradient is not as severe as suggested, even a 100 ℃ temperature difference would have a substantial effect on the microstructure and predictions of the FS mechanism. In addition, the emissivity is assumed to be close to 1 for most infrared pyrometers, which produces the same underestimation of the temperature as the blackbody radiation model with emissivity taken to be 1.
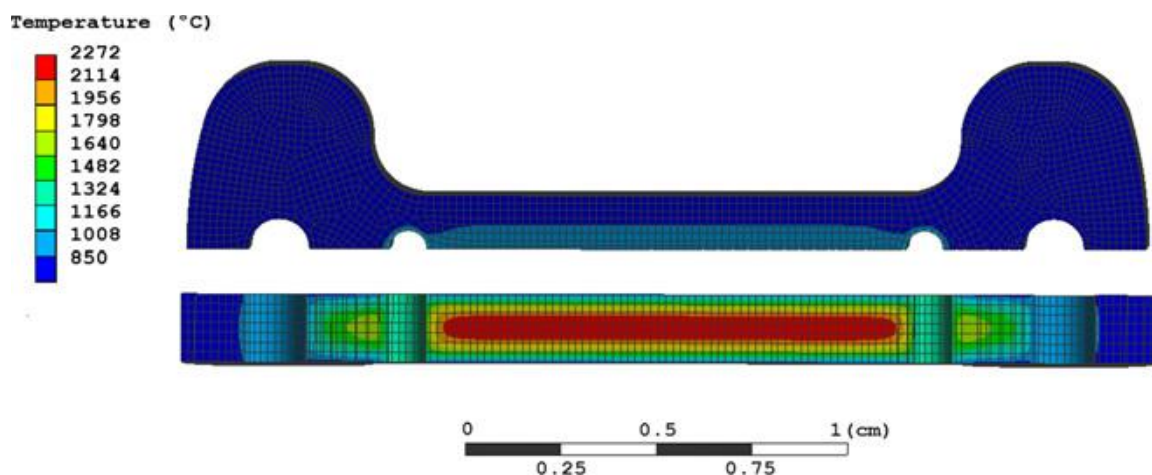
Figure 13: Finite element model showing predicted temperature gradient in 8YSZ. The temperature distribution is modeled after 5 seconds in current control (62).

1.4.3 EDXRD Temperature Calibration

In a series of papers by the group of Tsakalakos, the temperature during FS has been experimentally determined for a variety of oxide ceramics including ZnO (170), CeO_2 (171), $BiFeO_3$ (172), and TiO_2 (169). The approach uses energy dispersive x-ray diffraction (EDXRD) with the procedure, summarized originally for ZnO (170), repeated in the following section:

To estimate the temperature of the specimen during flash sintering, a sample is conventionally heated and the interplanar spacing from sufficient diffraction peaks are tracked, depending on the crystal structure, and used to calculate useful structural parameters such as lattice parameters, a and c, for the hexagonal or tetragonal case or a single lattice parameter, a, for the cubic case. The total unit cell volume can also be calculated from the appropriate parameters. During conventional heating the lattice parameters generally increase as the unit cell expands due to the expansion of the bond lengths with respect to temperature. By fitting a function to this data the lattice expansion

during FS can be linked to the conventional lattice expansion assuming there is no unusual lattice expansion caused by defect generation such as the reduction that occurs in many oxides. An example of this procedure is shown for ZnO in Fig. 14.
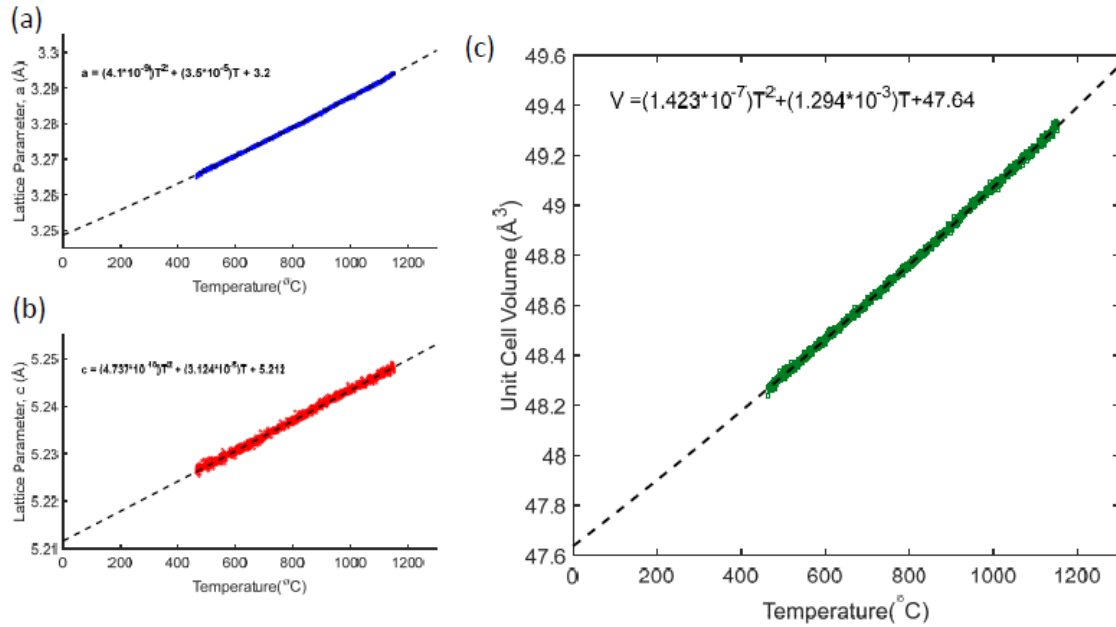
Figure 14: Lattice parameter expansion of (a) 'a' and (b) 'c' with temperature. Unit cell volume calibration using furnace temperature is used to estimate the actual sample temperature under flash (c) (170).

The benefit of this procedure is that this is a direct experimental measurement and the effect of defect formation can also be observed as peak broadening if a significant proportion of Frenkel defects are formed. The ability to measure bulk material response rather than surface response makes this a non-surface sensitive technique. Additionally, this method can probe different regions of the sample for comparison, i.e. interior/exterior and anode/cathode regions. The data is calibrated directly to thermocouple measurements and can be taken at high acquisition rate, down to 1s for TiO_2 (169). The measurements are taken for a gauge volume within the bulk of the specimen, avoiding underestimation of the

temperature inherent in infrared pyrometry, which only measures surface temperature. The major drawback of this method is that this approach is cumbersome. A synchrotron x-ray source is required to give sufficient intensity of the beam to take meaningful data for the rapid process of flash. The process of EDXRD and experimental procedure are described in further detail in section 3.2.

1.4.4 Other Temperature Approximation Methods (Impedance Spectroscopy, XRD Calibration from Platinum Standard, Melting Temperature Minimum)

In situ Thermometry using Impedance Spectroscopy

Using AC impedance spectroscopy, in situ thermometry is performed by taking electrical resistance as a temperature dependent factor (41, 56). The impedance spectroscopy was performed over a frequency range of 1 Hz - 300 kHz and the impedance, Z' is related with the expression,

$$Z'/T \propto exp(\frac{\Delta H}{RT}),$$
(1.4.4.1)

where R is the gas constant ($R = 8.314 \, J \, / \, mol \cdot K$), and $\Delta H = 82.8 \pm 0.7 kJ/mol$, taken from the literature. Of note these samples were predensified to 92% density using CS 1500 °C for 2 hours.

An enormous rise in temperature due with Joule heating, with temperatures rising to >2100 – 2500 °C, are extrapolated using impedance spectroscopy during flash. However, the temperature rise is somewhat reduced with thinner samples. This method could, in principle, be used for materials other than 8YSZ.

X-ray Diffraction Calibration from Platinum Standard

A series of temperature approximations were made using the tracking of x-ray diffraction peak shifts during heating including 3YSZ (27, 32, 173), TiO_2 (82), and TiO2-Al2O3 (86). Based on the thermal expansion of the lattice during conventional heating, the sample temperature was estimated by linking the lattice expansion during flash to the lattice expansion during conventional heating. A thin strip of platinum paste is painted onto the center of the dogbone perpendicular to the direction of the electric field. A schematic for these experiments is given in Fig. 15, taken from Jha, et al. (82).
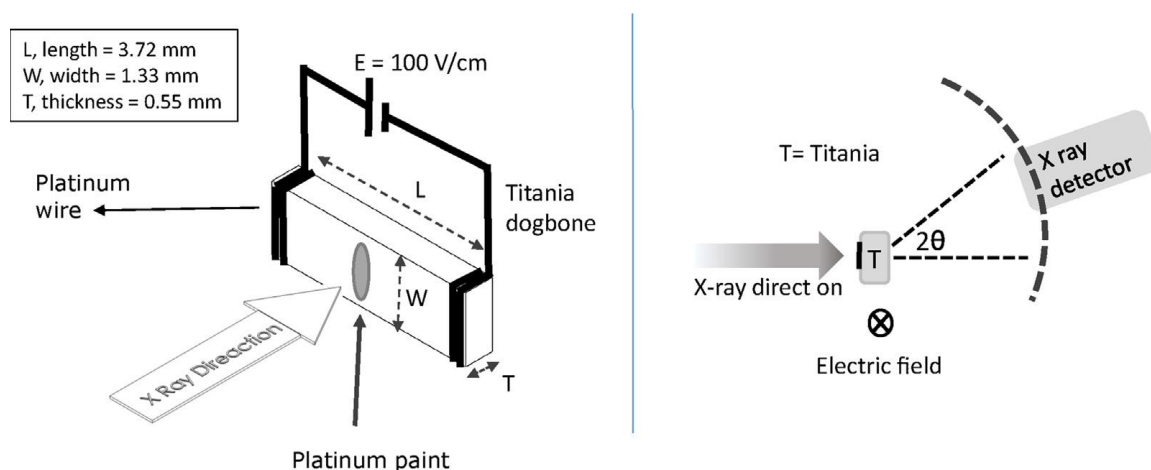
Figure 15: Experimental setup of monochromatic x-ray diffraction experiments performed using synchrotron radiation (82).

This is an indirect approach with a critical issue: The authors based all of their findings on the thermal expansion values of platinum from a single published paper from 1972 (174). Every peak for the studied materials were linked to the expansion of the platinum peak with no external thermocouple to test the accuracy of the temperature for any of the experiments, whether conventional heating or flash.

The samples were also all pre-sintered and then flashed again to avoid movement of the specimen during sample shrinking in the first flash. The sample gauge sections are extremely thin, generally a fraction of a millimeter, which means thermal radiation will dissipate the heat more efficiently, which lowers the specimen temperature below those found in conventional flash sintering experiments.

With these issues in mind, the temperatures may be underestimates of the temperatures achieved during FS and a more direct approach is needed to measure the specimen temperature (during the sintering process) with a thermocouple backup to the conventional heating data. This method was described in section 1.4.3 using EDXRD to calibrate the temperature in a similar way, but with a direct measurement of the material lattice expansion during furnace heating.

Melting of Platinum Paste

Zhang, et al. observed melting in the thin platinum layer sputtered onto the faces of the pellet, but not melting of the platinum wires touching the faces of the pellet (96). Based on the melting point of platinum at 1772 °C and the lack of evidence of melting in the ZnO specimen, which has a melting temperature of 1975 °C, Zhang suggested that the sample temperature rose to $1772 \,°C < T_{flash} < 1975 \,°C$, which would easily explain the rapid kinetics.

The paper studied the effect of air, pure O_2, argon, and argon + 5 mol% hydrogen, but the melting was only observed in the argon + 5 mol% H_2. The furnace temperature of the argon + 5 mol% H_2 was actually the lowest at the onset of flash (under $E = 300V \cdot cm^{-1}$), 186 °C compared to the maximum onset temperature of 631 °C with a pure O_2

atmosphere. As this means a temperature change of $1586\,°C < \Delta T < 1789\,°C$ in the sample, which is implausible. A much more plausible explanation is that the H_2 reacted with the platinum coating, creating the melting effect without such a dramatic temperature rise.

2. Thesis Objective

The primary goal of this thesis work is to analyze the effect of electric field on the sintering behavior of oxide ceramics. A series of test materials were chosen based on the level of iconicity of each material: ZnO (55%) (170, 175), TiO$_2$ (59%) (169, 176), and CeO$_2$ (74%) (171). This work has been divided into three parts, one part for each material with focus on the mechanism(s) responsible for the onset and sintering during flash as well as the findings with regards to the properties of each oxide sintered under flash. Journal article titles and abstracts are listed verbatim for each subject material below:

2.1 ZnO

Investigation of temperature approximation methods during flash sintering of ZnO

The lattice expansion in ZnO, using in-situ X ray diffraction, has been investigated during flash sintering with varying current densities. While current flow through the specimen enhances the kinetics of sintering for ZnO, the temperature is not high enough to claim thermal runaway or localized melting. Unlike the case of yttria stabilized zirconia (29, 52), experimental temperature approximations predict comparable specimen temperature to conventional sintering temperature of ZnO. Microstructural analysis supports the findings of the in-situ temperature approximations. In comparison with black body radiation, a gap between theoretical value and measured value was found due to flaws in the theoretical model. In addition, a new current ramp flash sintering technique was introduced to avoid the characteristic power spike, which has been the source of much debate about the

transition from voltage to current control. The advantage of this method is in the controlled sintering kinetics thus avoiding the channeling found in dielectric materials (87).

Flash sintering using controlled current ramp

In conventional flash sintering, the current rises nonlinearly to a set current limit, accompanied by a spike in the power density. This sudden power spike may cause hot spot formation, in which current preferentially channels through a small area, causing localized melting while other areas remain unsintered. By using a controlled current ramp early on the sudden power spike can be avoided. In addition, by changing the ramp rate material properties such as porosity, grain size and conductivity can be tuned.

2.2 TiO$_2$

Inhomogeneous reduction and its relation to grain growth of titania during flash sintering

Flash sintering under DC electric field partially reduces titania (rutile) and promotes abnormal grain growth near the anode. The resulting reduction in grain boundary density reduces the number of vacancy traps and enhances the O^{2-} ion conductivity through the specimen, facilitating greater non-stoichiometry. The observed gradient of densification and grain-growth across the two ends has been linked to the Peltier effect which causes heating at the anode-electrode junction and cooling at the cathode-electrode junction.

In-situ observation of oxygen mobility and abnormal lattice expansion in ceria during flash sintering

Using in situ energy dispersive x-ray diffraction (EDXRD) the average specimen temperature of TiO$_2$ in the steady state of flash is experimentally determined. Comparison

of the microstructure for flash sintering and conventional sintering in addition to the temperature determined from calibration of the unit cell expansion indicates that rapid Joule heating during flash sintering causes densification and grain growth comparable with conventional sintering. An average temperature approximation model is proposed to account for greybody radiation and thermal conduction. Using profile scans the inhomogeneity of the grain growth across the sample length is confirmed to be the result of inhomogeneity in temperature distribution and this is related to the current flow induced Peltier effect in n-type TiO_2.

2.3 CeO$_2$

In-situ observation of oxygen mobility and abnormal lattice expansion in ceria during flash sintering

Flash sintering has been shown to be an effective method of sintering for many types of ceramics. However, the characteristics of flash sintering for each type of ceramic varies. When ionically conducting ceramics are sintered under a DC electric field, a strong dependence of densification with respect to position is observed. Microstructural analysis of the effect of electric field on oxygen ion conductors shows non-stoichiometry (oxygen deficiency) at the cathode which continues to build up over time under flash. In oxygen ion conductors, dominant charge carriers during flash are oxygen ions and the final density of the specimen is related to the availability of oxygen. This effect is no longer evident when using an AC power supply. Thus, use of AC instead of DC electric field is preferable for flash sintering of ionically conducting ceramics.

3. Experimental Methods

3.1 Flash Sintering

Most flash sintering experiments are performed on ceramic green compacts in either a dogbone (6-8, 10-12, 14, 16, 17, 21, 25, 27, 29-32, 34-37, 39, 43-45, 47, 49, 53, 54, 62, 64, 66-71, 76, 78-80, 82, 84, 86-89, 91, 92, 102, 107, 108, 110, 111, 113-115, 117-119, 124, 127-129, 146, 148, 150, 169-173, 175-178) or pellet (15, 18, 22, 26, 33, 50-52, 55-61, 63, 72-75, 81, 83, 90, 93-101, 103, 105, 106, 109, 112, 116, 120-122, 125, 126, 130-140, 145, 147, 149, 179, 180) shape.

A schematic of the dogbone is given in Fig. 16 as most commonly used by Raj's group (43). Dogbone specimen typically have very thin cross sectional area in the gauge section with the "ears" of the dogbone allowing current to concentrate inwards by the time it gets to the gauge section. This helps to minimize current localization as the current distribution is more evenly distributed. The dogbone specimen are typically suspended by platinum wires within the furnace, which minimizes heat loss during flash due to thermal conduction. The issue with dogbone specimen is the same as their strength. Their geometry is tuned for optimal current flow, but that also makes them inherently unscalable. It's hard to imagine bulk ceramics made with 1.5-2mm x 3.3mm gauge sections. In addition, a majority of the material are in the "ears" of the dogbone, which do not sinter and are thrown away after the experiment is completed.
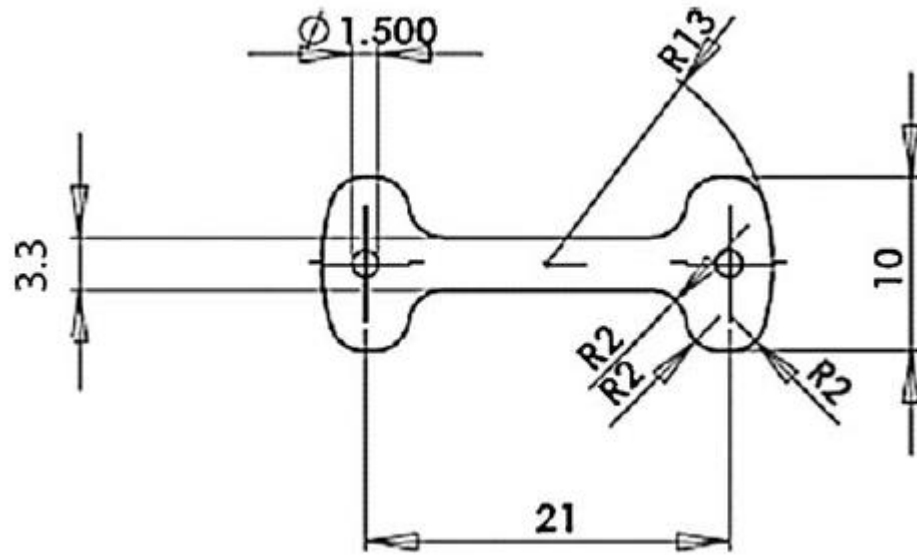
Figure 16: Schematic of most common dogbone design. The holes on the ends are where the platinum wires are looped to create the electric potential (43).

Pellet specimen are typically wedged between platinum electrodes which are themselves wedged between non-conducting (typically alumina) stage and pushrod. Pellet specimen are more likely to be used in future applications. If flash sintering of a 1 cm diameter specimen works then flash sintering of a 2 cm may also work and scaling is possible. The current study exclusively used cylindrical pellets of 6 mm diameter and varying thickness. Even at 6 mm, the cross sectional area is several times that of a dogbone.

The electric field is applied across the cylinder thickness using one of a variety of power supplies. BK 9115 is a high current DC power supply, V=0-80V and I=0-60A. BK PVS10005 is a high voltage DC power supply, V=0-1000V and I=0-5A. Pacific 118ACX is an AC power supply with frequency range f=45-1200Hz, V=0-150V and I=0-10A. The temperature is controlled using a purpose built temperature controller using Eurotherm 2404 controller and Epack SCR. A custom LabVIEW program has been written to control

the applied electric field and current limit as well as to record the electric field, current density, power density, furnace temperature, and linear displacement output data. An alumina tube stage with top pushrod is used with platinum wires coiled on both faces of the bottom base and top pushrod and extending to the top of the tube. The tube is placed inside a custom furnace heated using Kanthal A-1 (iron-chromium-aluminium alloy) wire pre-coiled around a long ¼" screw and then wrapped inside alumina-silica hard insulation. This furnace configuration can reach temperatures up to 1100 °C at a rate of $10\ °C \cdot min^{-1}$ and up to 1200 °C at a rate of $5\ °C \cdot min^{-1}$. An outer alumina tube is surrounded by the heating element and surrounds the alumina stage. The experimental setup is summarized in Fig. 17.
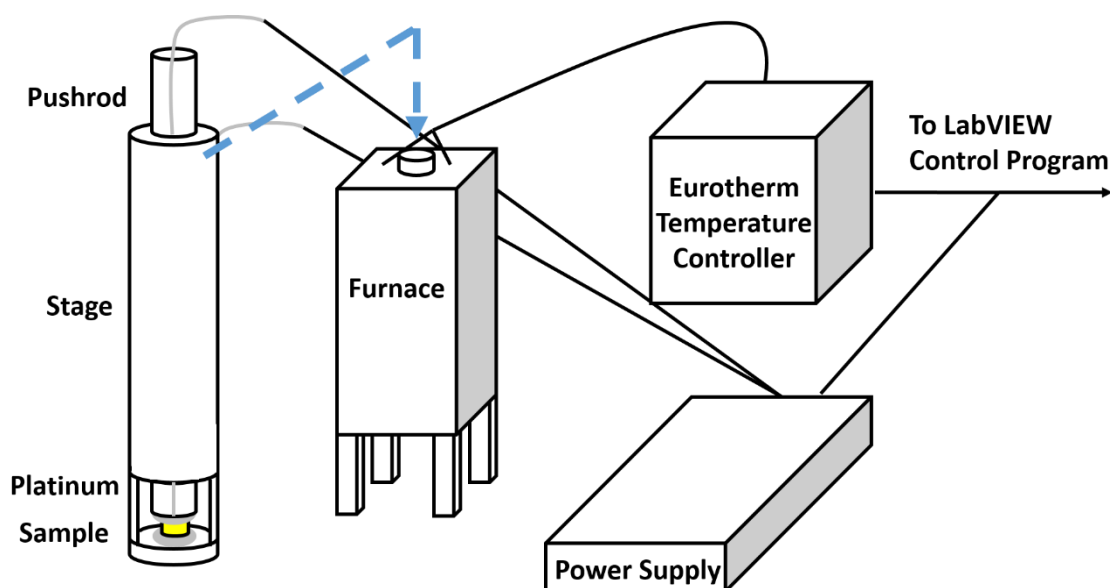
Figure 17: Experimental setup for flash sintering experiments.

3.2 Energy Dispersive X-Ray Diffraction

In a synchrotron, electrons, are injected from a linear accelerator into a synchrotron booster ring surrounded by a series of electromagnets. The electromagnets accelerate electrons from sub-GeV energies to GeV energies. These electrons are then injected into a storage ring, a much larger ring of electromagnets, which keeps the electrons cycling within the ring. The synchrotron has many types of magnets to control the orbit of the electrons in the storage ring. Each sector at the APS has two bending magnets, one of which serves as a source of x-rays for a bending magnet beamline. As the electrons are kept continuously cycling in the storage ring by bending magnets they have a centripetal acceleration which produces X-rays with a polychromatic range of energies, referred to as white light X-ray radiation. At different locations tangent to the storage ring X -rays are allowed to pass to the beamline site where various extra steps are applied depending on the type of X-ray characterization technique at a particular beamline. A schematic of the synchrotron setup is given in Fig. 18.
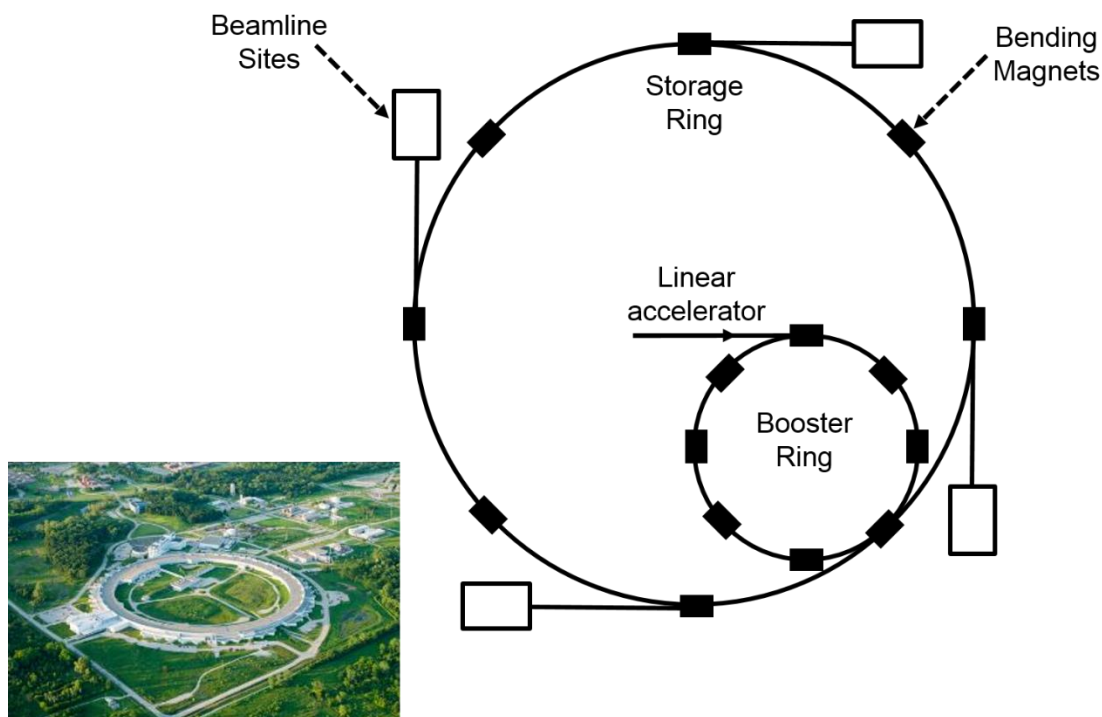
Figure 18: Aerial view (181) and schematic of a synchrotron facility with electrons accelerated from linear accelerator to booster ring and kept revolving around the storage ring using bending magnets. Beamline sites are located tangent to the storage ring to collect x-rays as the electrons continually release them due to the force provided by the bending magnets.

At Beamline 6-BM-A, Energy Dispersive X-Ray Diffraction (EDXRD) is used to study in situ d-spacing of crystalline materials. Laboratory-based X-Ray Diffraction (XRD) utilizes a monochromatic source of radiation provided by excitation of electrons from the heating up of a tungsten tip source. These electrons are used to bombard a copper substrate which then ejects a spectrum of white light x-ray radiation. The incident beam strikes a well-ordered crystal monochromator, which absorbs the radiation and produces a diffraction peak that serves as a monochromatic source for the sample.

Monochromatic radiation uses two parallel crystals of silicon to diffract the x-ray beam twice at an angle. By changing the angle, the wavelength of monochromatic light can

be tuned for specific applications. In addition, lab based Cu x-ray sources are ~8 keV while the x-rays used by the synchrotron beamlines are in the 60-180 keV range, allowing the x-rays to transmit through the samples. Thus, with synchrotron sources studies of the bulk material are possible at much faster rates in transmission mode.

EDXRD is an advantageous technique for in situ bulk characterization of materials and has the added advantage of using the full spectrum of white light x-ray radiation, so a single, stationary detector can be used instead of a moving detector or an area detector. In EDXRD a conical region of angle 2θ is transmitted from which the diffraction pattern can be chosen. In single crystal materials where there is a single direction of diffraction for each crystal plane, the position on the circumference must be chosen carefully. However, for polycrystalline materials this is not a concern as the beam will pass through many grains of random orientation. The energy spectrum in EDXRD is analogous to the 2θ angle so an energy dispersive detector can be inserted at one fixed position instead of varying the angle, which increases the acquisition time for the spectrum. An alternative using monochromatic radiation would require placing a series of detectors at a full 2θ range, creating an area detector.
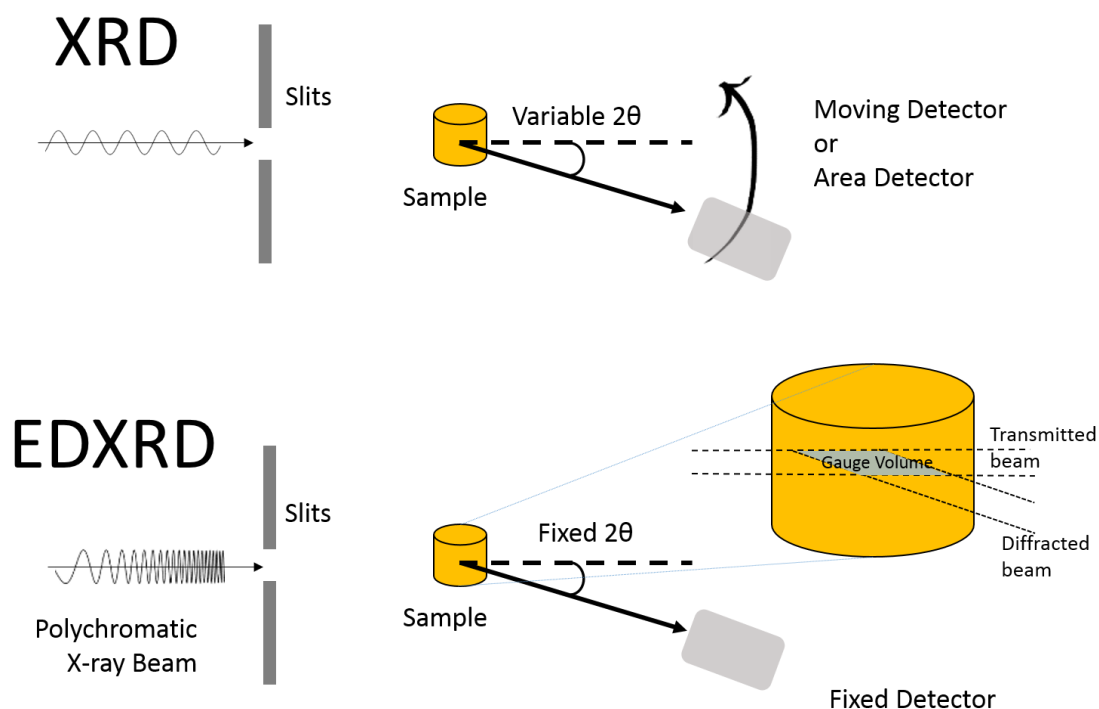
Figure 19: Schematic summary of energy dispersive X-ray diffraction (EDXRD) contrasted with traditional, monochromatic X-ray diffraction (XRD) (170).

The following procedure has been taken primarily from a previous work (169) and has been used in a number of published and submitted works (169-171). The detector is placed at an angle with respect to the incident beam, in this case $2\theta \sim 3°$, measuring one part of the diffraction ring. For nanometer and submicron sized particles the gauge volume contains enough grains with random orientations to avoid texturing effects. However, as average grain size increases to tens of microns the orientation of the large grains affects the counts collected at that particular site on the diffraction ring and can skew the diffraction pattern. The incident beam slits are limited to a X mm x Y mm cross sectional area, typically 0.2 mm x 1 mm in the following experiments, to balance intensity requirements

to the constraints of the furnace such that the gauge volume is small enough to avoid collecting data from the surrounding stage.

For conventional heating counts are collected over a 60 second period, roughly coinciding to 1 scan / 10 °C. Since conventional sintering is a slow process 60 seconds is still a fast enough acquisition rate to track the sample properties. For the profile scans collected over the specimen length, from positive to negative electrode, a short acquisition time measuring in <5s is taken per position with a ~5s delay to change the sample position using the automated xyz stage. Each profile scan covers a full section of the sample height and the stage is shifted in vertical steps for the remaining scans.

X-rays are collected in a germanium detector. The Ge detector converts x-rays into electron-hole pairs with the number of e-h pairs proportional to the x-ray energy. A -500 V bias voltage causes these pairs to separate. The x-rays are detected as a voltage pulse so this signal is amplified and the spectrum is collected. A multi-channel analyzer (MCA) collects the spectrum and displays it in terms of channel number versus counts. The channel number is proportional to x-ray energy. These frequencies, corresponding to energies, are reciprocal to the d-spacing in real space and calibration standards are used to convert the data from channel to energy to d-spacing. Using 8YSZ and CeO_2 as calibration standards yield the fitting constants, which are then used to determine energy and interplanar spacing of the studied material. The spectra for both the calibration standards and the studied materials are fitted using a purpose built MATLAB fitting program approximating the peaks to a Pseudo-Voigt shape. This process is summarized schematically in Fig. 20.
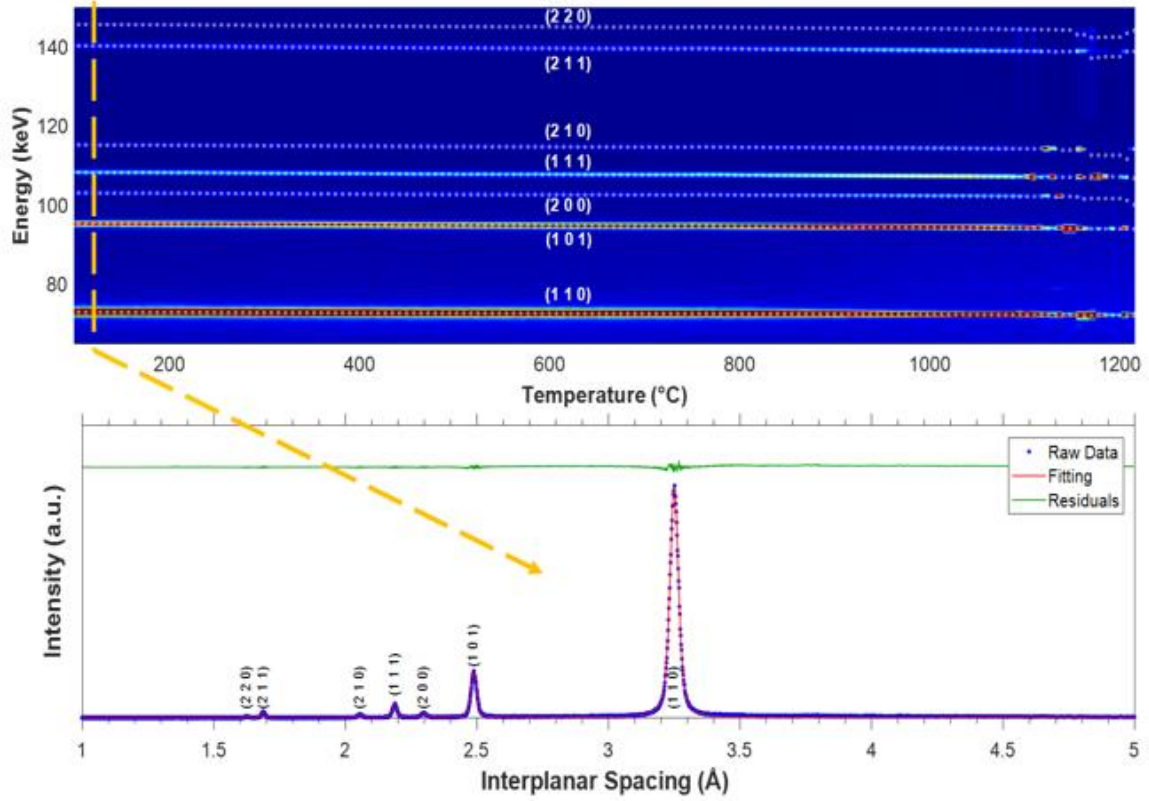
Figure 20: The fitting process of the EDXRD spectra involves the conversion of channel number to energy in reciprocal space to d-spacing. The spectra are then fit with a Pseudo-Voigt function. The contour plot is taken for conventional heating of TiO2 to 1200 °C (169).

The derivation of the equations used to convert to energy and d-spacing are given below. According to Bragg's law,

$$n\lambda = 2d_{hkl} \sin\theta, \tag{3.2.1}$$

where n is a positive integer, taken as 1, λ is the incident wavelength d_{hkl} is the d-spacing of the Miller index, hkl. Since the energy of a photon, $E = h\nu = hc/\lambda$, with Planck's constant $h = 6.626 \times 10^{-34}$ J·s,

$$E_{hkl}(keV) = \frac{hc}{2d_{hkl} \sin\theta} = \frac{6.1992(keV \cdot \text{Å})}{d_{hkl} \sin\theta}, \tag{3.2.2}$$

The x-rays are collected in a germanium detector where channel number is proportional to the energy of the x-ray. Thus,

$$E_{hkl} = A + B * channel, \tag{3.2.3}$$

from which the d-spacing of the diffracted beam can be calculated using equation 3.2.2.

Fitting is performed with a Pseudo-Voigt approximation (P), a convolution of Gaussian (G) and Lorentzian (L) functions,

$$P(A_i, B_i, C_i, D_i, x) = D_i * G(A_i, B_i, C_i, x) + (1 - D_i) * L(A_i, B_i, C_i, x) \tag{3.2.4}$$

where

$$G(A_i, B_i, C_i, x) = A_i * \exp\left[-4 * \log(2) * \left(\frac{x - b_i}{c_i}\right)^2\right] \tag{3.2.5}$$

and

$$L(A_i, B_i, C_i, x) = \frac{A_i}{1 + 4 * \left(\frac{x - B_i}{C_i}\right)^2} \tag{3.2.6}$$

In equations 3.2.4-3.2.6 the parameters are defined: A is the peak intensity, B is the x-axis position of the peak center, C is the full width at half maximum, and D is the Pseudo-Voigt parameter such that $0 < D < 1$ where $D = 0$ corresponds to an ideal Lorentzian function and $D = 1$ corresponds to an ideal Gaussian function. The variable, x, is the x-axis position which corresponds to channel (unitless), energy (keV), or interplanar spacing (Å) depending on the spectrum. The fitting program takes a sum of these Pseudo-Voigt functions such that

$$P_{total} = \sum_{i=1}^{N} P(A_i, B_i, C_i, D_i, x) \tag{3.2.7}$$

with N total peaks.

3.3 Spectroscopy

3.3.1 X-Ray Photoelectron Spectroscopy

X-Ray Photoelectron Spectroscopy (XPS) uses a beam of X-rays focused on a small region, which causes the ejection of core shell electrons from the studied material. The electrons are collected by a detector, with the electron energy recorded over a wide range. Every atom core level electron has a unique energy footprint based on the attraction of the atomic nucleus and this can be converted to a binding energy. In addition, the interaction of different bond types, i.e. oxygen-metal bonds or oxygen-carbon bonds, slightly changes the binding energy, which allows for further information to be collected.

While the X-rays can penetrate deep into the material, the ejected electrons have limited mean free paths as they interact with the surrounding crystal lattice. The penetration depth that can be resolved for XPS is low, on the order of nanometers. Thus, XPS is a surface sensitive technique and by changing the grazing angle of the X-ray beam the penetration depth can also be changed. Taking a series of scans with different grazing angles, one can determine the change in composition near the surface of the specimen.

The experimental procedure and data that is collected has been taken primarily from a previous work in section 5.1 and follows here (176). The specimen chemistry was analyzed using ThermoFisher K-Alpha X-Ray Photoelectron Spectroscopy (XPS) with 1486.7 eV X-ray photon energy and 400µm spot size. Three spots were mapped at different

sections of the cross-section area: cathode, middle, and anode. After completion of a survey scan over a binding energy range from 1350 eV – 0 eV with 1 eV step size, the specific regions 298 eV – 279 eV (C1s), 475 eV – 448 eV (Ti2p), and 545 eV – 525 eV (O1s) were scanned in detail (see Fig. 21) for each position.
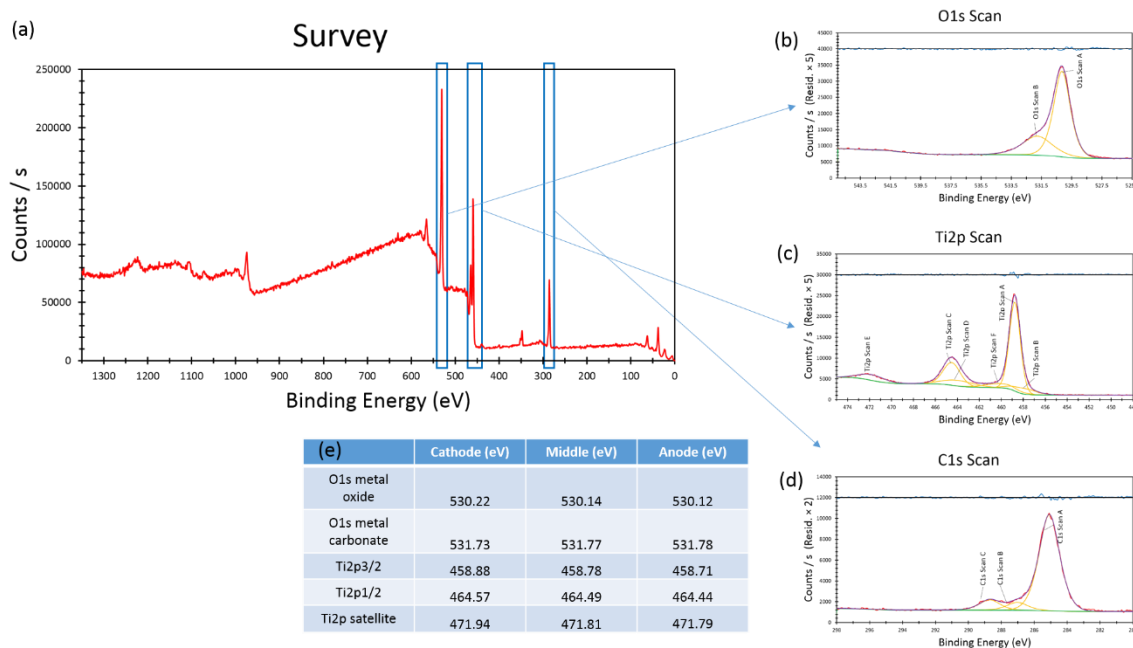
Figure 21: XPS survey plot (a) and detailed fitting for binding energies for (b) O1s, (c) Ti2p, and (d) C1s core level excitations. (e) The binding energies for selected O1s and Ti2p peaks have been estimated for cathode, middle, and anode.

3.3.2 Raman Spectroscopy

Raman Spectroscopy is a technique that uses a focused laser on a flat sample surface. The reflected beam is scattered depending on the crystal structure and composition of the sample surface, which tells a great deal of information about the sample chemistry and bond structure. Peaks in the Raman spectrum are caused by specific bending, stretch, and other modes of the bonds. A shift in these peaks indicates the incorporation of dopants,

for example. A change in intensity indicates the level of crystallinity as seen in section 5.1. Using a Renishaw InVia Raman MicroSpectroscopy the Raman Spectra are analyzed in different positions of the sample, which can be linked to non-homogeneity or density of defects at different positions. This method was used to study changes along the thickness of rutile TiO_2 and compared to a conventionally sintered standard with a spot size of ~1 μm and Raman shift from 100-700 cm^{-1} (176).

3.3.3 Impedance Spectroscopy

Impedance Spectroscopy is a valuable technique in measuring small changes in composition. As many techniques require careful preparation of a sample surface or have sensitivity that is insufficient to measure small changes in stoichiometry, impedance spectroscopy can fill the void. A constant voltage is applied across the sample using silver electrodes. The frequency of the voltage is swept over a wide range, which induces a change in the phase angle and impedance depending on the frequency applied.

The total impedance is a complex quantity,

$$Z = Z' - jZ'' \,, \tag{3.3.3.1}$$

where Z' is the real part of the impedance and Z'' is the imaginary part of the impedance. The impedance modulus, $Z_{mod} = |Z|$, is the magnitude of the complex impedance while phase angle, Z_θ, is the phase shift between the applied voltage and the current such that $0 \leq Z_\theta \leq 1$. Both quantities are are used to find the real and imaginary parts of the impedance, Z' and Z'' by the following expressions,

$$Z' = Re(Z) = Z_{mod} \cos(Z_\theta) \tag{3.3.3.2}$$

$$Z'' = Im(Z) = Z_{mod} \sin(Z_\theta). \tag{3.3.3.3}$$

For a perfect resistor there is no complex part to the impedance as there is no delay in the current, $Z_\theta = 0°$, so $Z_R = R$ where R is the resistance. For a perfect capacity there is no real part to the impedance as there is only a delay in the current, $Z_\theta = -90°$, so $Z_C = \frac{1}{j\omega C}$ where $j = \sqrt{-1}$, $\omega = 2\pi f$ is the angular frequency, and C is the capacitance. For a ceramic single crystal in the ideal case the impedance can be modelled as an RC circuit in parallel with impedance

$$Z = Z_R + Z_C = R + \frac{1}{j\omega C} \tag{3.3.3.4}$$

In real materials the capacitive behavior is imperfect and should be modeled with a constant phase element (CPE). The impedance of a constant phase element is given by Eq. 3.3.3.5,

$$Z_{CPE} = \frac{1}{(j\omega)^\alpha Y_0}, \tag{3.3.3.5}$$

where the $0 < \alpha < 1$ and Y_0 is analogous to the capacitance. For $\alpha = 0$ the system is a pure resistor while for $\alpha = 1$ the system is a perfect capacitor.

For polycrystalline ceramics there are generally two combined R-CPE circuits corresponding to bulk and grain boundary impedance. Generally the relaxation frequency of the grain boundary impedance is at a lower frequency in comparison to the bulk impedance. In addition, the lower the impedance values the higher the specimen conductivity.
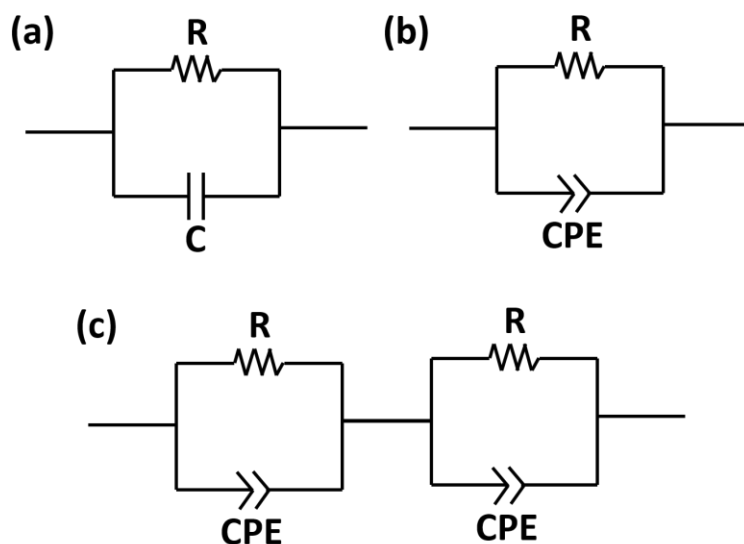
Figure 22: (a) R-C circuit, (b) R-CPE circuit, and (c) 2 R-CPE circuits in series.

In this case a Gamry Reference 600+ potentiostat was used to perform the measurements and to produce the Nyquist plots of Z' vs $-Z''$. For the case of ZnO conductivity studied for specimens sintered at differing current ramp rates, (175), the samples were tested at to 100°C with 500 mV applied voltage over a frequency range from 5 Hz – 5MHz.

3.4 Electron Microscopy

3.4.1 Scanning Electron Microscopy

Scanning Electron Microscopy (SEM) allowed for grain size and porosity approximations A Zeiss Sigma Field Emission SEM was used in the studies. The sputtering of 10-15nm gold coating onto the surface of the specimen was determined based on the material composition. For samples that had been polished a thermal etching treatment at

~250℃ below the conventional sintering temperature was carried out in air for 5 hours. Lince software developed by Darmstadt University of Technology was used to estimate the average grain size and standard deviation following the linear intercept method. ImageJ software was used to estimate porosity in polished specimens.

3.4.2 Transmission Electron Microscopy

The experimental procedure for TEM analysis was performed by Haiyan Wang's group at Purdue University. A brief summary of the experimental procedure has been taken from Jha, et al. (171) and repeated in the following. Plan-view TEM samples were prepared through grinding, polishing, dimpling and final polishing in a precision ion milling system (PIPS II, Gatan). A FEI TALOS TEM/STEM with ChemiSTEM technology (X-FEG and SuperX EDS with four silicon drift detectors) operated at 200 kV was used in this study for microstructure characterization and energy-dispersive X-ray spectroscopy (EDS) chemical mapping.

4. ZnO – Temperature Approximation, Current Ramp Rate, and Conductivity Comparison

4.1 Investigation of Temperature Approximation Methods during Flash Sintering of ZnO

4.1.1 Disclaimer

4.1.2 Introduction

Zinc oxide is an n-type, II-VI semiconductor with a wide bandgap of ~3.3eV at room temperature (182). It has many applications including use in gas sensors (183), varistors (184), optoelectronics, and piezoelectronics. Conventional sintering of ZnO has been extensively studied (160, 185-188) to determine the effects of time, temperature, grain

size and grain growth mechanisms. In the present work the response of ZnO to an applied

electrical field in order to improve understanding of flash sintering was studied, which has

been shown to densify ceramics at much higher rates at relatively lower temperatures (6,

49). Within the flash sintering community, zinc oxide is one of the most widely studied

material systems (94-99).

Flash sintering, a new process invented in 2010 (6), takes place when an electric

field is applied to a ceramic specimen at a sufficiently high temperature to cause a nonlinear

rise in specimen conductivity. This nonlinear rise in conductivity allows current to flow

through the specimen which causes rapid densification at furnace temperatures well below

those required for conventional sintering (189). Unlike the case of spark plasma sintering

(SPS), the current flows entirely through the sample rather than through a conductive die

(189).

The mechanism for rapid densification is under debate. Originally, there are three

proposed mechanisms put forth to explain this enhanced diffusion. First, a thermal runaway

effect in which current flows through the sample, inducing Joule heating which increases

the conductivity of the specimen (30, 95). This increase in conductivity allows a higher

current density which then results in more heating in a feedback loop. High temperatures

can be reached rapidly, higher than the temperature required for conventional sintering or

rapidly enough that a fast firing effect takes place, avoiding grain coarsening that normally

occurs during a gradual increase in temperature (166, 167, 190). A second proposed

mechanism is local heating at the grain boundary due to higher resistance compared with

the bulk. However, the temperature gradient required for maintaining local heating at the

grain boundary was calculated to be prohibitively high (191). The third mechanism is an

avalanche of defects at relatively high temperature, a combination of some Joule heating and the influence of the electric field, which can explain the high rate of sintering (29, 155, 192) and other unusual aspects of flash sintering such as electroluminescence (25, 29), phase transformation (27, 86), texture (82), and change of electrical conduction mechanism (79).

Luo's group has concluded that the nonlinear rise in conductivity of ZnO can be attributed to thermal runaway and that the primary mechanism for the densification of ZnO under flash conditions is Joule heating (95). Evidence for this conclusion comes from the blackbody radiation model developed to estimate the rise in temperature of yttria-stabilized tetragonal zirconia under a weak electrical field (155),

$$T = [T_0^4 + \frac{W}{\varepsilon A \sigma}]^{1/4}, \hspace{4cm} (4.1.1)$$

where T is the specimen temperature (K), T_0 is the furnace temperature (K), W is the total power through the sample (W), σ is the Stefan-Boltzmann constant (5.67 x 10^{-12} Wcm^{-2}K^{-4}), and A is the surface area of the sample (cm^2). Zhang, et al. (95, 99) calculated temperatures ranging from 1002°C with J=3.1A/cm^2 to 1407°C with J=12.4A/cm^2. This same model has been used in 3mol% yttria-stabilized zirconia (3YSZ) to support both Frenkel defect generation (155) and thermal runaway (30) as the primary mechanism.

It is important to note two issues when using a blackbody radiation model for flash sintering: first, the assumption of an emissivity equal to 1 for all materials (95) and second, omission of the requirement that the model is valid for ΔT/T<<1 (8). For significant temperature increases the blackbody radiation model, commonly used in flash sintering temperature approximations, is invalid. Emissivity is 1 for black body only, for ceramics they vary (always < 1) depending on the temperature and wavelength of the light.

Additionally, the voltage through the sample is used to calculate the power through the sample, which is inserted into Equation 5.1.1. A 4-point measurement of voltage drop due to contact resistance on 8YSZ clearly shows that it is too significant to avoid (193). The linear shrinkage due to densification has not been considered. While the first factor overestimates the temperature, the second factor underestimates the temperature. Pyrometry has also been used to measure the temperature of the specimen during flash (155). Such a technique is problematic if the optical luminescence characteristics from the flash event are different than radiation from an assumed black body at a different temperature1. In addition, only the surface temperature is measured (194).

It is the intention to resolve the question of temperature rise during flash sintering by using in-situ energy dispersive x-ray diffraction (EDXRD). In-situ study of flash sintering using a synchrotron x-ray source was first used by the Tsakalakos research group to study flash sintering of 8YSZ (52). Thus, a measure of the lattice expansion of ZnO during flash sintering was compared with a conventionally heated sample. Using this reference, the first goal of this study will be to determine the temperature, under varying current densities, by comparing the unit cell volumes to that of the conventionally heated calibration standard. The second goal of this study is to compare the densification and grain growth behavior of samples densified under applied electric field and current flow to that of conventionally sintered samples at comparable temperatures.

4.1.3 Experimental Procedure

Sample Preparation

Pure zinc oxide nanopowder, with <100 nm particle size from Sigma-Aldrich (544906, Lot# MKCB2717V). Cylindrical pellets with dimensions, 3±0.1mm thickness and 6mm diameter, were pressed in a stainless steel die using a 150MPa uniaxial load. Geometric measurements indicate green body density of 60±3%.

Specimens were heated at a rate of 10°C/min, dwelled at their respective temperatures for 60s, and then cooled at a rate of 25°C/min. Flash experiments were performed isothermally at 800 °C, at which point a DC (direct current) electric field of 60V/cm was applied to the specimen. Platinum paste was applied to both ends of the disc and platinum wires wrapped around the alumina rods were used to establish electrical contact to the power supply. A small weight equivalent to 10 kPa was used to maintain consistent electrical contact between the electrodes and the sample. Under an electric field of 60V/cm, differing current limits of 5, 10, 15, 20, 25, and 30A/cm^2 were applied.

After a few seconds of incubation period (91), there was a nonlinear rise of conductivity during which some densification occurred. The power supply switched to current control at a predetermined current limit after which the sample was allowed to continue to densify under a steady state electric field determined by the conductivity of specimen and set current limit. After 60 seconds under current control the power supply is turned off and the furnace is allowed to cool at a rate of 25°C/min. A typical example of a flash sintering profile with the current density, electric field, calculated power density and corresponding densification is shown in Fig. 23.
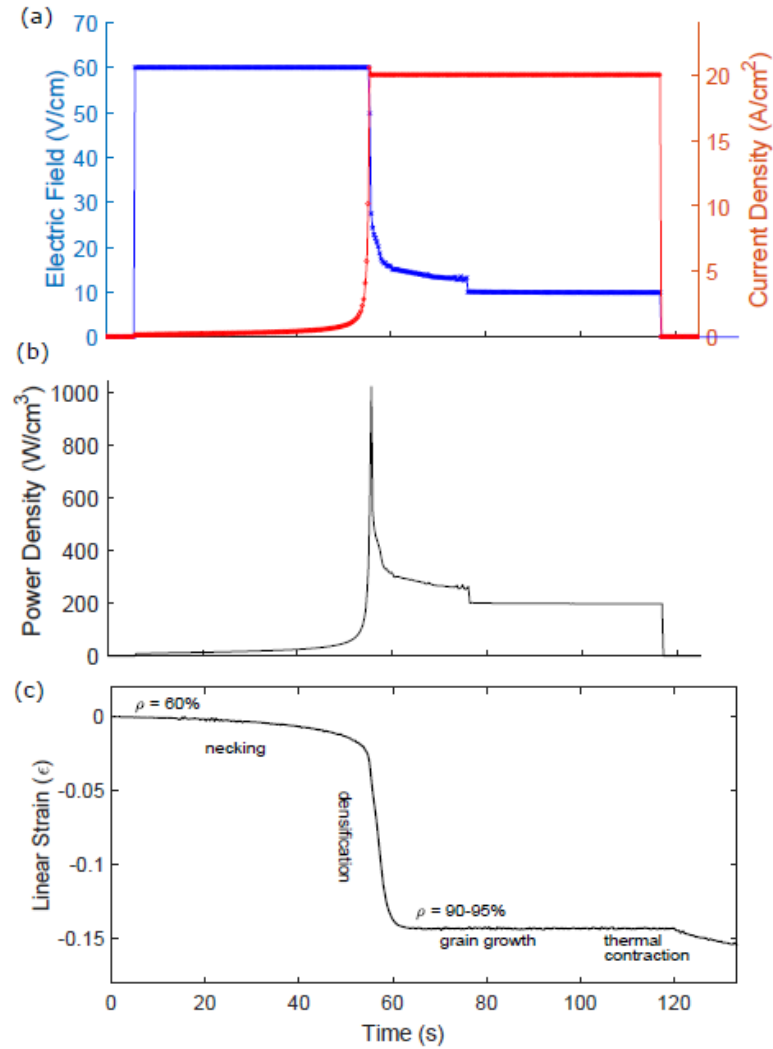
Figure 23: (a) A time synchronized plot of the electric field (E) applied at electrodes that results in rise in current density (J) through the specimen. The power density (P) through the sample is given in (b), where P=EJ. (c) shows the densification with flash.

Argonne Data Acquisition

At the Synchrotron facility at Argonne National Laboratory the real time change in lattice parameter during flash sintering was observed. White beam x-ray radiation with Energy Dispersive X-ray Diffraction (EDXRD) technique was used in contrast to monochromatic wavelength XRD, with schematic shown in Fig. 19. One advantage of EDXRD is the ability to detect the diffraction signal at a single point. The complete scan of equivalent 2θ, in the case of monochromatic beam, can be performed at the same time

without moving the detector and the second technique, since diffraction data can be obtained only from the gauge volume, spatial resolution was used to look at any part of the sample while diffraction from other materials in the path of the beam are filtered out. In other words, a specimen can be placed in a completely enclosed furnace while patterns are collected from the specimen only. Once the energy spectrum is collected, it is saved with a channel range from 1 to 8192. A calibration is used on a specimen with known lattice parameters to convert the channels into energy of radiation (which is comparable to 2θ in normal XRD with monochromatic beam). The spectra can further be converted into d-spacing and the method is included in Appendix A.

The XRD patterns are collected while the specimens are conventionally heated to the desired furnace temperature and then flashed. One XRD scan is taken effectively every 2.3 seconds. A MATLAB code has been written to synchronize the flash data, acquired using LabVIEW, with EDXRD data. Fig. 25 is an example of one flash sintering experiment with contour plot from EDXRD data. Every vertical scan is a pattern converted into d-spacing (Fig. 25c) and Fig. 25d shows the shift in the d spacing for peak (100) as the specimen undergoes the flash.
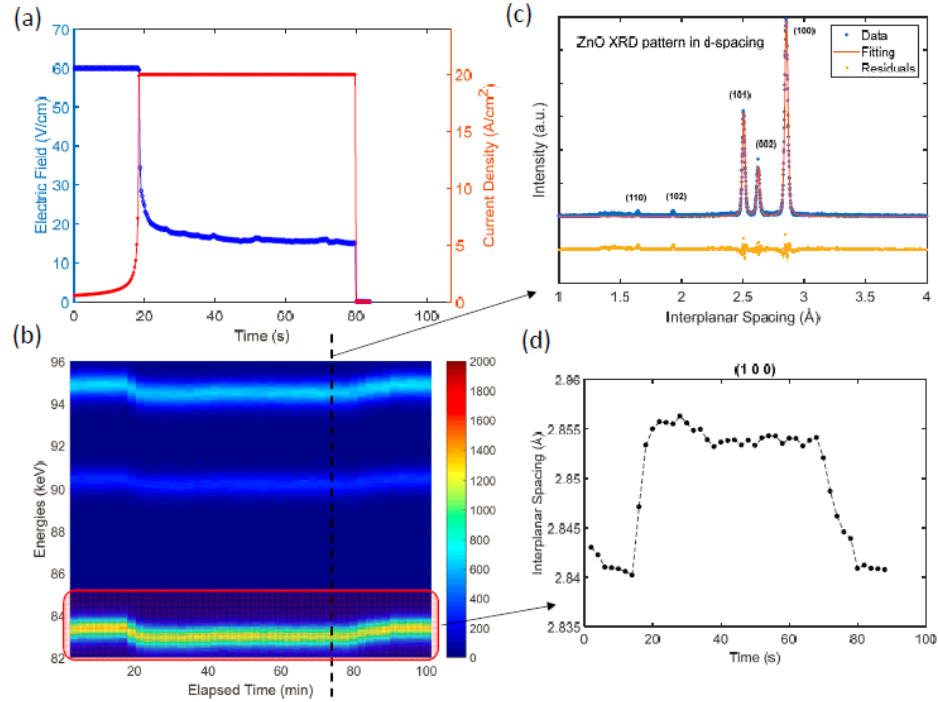
Figure 24: (a) Power density through specimen during flash sintering with 20 A/cm2 (b) shows the colorplot for the flash with X axis shows the time and Y axis is the energy of diffracted beam. If one takes a vertical line, that gives us a XRD pattern, an example is shown in (c) with peaks identified. We can also follow the change in lattice parameter by a pseudo Voigt fitting of certain peaks: for example, peak (100) of ZnO is shown in (d).

To estimate the actual temperature of the specimen during flash sintering, a ZnO sample was conventionally heated up to 1150°C and the interplanar spacing from peaks (101) and (100) were used to calculate lattice parameters a and c for the hexagonal ZnO unit cell. The calculation is shown in Appendix B. Using the lattice parameters, a and c, the total unit cell volume of the lattice was calculated with respect to temperature, as shown in Fig. 26. This calibration was used to estimate the specimen temperature during flash sintering, assuming that there wasn't any unusual lattice expansion caused by defect generation. If there were some measurable contribution from defect generation to the strain then the actual temperature of the specimen, it would have been even lower than the estimated temperature from the calibration specimen. Our temperature estimation is,

therefore, the upper limit of the temperature. An empirical quadratic equation is fitted to the data to find out the specimen temperature (Appendix B).
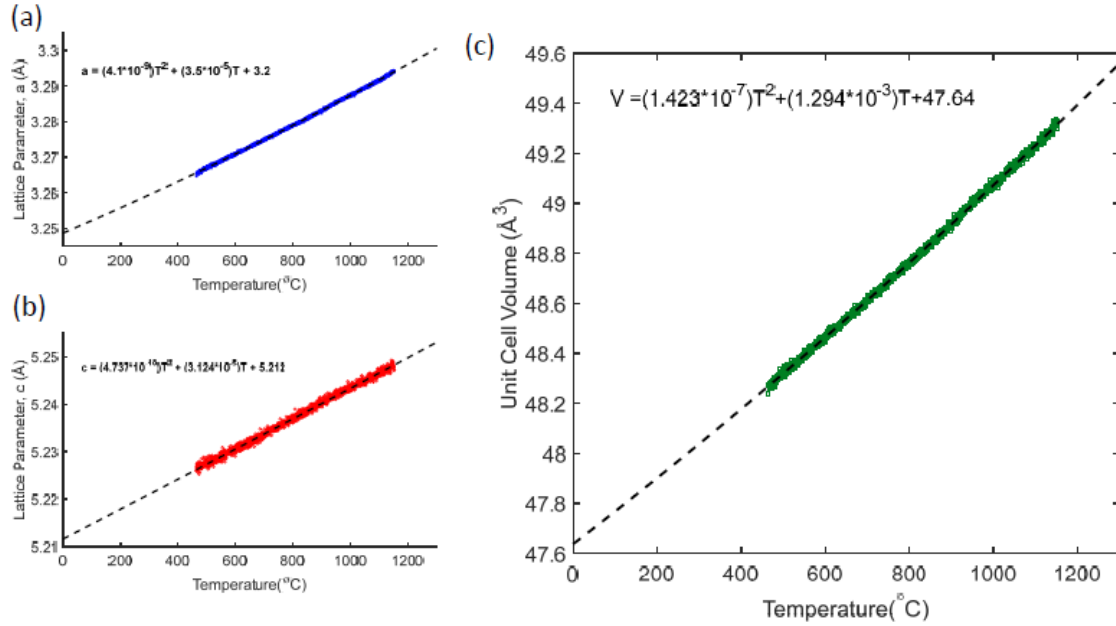
Figure 25: Lattice parameter expansion of (a) 'a' and (b) 'c' with temperature. Unit cell volume calibration using furnace temperature is used to estimate the actual sample temperature under flash (c).

Scanning Electron Microscopy

Scanning electron microscopy (SEM) was carried out using a field-emission microscope (Zeiss Sigma Field Emission SEM) to characterize the microstructures. Fractured surfaces were seen microscopically in order to avoid the possibility of grain growth during thermal etching. A 15nm gold coating was sputtered onto the specimens to avoid charging.

4.1.4 Results

At Argonne different current density limits ranging from 5 A/cm2 to 30 A/cm2 were applied. The power density plot (Fig. 27 (a)) shows that power density increases with current density. The corresponding unit cell volume expansion, shown in Fig. 27 (b), demonstrates a clear trend of higher lattice expansion when more current is allowed to pass through the specimen, indicating higher specimen temperature. Further details of the experiments, indicating specimen densities, grain sizes, and temperatures, are shown in Table 2. An error range is given based on differential lattice expansion during the 60 seconds of current-controlled flash sintering. There have been suggestions of (146) local melting at the grain boundaries which would have caused densification, however, no change in the unit cell volume during the power spike (when a transition from voltage control to current control was applied), which would indicate temperatures sufficient for melting, was observed.
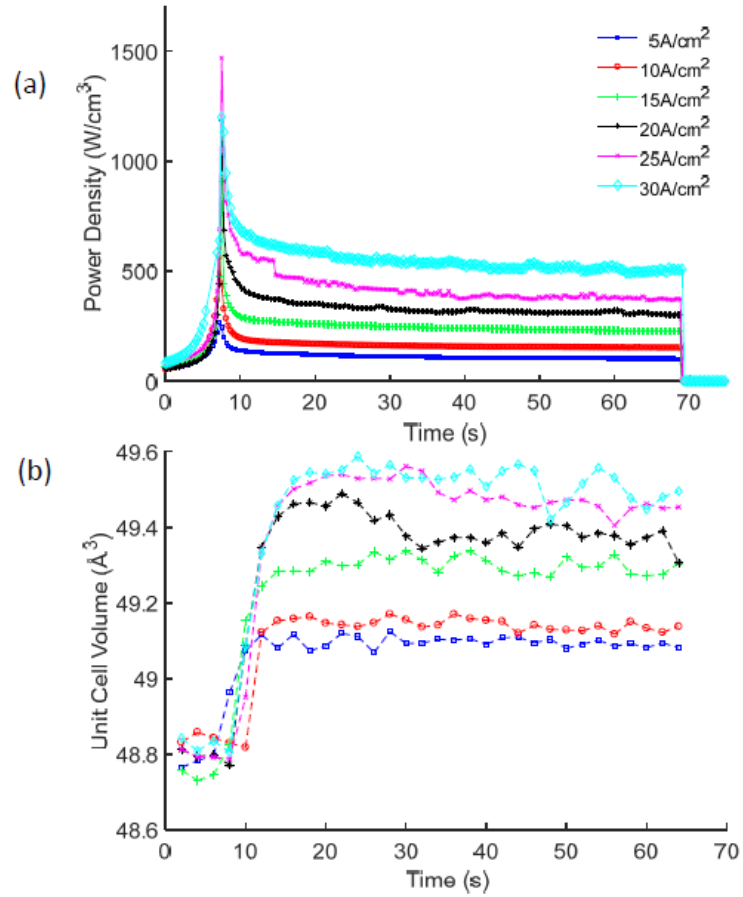
Figure 26: (a) Power density through specimen during flash sintering and (b) accompanying unit cell volume expansion. Current densities from 5-30A/cm2 are analyzed.

Table 2: Comparison of density, temperature, and grain size in conventional sintering and flash sintering.

Conventional Sintering Furnace Temperature (°C)	Flash Sintering						
	ρ/ρ_{th} (%)	Grain Size (µm)	J (A/cm^2)	Temperature EDXRD (°C)	Temperature Blackbody (°C)	ρ/ρ_{th} (%)	Grain Size (µm)
800	66	0.1-0.3	5	1010	1198	86	0.2-0.5
900	82	0.1-0.4	10	1050	1354	95	0.5-1.5
1000	88	0.3-0.8	15	1140	1482	94	0.8-2
1100	92	0.8-2	20	1200	1621	95	1-3
1200	92	2-4	25	1260	1718	94	2-4
1300	92	4-6	30	1280	1861	95	2-5

To understand the effect of flash on the change in shape of peaks, a test case condition of 20 A/cm^2 was performed and analyzed, thus the change in full width at half maximum (FWHM) and peak height intensity with lattice expansion is shown in Fig. 28. The FWHM and intensity have been normalized with their corresponding maximum value for comparison. What is interesting to note, is that at the advent of flash, sudden jump in d spacing and FWHM with a corresponding dip in the intensity is observed. After 60 seconds of current control, when the flash is turned off, the d-spacing goes down gradually. This occurs due to fast, adiabatic heating during the flash spike, which is also noticed in densification (Fig. 23(c)), and then cooling to thermal equilibrium with the furnace. The sudden jump in FWHM, can come from either abnormal defect generation (52) or due to shift of the peak with temperature rise during relatively long acquisition time of synchrotron in comparison to the fast heating of the specimen. The result from the experiments on ZnO indicate there may be an effect of flash in defect formation, but it is less prominent in semi-conductors like ZnO when compared with the results of 8YSZ (52).
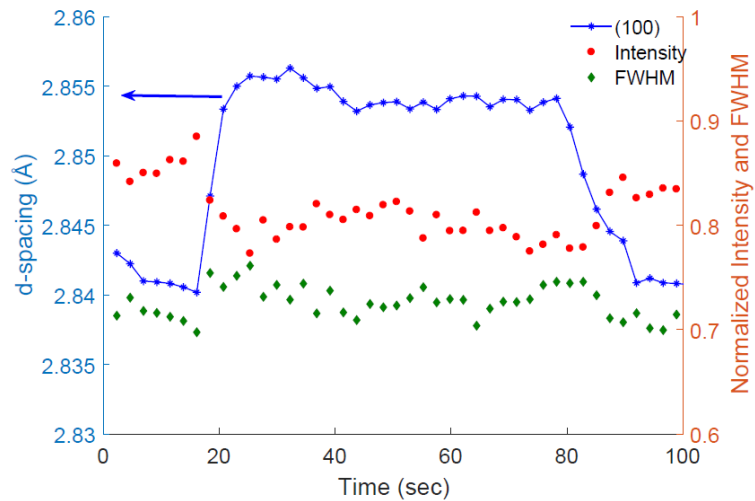
Figure 27: A flash experiment with 20 Acm^{-2} and corresponding peak analysis for (100) includes increase in d-spacing, full width half maxima (FWHM) and peak intensity.

Results of the temperature calibration using unit cell volume with calculations from the blackbody radiation model, was compared. Isothermal furnace temperature was $T_0 =$ 800 °C and the surface area measured after cooling was used in the blackbody radiation equation. The blackbody radiation model suggests significantly higher temperatures than the actual measured temperatures and the gap widens as current density is increased, as shown in Fig. 29. It is important to note, that 10 A/cm^2 is enough current to sinter ZnO to high density at 800 °C. The temperatures calculated using the blackbody radiation model are a lowest approximation because the minimum power was applied though the specimen during stage III. If the blackbody radiation model at face value is used then at the current cutoff where there is a power spike it would be expected that the samples would exceed the melting point of ZnO, 1977 °C (195).
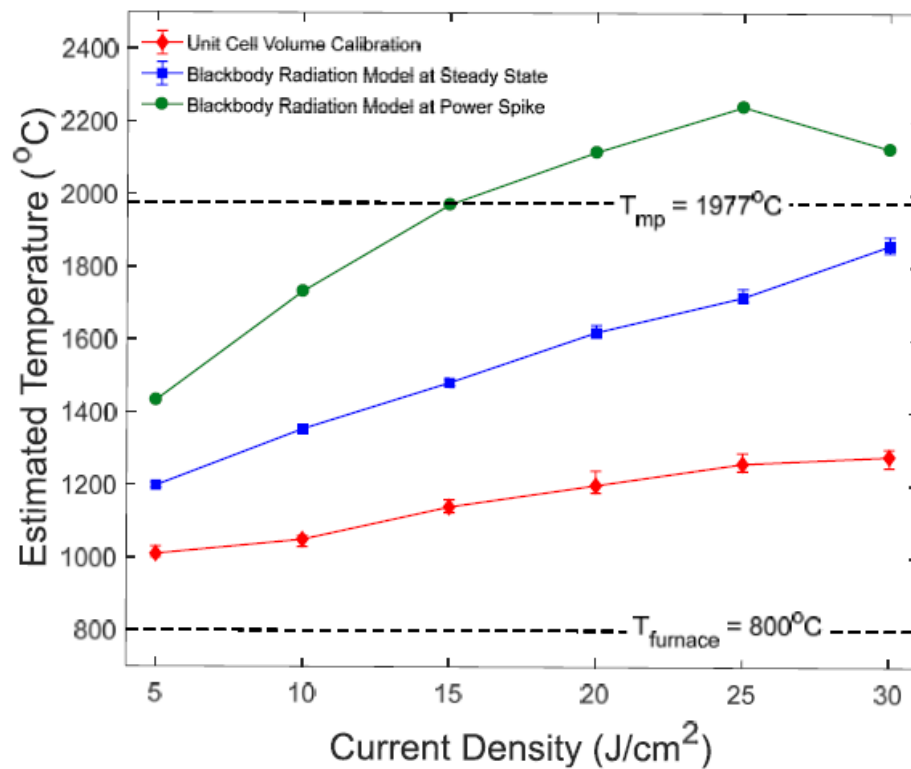
Figure 28: Comparison of estimated temperatures using thermal expansion of the unit cell volume to calculated temperatures using the blackbody radiation model.

Corresponding SEM analysis of fracture surfaces in Fig. 30 indicates that densification occurs with modestly lower grain growth during flash sintering when compared to conventional sintering. Evidence of melting predicted according to the blackbody radiation model temperatures is not found in the microstructure. Instead the microstructure is comparable to conventionally sintered specimens in the temperature range predicted by our unit cell volume calibration.
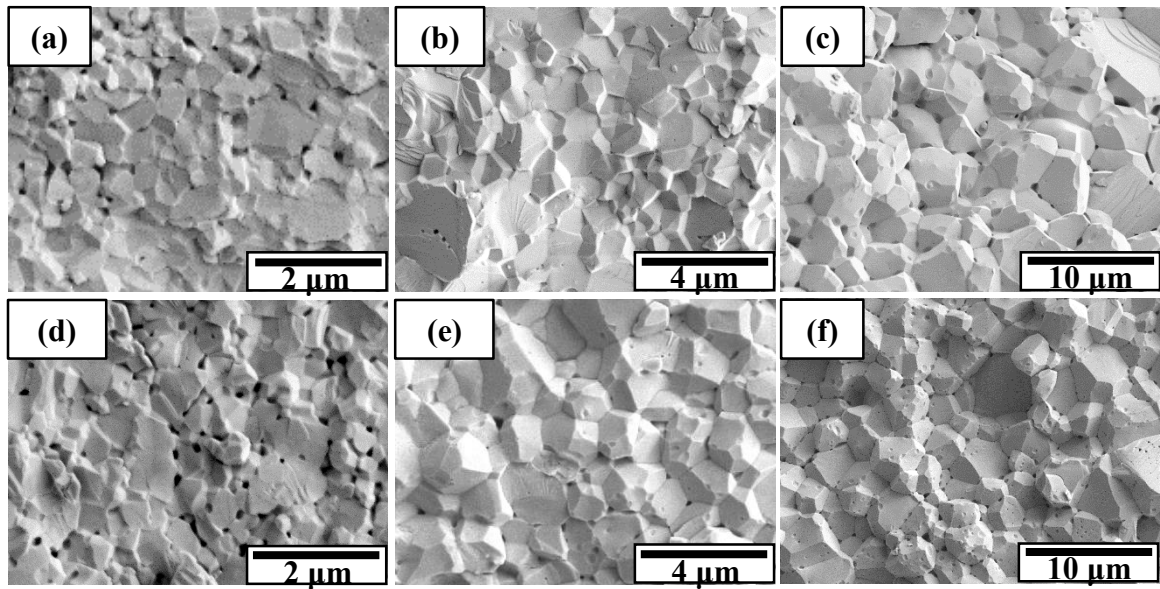
Figure 29: Microstructure comparison for flash sintered specimens versus conventionally sintered specimens. Conventionally sintered specimens dwelled for 1 minute at 1000 °C, 1100 °C, and 1300 °C, respectively, are shown in (a), (b), and (c) while (d), (e), and (f) show flash sintered specimens with current-controlled hold time of 1 minute at 5A/cm^2, 10A/cm^2, and 30A/cm^2, respectively.

There has been debate on the contribution of the power spike seen during the transition from voltage control to current control. However, the ephemeral nature of the fast transition does not allow enough time to understand this transition using in-situ diffraction, as explained in the analysis of the FWHM. To avoid the power spike we can go into current control at a very low current density (0.5 A/cm^2) and ramp the current at a

linear rate by controlling the electric field with a PID control. It is discovered that the kinetics of densification are proportional to the power density through the specimen. The theory of thermal runaway is invalidated since the temperature rise is in equilibrium with electrical power throughout the experiment.

4.1.5 Discussion

We question the reliability of the use of blackbody radiation model to correctly predict sample temperature. If the real power density through the specimen can be measured by 4-point contact measurement, it may give a better approximation, but it still is susceptible to the assumption of ΔT and ϵ. Sample geometry plays an important role as well, since the equilibrium between radiation dynamics and power through the specimen determines the actual temperature (79). In our opinion, the blackbody radiation model should be used with caution and must be verified with other techniques.

In this study, it is shown, that comparing the expansion of the unit cell volume in conventional heating to flash sintering provides an accurate measure of the temperature of the specimen. The thermal expansion of the material provides experimental verification of specimen temperature that is reasonably within the bounds of the final specimen microstructure.

The temperatures reached during flash sintering of ZnO are comparable to those of conventional sintering. However, the time spent at high temperature is much lower than in conventional sintering. The improved densification may be due to a fast firing effect (166, 167, 190), but the phenomenon of an avalanche of Frenkel defects, formed under the influence of the applied electric field, cannot be ruled out at these temperatures. This work

adds to a growing body of in situ XRD work relating to mechanisms and applications of flash sintering (Table 3). We have avoided the power spike to eliminate the uncertainty of abnormal heating in the current-ramp experiment. Using flash sintering at different current-density ramp rates may help to elucidate the effect of fast heating rates (we used 3 orders of magnitude) on the grain boundary morphology, but that is being considered in another work (175).

Table 3: Literature survey of current in situ XRD work related to flash sintering.

Material	Authors	Title	Study
8YSZ	Akdogan, et al (52)	Anomalous lattice expansion in yttria stabilized zirconia under simultaneous applied electric and thermal fields: A time-resolved in situ energy dispersive x-ray diffractometry study with an ultrahigh energy synchrotron probe	Anomalous change of full width at half maximum
CeO2	Jha, et al (171)	In situ observation of oxygen mobility in ceria during flash sintering	Ionic diffusion and inhomogeneity
TiO2-Al2O3	Jha, et al (86)	Phase transformation in the alumina–titania system during flash sintering experiments	Chemical kinetics with temperature
TiO2	Jha, et al (82)	Electric field induced texture in titania during experiments related to flash sintering	Generation of texture
TiO2	Yoon, et al (84)	Measurement of O and Ti atom displacements in TiO2 during flash sintering experiments	Pair distributive function of Ti and O under flash
TiB2-TiO2-TiBO3	Özdemir, et al (112)	Electric field effect on chemical and phase equilibria in nano-TiB2–TiO2–TiBO3 system at <650 °C: an in situ time-resolved energy dispersive x-ray diffraction study with an ultrahigh energy synchrotron probe	Chemical and phase equilibria
3YSZ	Lebrun, et al (27)	Emergence and Extinction of a New Phase During On–Off Experiments Related to Flash Sintering of 3YSZ	Emergence of metastable phase
3YSZ	Teradus, et al (29)	Electroluminescence and the measurement of temperature during Stage III of flash sintering experiments	Electroluminescence and temperature estimate
3YSZ	Lebrun, et al (32)	Broadening of Diffraction Peak Widths and Temperature Non-uniformity During Flash Experiments	Inhomogeneous lattice expansion

4.1.6 Appendix A

According to the Planck-Einstein relation the x-ray photon energy is

$$E = h\nu \,, \hspace{6cm} (4.1.A1)$$

where h=4.16.626×10⁻³⁴J·s, Planck's constant, and ν is the photon frequency, $\nu = \frac{c}{\lambda}$.

Bragg's law states

$$n\lambda = 2d_{hkl} \sin \theta \tag{4.1.A2}$$

where d_{hkl} is the interplanar spacing in the crystal lattice with Miller indices, hkl. Taking n=1 and inserting Eq. (4.1.A1) into (4.1.A2) we find,

$$E_{hkl}(keV) = \frac{hc}{2d_{hkl} \sin \theta} = \frac{6.199}{d_{hkl} \sin \theta} \tag{4.1.A3}$$

A germanium detector is used to collect the x-ray spectrum of the specimen. The slits were moved to give a beam flux with $\Delta x = 1$mm and $\Delta y = 0.2$mm. The acquisition time was taken at 2.3 seconds per spectrum in order to give enough counts for accurate peak fitting and a short enough time to get an accurate picture of the different stages of flash sintering.

$$E = a + b * channel \tag{4.1.A4}$$

a = 0.0991, b = 0.0347, θ = 1.501 degrees

Energy can be further converted into d-spacing by using Eq. (4.1.A3).

4.1.7 Appendix B

ZnO has a wurtzite crystal structure, which is a hexagonal system. Thus, the lattice parameters are calculated using the symmetry of a hexagonal lattice given in Eq. (4.1.B1).

$$\frac{1}{d^2} = \frac{4}{3} \frac{h^2 + hk + k^2}{a^2} + \frac{l^2}{c^2} \tag{4.1.B1}$$

Two equations are required to solve this equation requiring the tracking of two peaks in the spectrum. The (1 0 0) and (0 0 2) peaks were used in calculations of the lattice parameters and unit cell volume. The lattice parameters, a and c, are given in Fig. 26.

Using the lattice parameter dependence on temperature we can calculate the unit cell volume in the hexagonal system using Eq. (4.1.B2).

$$V = \frac{\sqrt{3}}{2} a^2 c \qquad\qquad (4.1.B2)$$

From the unit cell volume data, we extrapolate a quadratic equation relating the unit cell volume to temperature.

$$Unit\ Cell\ Volume = V_{unit\ cell} = (1.423 * 10^{-7})T^2 + 0.001294T + 47.6 \qquad (4.1.B3)$$

Linear model Poly2:

curve(x) = p1*x^2 + p2*x + p3

Coefficients (with 95% confidence bounds):

p1 = 1.423e-07 (1.29e-07, 1.557e-07)

p2 = 0.001294 (0.001272, 0.001316)

p3 = 47.64 (47.63, 47.65)

The fitting of Eq. (4.1.B3) to the unit cell volume is shown in Fig. 26. At 25°C a unit cell volume of 47.67 Å^3 is calculated using Eq. (4.1.B2), in fair agreement with the literature value of 47.62 Å^3 (87, 196). This equation is then used to give an approximation of the temperature during flash at various current densities through reference to the unit cell volume expansion.

4.2 Flash Sintering Using Controlled Current Ramp

4.2.1 Disclaimer

This work has been published in the Journal of the European Ceramic Society (175). The author constructed the experimental apparatus and performed the experiments with the help of Dr. Shikhar K. Jha, Kent H. Christian, and Ryan T. Lay. The principal investigator of this work is Dr. Thomas Tsakalakos. This work was funded by the Office of Naval Research under Contract No. N00014-15-1-2492 and subaward from Purdue University under Contract No. 4104-78982-820133.

4.2.2 Introduction

In conventional flash sintering, the current rises nonlinearly to a set current limit, accompanied by a spike in the power density. This sudden power spike may cause hot spot formation, in which current preferentially channels through a small area, causing localized melting while other areas remain unsintered. By using a controlled current ramp early on the sudden power spike can be avoided. In addition, by changing the ramp rate material properties such as porosity, grain size and conductivity can be tuned.

Flash sintering is a new sintering method developed by Cologna and Raj to densify 3 mol% yttria stabilized zirconia (3YSZ) in under 5 seconds at 850 °C (6). This method has been applied to sinter a wide variety of ceramic materials (189, 194) at lower temperatures and shorter hold times than conventional sintering. There are three proposed mechanisms originally posited for flash sintering: ultra-fast heating (30, 37, 99), bulk mass

transport through defect generation (79, 91), and vacancy segregation and selective grain boundary melting (156, 158).

The first mechanism posits that Joule heating (30, 99) caused by the feedback between increased temperature and conductivity initiates the flash event and ultra-fast heating causes non-equilibrium grain boundaries to form while avoiding coarsening which is the reason for rapid densification (37).

Others believe that the temperature reached due to current induced Joule heating is below the conventional sintering temperature and, thus, is insufficient to explain the flash phenomenon. Instead, a combination of Joule heating and the nucleation of an avalanche of Frenkel defects, due to the effect of the electric field (91), enhances diffusion at a temperature significantly below conventional sintering.

A third mechanism postulates that there is a temperature gradient between the grain boundaries and the grain bulk. Thus, while the temperature reached in the bulk is not high enough for sintering, the temperature at the grain boundaries is high enough to induce local melting or softening at the grain boundaries, resulting in rapid diffusion along the grain boundaries (158). However, the thermal diffusivity of ceramics precludes a significant temperature variation in nanoscale ceramic grains. The thermal diffusivity of ZnO can be estimated from $\alpha = k/\rho c_p$, where α is thermal diffusivity, k is thermal conductivity, ρ is the density of the ceramic, and c_p is the specific heat capacity. In the case of zinc oxide, thermal conductivity of ZnO at 1000 °C is approximately $4 \, W \cdot m^{-1} \cdot K^{-1}$. (159) For simplicity, the specimen is taken to be fully dense, ρ=5.606 gcm-3. Finally, at 1000 °C, specific heat capacity is calculated to be 54.2 J mol-1K-1 according to fitting data from Robie, et al. (161), $c_p = 53.999 + 7.581 * 10^{-4}T - 5.868 * 10^5 T^{-2} - 127.50 T^{-\frac{1}{2}} +$

$1.9376 * 10^{-6} T^2$, which is equivalent to $0.6658 \ J \cdot g^{-1} \cdot K^{-1}$. Inserting all values into equation 1, the thermal diffusivity of ZnO at 1000 °C is calculated: $\alpha = 1.072 * 10^{-6} \ m^2 \cdot s^{-1}$. Following the procedure of Ji, et al. (37) the time, t, taken for temperature to distribute itself between two ends of a grain of diameter, x, can be calculated as $t = \dfrac{x^2}{\alpha}$. For x=100 nm, the maximum grain size of the ZnO powder according to the supplier, it would take on the order of 10 nanoseconds for the heat to distribute itself from one end of the grain to the other. Even assuming grain growth this would still be many orders of magnitude greater than the time of flash, which is several seconds at a minimum.

Based on previous work estimating the temperature during flash sintering of ZnO using energy dispersive x-ray diffraction (EDXRD) (170), the authors believe that rapid Joule heating is the most likely explanation for the enhanced diffusion, at least in the case of ZnO. As a result, it is critical that the heating rate should be controlled in order to achieve the desired microstructural and electrical properties. This is not possible in conventional flash sintering, where an applied, fixed voltage causes a nonlinear rise in conductivity at high temperature, which results in a feedback loop of rising current and conductivity. To avoid catastrophic thermal runaway, an abrupt switch to current control results in a power spike as the voltage drops rapidly to maintain constant current despite rising. This runaway current followed by an abrupt switch to current control results in a sharp and significant power spike through the material, which often leads to channeling of current at one spot, known as a hot spot (87). The power spike can be detrimental due to thermal shock during the sudden rise and drop in power. In addition, the microstructure of the resulting product is difficult to tune due to the uncontrolled rise in current in stage I, under voltage control.

Flash sintering can be alternatively controlled by switching to current control the moment the current rise becomes unstable and then controlling the rate at which the current rises to its maximum set limit, which will avoid the sharp power spike. Initial work towards this end has been performed by Jian Luo's group by applying a step-wise increase of the electric current (99) as well as a two-step current schedule akin to conventional two-step sintering (98). In addition, the properties of the ceramic can be adjusted by changing the heating rate through the use of different current ramp rates. The effect of fast firing was investigated by comparing the microstructure of ZnO specimen under a range of current ramp rates, differing by orders of magnitude, as well as to conventional flash sintering.

Zinc oxide (ZnO) is the chosen material for this study as the sintering of ZnO has been studied extensively for both conventional (160, 185-187, 190) and flash (94-101) sintering, thereby providing a standard from which to study the behavior of flash sintering, in general, without concerns of phase transformations or chemical reactions.

Impedance spectroscopy on 3YSZ has shown that flash sintering reduces the grain boundary thickness while increasing the concentration of oxygen vacancies near the grain boundaries (22). A similar study has been performed here on ZnO by measuring the complex impedance of specimens sintered by CS (conventional sintering), CF (conventional flash sintering), and CRF (current ramp flash sintering). Comparison of the Nyquist plot for conventional flash sintering and current ramp flash sintering is performed and shows the effect of defect formation and grain growth on the conductivity of ZnO densified using flash.

4.2.3 Experimental Procedure

Zinc oxide nanopowder, with a grain size<100 nm, purchased from Sigma Aldrich (544906, Lot# MKCB2717V), is pressed into cylindrical pellets with 6mm diameter and 5mm thickness using a uniaxial 200 MPa load. The initial green body density, measured geometrically, is 60-65%.

Three methods of sintering, conventional sintering (CS), conventional flash sintering (CF), and current ramp flash sintering (CRF) were compared. For CS, the sample was heated at a rate of $10 \, °C \cdot min^{-1}$ from room temperature until reaching 1000 °C, 1100 °C, and 1400 °C and then held for 1 minute at this temperature and cooled at a rate of 25°C $\cdot min^{-1}$ to room temperature. For the CF experiment, the sample was heated to 700°C at a rate of $10 \, °C \cdot min^{-1}$ at which point an electric field of $60 \, V \cdot cm^{-1}$ was applied with a preset current limit of $5 \, A \cdot cm^{-2}$. The sample was held in current control for 60 seconds before turning off the field. The furnace was then cooled at the same rate of $25 \, °C \cdot min^{-1}$.

In the four CRF experiments, rather than allowing the current to reach $5 \, A \cdot cm^{-2}$ under constant electric field before switching to current control, the switching to current control happens early on, at $0.5 \, A \cdot cm^{-2}$, and afterwards the current limit is increased linearly to $5 \, A \cdot cm^{-2}$ with a PID (proportional-integral-differential) system. The power is then switched off after 10 seconds at maximum current. This results in the avoidance of the large power spike characteristic of flash sintering. Four current ramp rate schedules are followed: $1 \, A \cdot cm^{-2} \cdot s^{-1}$ (4.5-second ramp), $0.1 \, A \cdot cm^{-2} \cdot s^{-1}$ (45-second ramp), $0.01 \, A \cdot cm^{-2} \cdot s^{-1}$ (7.5-minute ramp), and $0.001 \, A \cdot cm^{-2} \cdot s^{-1}$ (1.25-hour ramp). The slowest ramp rate ensures that there is no effect of rapid heating on the densification of the material.

A Zeiss Sigma Field Emission SEM is used to characterize the microstructure of the final prepared specimens. Fracture surfaces were used for the comparison to avoid the grain growth during thermal etching of polished surfaces. Grain sizes were estimated using linear intercept method with Lince software.

A Gamry Reference 600+ potentiostat was used to study the frequency response of ZnO densified under the different current ramp rates and compare these to conventional flash sintering. Samples were heated to 100°C, after which 500 mV was applied across the specimen with a frequency range of 5 MHz to 5 Hz and 10 data points per decade.

4.2.4 Results

A comparison of the current-density ramp rates is given in Fig. 31(a). A semilog plot is used to illustrate the current schedules due to the significant disparity between the fastest and slowest rates. The maximum power density through the sample during is inversely proportional to ramp rate, presented in Fig. 31(b). As shown in Fig. 32, a slower ramping of the current results in higher final density and larger grains despite the fact that the highest power density was found in the fastest ramp rate. A comparison of density and grain size is shown in Fig. 32 (e), where density was measured geometrically while grain size and standard deviation of grain size was measured using Lince software. Of note is the increasing standard deviation of grain size with respect to average grain size indicating abnormal grain growth.
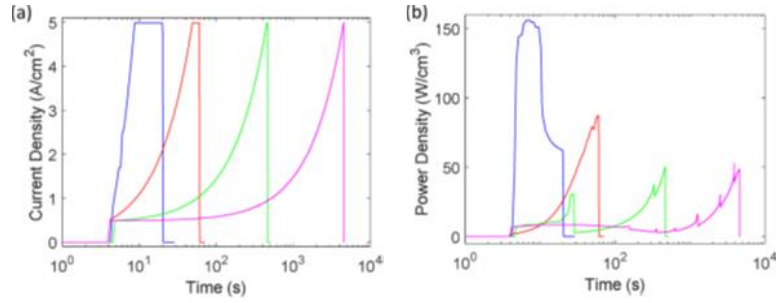
Figure 30: (a) Current ramp and (b) resulting power density at 1 A·cm^{-2}·s^{-1}, 0.1 A·cm^{-2}·s^{-1}, 0.01 A·cm^{-2}·s^{-1}, 0.001 A·cm^{-2}·s^{-1}.
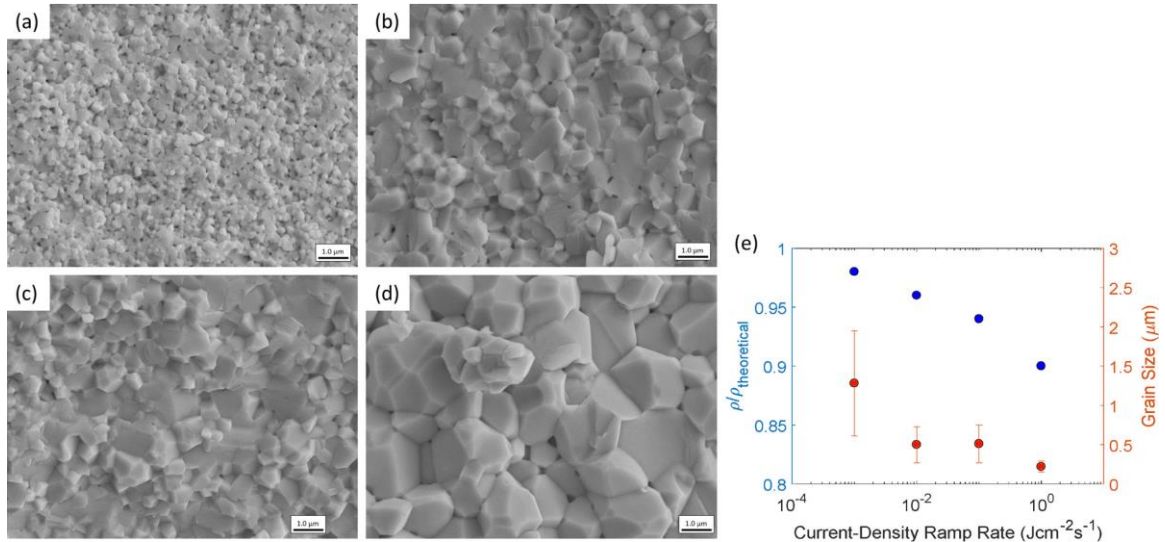
Figure 31: Grain size comparison at current ramp rates (a) 1 A·cm^{-2}·s^{-1}, (b) 0.1 A·cm^{-2}·s^{-1}, (c) 0.01 A·cm^{-2}·s^{-1}, and (d) 0.001 A·cm^{-2}·s^{-1}, from J = 0.5-5 A·cm^{-2} with 10 s hold time. (e) Semilog plot of density and grain size as a function of current-density ramp rate.

Fig. 33 provides a comparison of a conventional flash sintering experiment and a current ramp flash sintering experiment, with a ramp-rate of 0.1 A·cm^{-2}·s^{-1}. Despite having an even shorter flash time as lower power density, shown in Fig. 33(a), the grain growth in the current-ramp is higher than in conventional flash. There is a non-negligible effect of heating at the beginning of the ramp, 0.5 A·cm^{-2} in this case, where conventional flash sintering a current-ramp flash sintering are identical. However, as seen in Fig. 31, the power density at the beginning, before the system is put into ramp-current control is quite

small. This beginning current density is chosen to minimize the effects of heating on starting microstructure while still allowing the beginning of the nonlinear rise in conductivity.
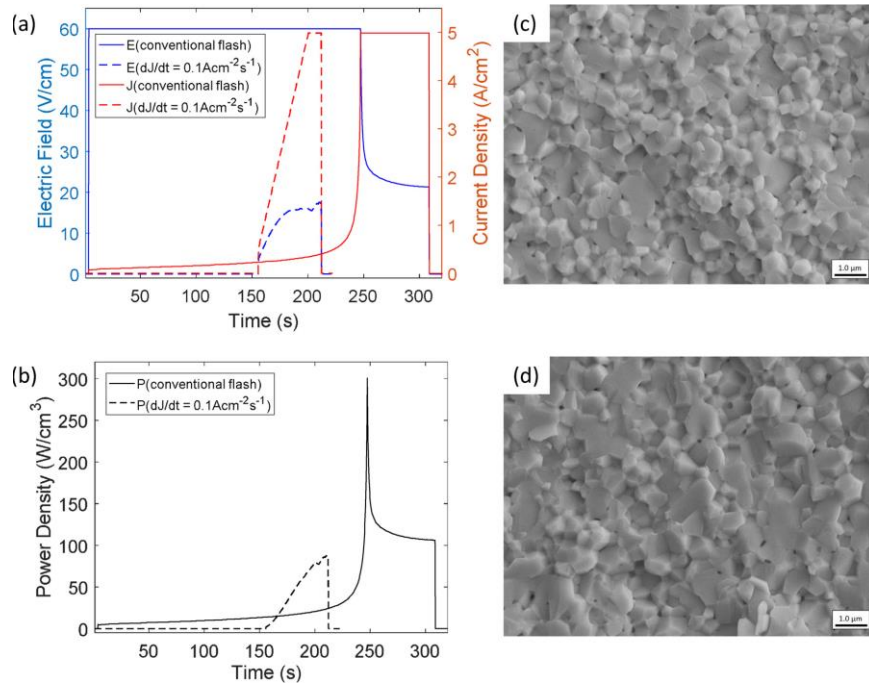
Figure 32: Current ramp flash sintering comparison to conventional flash sintering showing (a) electric field applied (E) and current density through the sample (J) with (b) resulting power density (P=EJ). Microstructure comparison shows that despite higher power density for lower time in conventional flash (c) compared with current ramp (d), grain growth is higher during current ramp.

Analysis of microstructure near the positive electrode, middle of specimen, and negative electrode is given in supplementary Figs. 34-36 for CF, $dJ/dt = 0.1 \text{ A} \cdot \text{cm}^{-2} \cdot \text{s}^{-1}$, and $dJ/dt = 1 \text{ A} \cdot \text{cm}^{-2} \cdot \text{s}^{-1}$. Interestingly, an electrode effect is observed for the highest ramp rate with grain size varying from 0.20 ± 0.70 μm to 0.26 ± 0.10 μm when moving from negative electrode to positive electrode, which has also been reported in the literature (50, 95). Zhang and Luo have reported the elimination of this effect under an Ar + 5% H_2 environment, which they attributed to the prevention of oxidation of ZnO near the positive

electrode in the presence of a reducing atmosphere (96). Flash sintering experiments using AC electric field have now shown this effect (35).
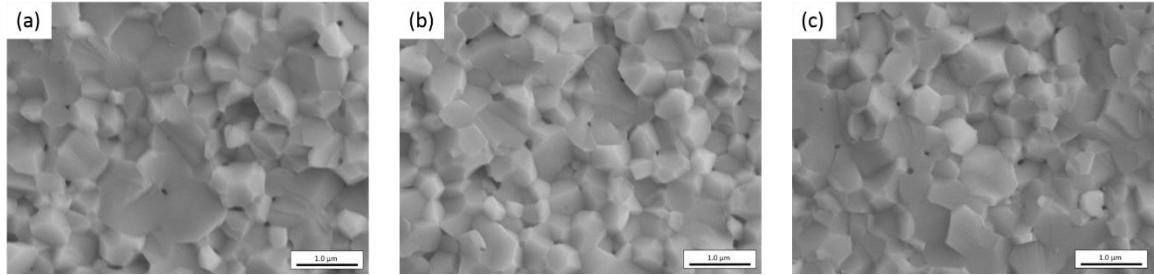
Figure 33: Microstructural comparison of a conventional flash sintering experiment with current cutoff of 5 A·cm^{-2} and 60 s hold time at (a) positive electrode, (b) center, and (c) negative electrode. Grain size varies from (a) 0.45 ± 0.21 μm to (b) 0.40 ± 0.16 μm to (c) 0.45 ± 0.17 μm.
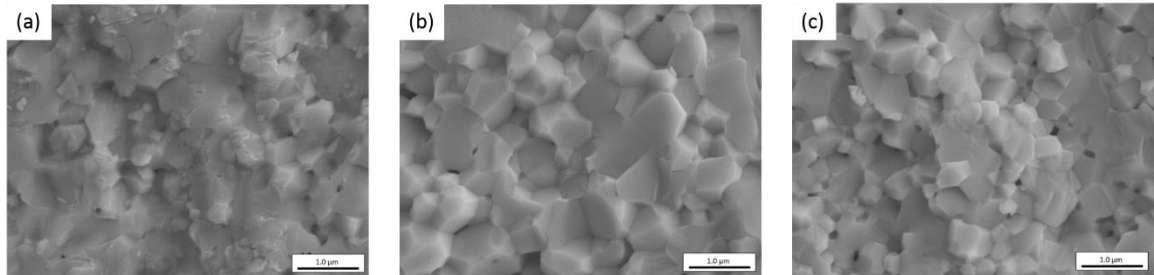
Figure 34: Microstructural comparison at (a) positive electrode, (b) center, and (c) negative electrode. Controlled flash sintering at a rate of 0.1 A·cm^{-2}·s^{-1} current ramp to 5 A·cm^{-2} with 10 s hold time. Grain size varies from (a) 0.39 ± 0.14 μm to (b) 0.51 ± 0.24 μm to (c) 0.37 ± 0.12 μm.
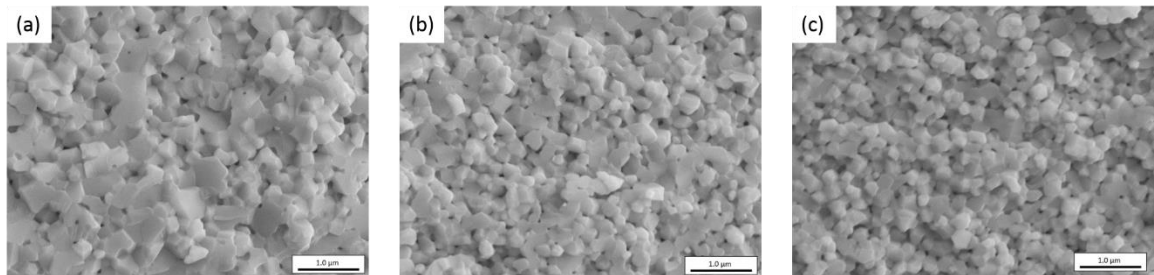
Figure 35: Microstructural comparison at (a) positive electrode, (b) center, and (c) negative electrode. Controlled flash sintering at a rate of 1 A·cm^{-2}·s^{-1} current ramp to 5 A·cm^{-2} with 10 s hold time. Grain size varies from (a) 0.26 ± 0.10 μm to (b) 0.22 ± 0.07 μm to (c) 0.20 ± 0.70 μm.

In Fig. 37 comparison of the Nyquist plots for the different ramp rates, with a conventional flash sintered specimen indicates that conductivity rises with a higher current ramp rate up to the very rapid, uncontrolled rate seen in conventional flash sintering. For a very slow rate the conductivity rises again.
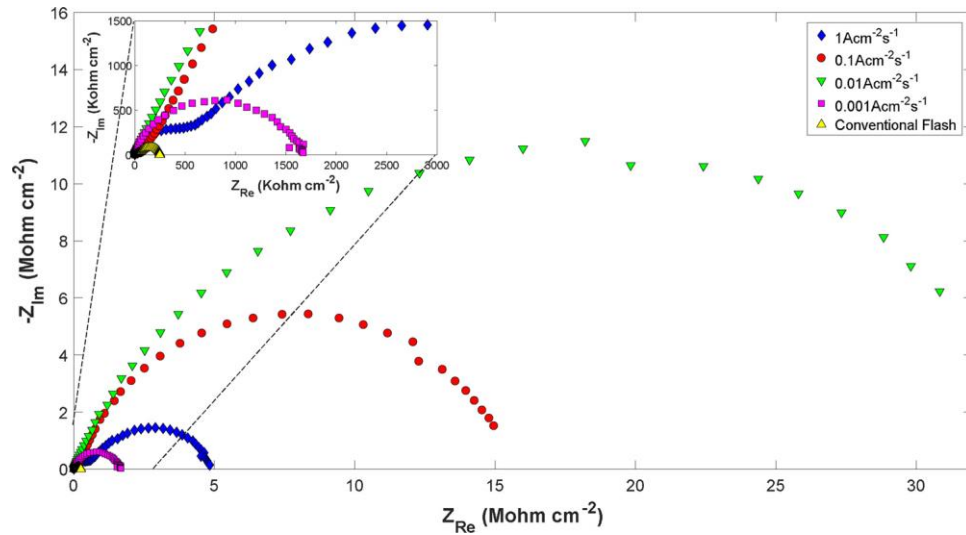
Figure 36: Nyquist plots of ZnO taken at 100 °C for varying current ramp rates compared with conventional, uncontrolled flash sintering. Inset shows a zoom of the smallest impedance responses.

4.2.5 Discussion

We show a new way of performing flash sintering by controlling the current proactively with a linear ramp rate rather than an abrupt maximum limit. The result of this controlled flash sintering is that we can tune the microstructure and electrical properties of ZnO by changing the rate.

It is important to address the enhanced grain growth of ZnO under current ramp compared with conventional flash sintering, despite the lower power through the sample.

ZnO is a well-studied ceramic system and, as has been thoroughly reported (95, 96, 99, 100, 160, 185, 186, 197-206), the densification and grain growth characteristics of ZnO is highly susceptible to changes in grain boundary composition.

Based on experimental results by Luo's group (100), we see that the temperature required for the onset of flash is inversely proportional to the starting grain size of the green body. This has been attributed to the enhanced electronic conduction of the surface layers, a critical factor in green bodies with small contacts between the grains. However, in our case we start with the same grain sizes at the onset of flash. Once flash has started the specimen temperature rises and sintering begins early on.

Grain coarsening is often caused by the competitive mechanisms of densification and grain growth. In the case of CF, the grains densify quickly and the curvature of the grains is replaced by more stable grain boundaries with near hexagonal grains. Once the curvature is removed the driving force for grain growth is reduced. However, as CRF is a slower process, this allows for grain growth before full densification is achieved. This effect may be on factor to explain enhanced grain coarsening despite lower power density during the slower ramp rates.

In addition, supplementary Figs. 38 and 39, comparing the grain size and corresponding Nyquist plots of conventionally sintered specimen, show that there is a clear correlation between grain size and conductivity. This effect is unrelated to flash sintering and is further confirmed in the literature, with significantly higher electrical conductivity of dense specimen of micrometer compared to nanometer sized grains (207, 208). For slower current-ramp rates, where more time is given for grain growth we see higher grain

growth which results in increased conductivity of the specimen. This is analogous to conventional sintering at different ramp rates.
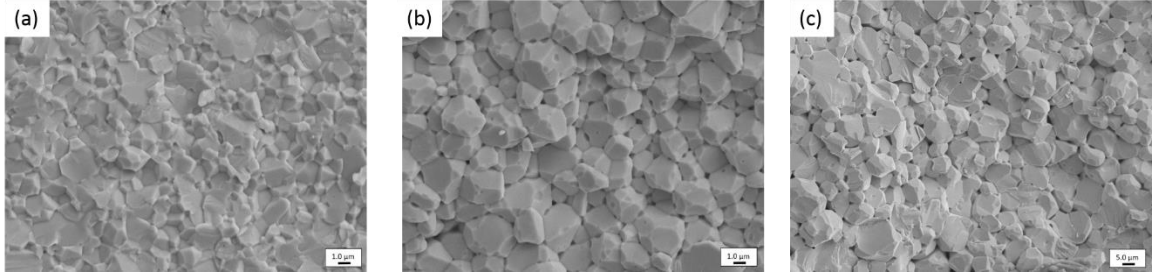
Figure 37: Comparison of ZnO heated to varying maximum temperatures of (a) 1000 °C, (b) 1100 °C, and (c) 1400 °C. Densification ceases by 1000 °C and microstructural change is dominated by grain growth at higher temperatures.
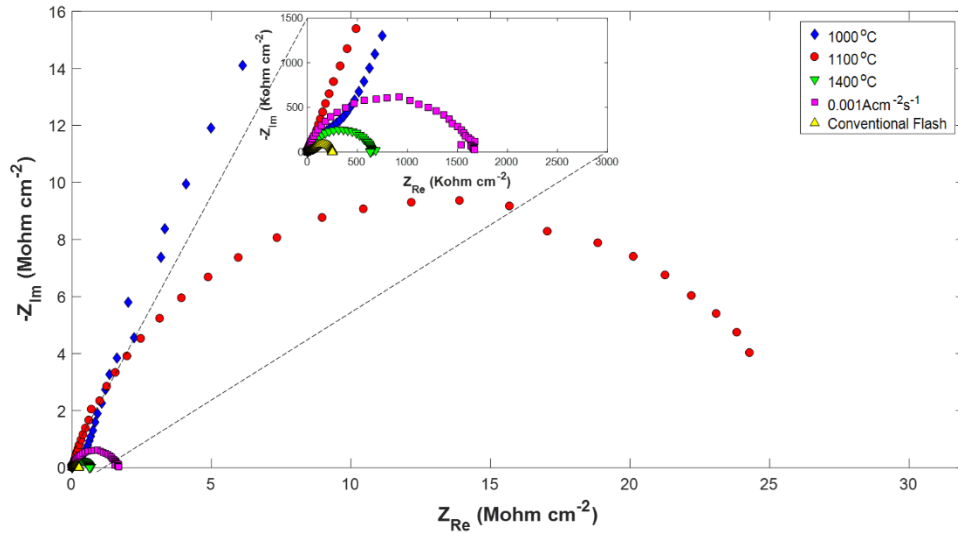
Figure 38: Nyquist plots of ZnO taken at 100 °C for conventional sintering at 1000 °C, 1100 °C, 1400 °C, compared with conventional flash sintering and slow current ramp flash sintering. Inset shows a zoom of the smallest impedance responses.

Impedance spectroscopy, given in Fig. 37, further indicates that bulk conductivity of specimens is higher when sintered at the slowest ramp rate of 0.001 A $\cdot$ cm^{-2} $\cdot$ s^{-1} due to the large average grain size, shown in Fig. 35. In addition, grain growth during the slowest ramp rate is comparable to conventional sintering at just over 1000 °C, shown in Table 4

and Fig. 38, which is consistent with predictions of flash sintering temperature in previous work (170).

Table 4: Comparison of conventionally sintered specimens, conventionally flash sintered specimen, and current ramp flash sintered specimen.

Furnace Temperature (°C)	Density (% Theoretical)	Average Grain Size (µm)	Current Density (A/cm^2)	Current Ramp Rate (A/cm^2/s)	Hole Time (s)
1000-CS	96	1.19 ± 0.044	0	N/A	60
1100-CS	97	1.83 ± 0.93	0	N/A	60
1400-CS	95	7.49 ± 2.85	0	N/A	60
700-FS	96	0.40 ± 0.16	5	Uncontrolled	60
700-CR1	90	0.22 ± 0.07	5	1	10
700-CR2	94	0.51 ± 0.24	5	0.1	10
700-CR3	96	0.50 ± 0.23	5	0.01	10
700-CR4	98	1.28 ± 0.67	5	0.001	10

This situation reverses with faster ramp rates. As the ramp rate increases from 0.01 $A·cm^{-2}·s^{-1}$ to 0.1 $A·cm^{-2} · s^{-1}$ to 1 $A·cm^{-2}·s^{-1}$ and, finally, to the fastest rate in conventional flash sintering. The grain size factor on its own does not explain this relation to conductivity. This becomes even more apparent when comparing flash sintering conductivities to conventional sintering conductivities, which are much lower.

Grain growth is also related to complexions, or grain boundary phases, which attain non-equilibrium structure as a result of rapid heating (194) and prevent atoms them from forming closely packed, orderly crystal structure near the boundaries (168). This has two consequences: enhanced diffusion along the grain boundaries, which causes sintering, and rapid movement of the grain boundaries, resulting in grain growth which leaves behind many defects such as stacking faults in its wake (209, 210). These stacking faults remain in the new, larger grains, and are now paths for electrons, similar to the 2d conduction

layers described by Luo (100), which increases the conductivity of the specimen. In this case, the faster the heating rate, the greater the concentration of stacking faults.

A rapidly rising current may induce more oxygen ions out of the lattice to compensate for insufficient available electrons. In this case, the oxygen travels from one end of the sample to the other and out to the environment. After the electric field is turned off, to maintain charge neutrality, zinc ions are reduced with weakly bonded electrons in the valence band, which lowers the activation energy required to promote them from the valence band to the conduction band. We do not claim that these point defects play any role in the sintering or initiation of flash, but are present as observed in the post sintered electrical conductivity, as was also confirmed by cathodoluminescence spectroscopy on flashed specimens of ZnO (97).

However, we cannot confirm any of these possibilities. The main goal of this work remains to provide a new method to tune the microstructure and electrical properties with a controlled current ramp while avoiding hot spot formation.

5. TiO₂ – Inhomogeneous Temperature Distribution, Reduction, and Microstructure

5.1 Inhomogeneous Reduction and its Relation to Grain Growth of Titania during Flash Sintering

5.1.1 Disclaimer

This work has been published in Scripta Materialia (176). The author constructed the experimental apparatus and performed the experiments with the help of Dr. Shikhar K. Jha. The principal investigator of this work is Dr. Thomas Tsakalakos. Part of the analysis was performed at Purdue University by Han Wang and Xin Li Phuah under the direction of Dr. Haiyan Wang. This work was funded by the Office of Naval Research under subaward Contract No. 4104-78982-820133 for Rutgers University and N00014-17-1-2087 for the flash sintering effort and N00014-16-1-2778 for the TEM work.

5.1.2 Introduction

Flash sintering (FS) utilizes an electric field, which is applied across a ceramic green body at high temperature and results in a non-linear rise in current through the sample, causing rapid densification. Flash sintering was first shown to reduce the required furnace temperature for sintering of 3 mol% yttria-stabilized zirconia (3YSZ) from 1450

°C for conventional sintering (CS) to 850 °C and additionally lowered the time to under 5 seconds (6).

Despite the work of many researchers there is still a great deal of debate as to the predominant mechanism responsible for the enhanced diffusion during the flash event. Three proposed mechanisms include rapid heating and the resulting destabilization of the grain boundaries (37, 99), an avalanche of Frenkel pair defects induced by the electric field which enhances the diffusion pre-exponential factor (6, 43, 155, 211), and local melting or softening of the grain boundaries due to inhomogeneous temperature distribution, which enhances diffusion across the grain boundaries (156, 158).

In ionic and mixed electronic-ionic conductors diffusion through vacancy and interstitial mechanisms takes place under the influence of a chemical potential, as in the operation of a solid oxide fuel. The observation of defects in the bulk during or post flash has been claimed as evidence that Frenkel pairs are generated and enhance the kinetics of sintering (43, 173). However, diffusion of oxygen vacancy-interstitial pairs alone does not lead to densification as diffusion of both the species are required.

For the case of titania, found in three polymorphs (rutile, anatase, and brooktite), rutile is the only stable phase at high temperatures and is a mixed conductor. Rutile and composites containing rutile is a common model system studied in flash sintering works (79, 80, 82-84, 86, 112).

Although in situ flash sintering of TiO_2 (84) as well as ZnO (97) and 3YSZ (173) give direct evidence of oxygen diffusion during flash sintering, detection of oxygen vacancies post-flash sintering has been elusive due to the relatively slow cooling of the

furnace which allows enough time for the non-equilibrium defects, namely interstitials and vacancies, to annihilate. In addition, the high surface area to volume ratio of a dogbone design allows for rapid re-oxidation. In contrast, experiments with thicker cylindrical pellets and rapid furnace cooling allow analysis of the reduction of titania, $TiO_2 \rightarrow xV_O^{\bullet\bullet} + TiO_{2-x}$. This reduction is clearly observed through blackening of the TiO$_2$ pellet interior unlike in previous studies of flash sintering of ZnO (170, 175), a related n-type semiconductor.

Inhomogeneity in the microstructure across the electrodes has been discussed in detail in a review by Yu, et al. (189). Other chemical inhomogeneity observations during flash sintering have been made. For example, blackening at the cathode of tricalcium phosphate (TCP) (126) was attributed to oxidation at the anode and reduction at the cathode. Also, a buildup of magnesium near the cathode in magnesia-silicate glass-containing alumina (47, 146) and sodium in soda lime silicate glass (148) was caused by migration of positively charged ions towards the cathode.

Raman spectroscopy and X-ray photoelectron spectroscopy (XPS) were used to study the chemistry and crystallinity across the FS specimen. These tools were used to map inhomogeneity in the reduction which had a greater concentration at the anode. Analysis of the microstructure indicated a distinct electrode effect in sintering, with more intergranular porosity and less grain growth at the cathode and intragranular porosity and rapid grain growth at the anode.

5.1.3 Experimental Methods

Rutile titania nanopowder, grain size ~50 nm, was acquired from Inframat Advanced Materials, Product # 22N-0814R. The powder was loaded into a 6mm die with uniaxial, 200MPa applied pressure, which achieved a green body density of ~52%.

For FS, samples were coated with platinum paste on both faces and placed inside a cylindrical, alumina stage with platinum electrodes in contact at both ends. The specimens were then heated at a rate of 10 °C·min^{-1} under 50 V·cm^{-1} DC electric field applied at 500 °C. The alumina stage was placed inside an alumina tube enclosure within the furnace, which created a less oxygen-rich environment than air, which initiated the runaway effect of flash with a significantly lower electric field than mentioned in the literature (79).

As the sample was heated it became more conductive, which allowed a small current flow. The internal resistance to the current heated the sample and allowed even more current to flow. The external, conductive heating due to the ramp of the furnace and the internal, resistive heating of the sample due to current flow created a feedback loop that resulted in a rise in current and rapid densification. To avoid runaway heating a limit was placed on the current, in this case 5 A·cm^{-2}, and the electric field dropped accordingly. This stage was held for 1 minute before the electric field was turned off altogether and the furnace was cooled at a rate of 25 °C · min^{-1}.

A comparison was made using a CS specimen at 1150 °C with heating rate of 10 °C·min^{-1}, 1 min hold time, and cooling rate of 25 °C·min^{-1}. Both specimens were cut vertically to expose the cross-section area from cathode to anode and were mechanically polished down to 0.25 μm using diamond polishing paste.

The specimen crystallinity was analyzed using Renishaw InVia Raman MicroSpectroscopy with spot size ~1 μm and Raman shift range 100-700 cm^{-1}. Three spots were mapped: the cathode and anode for the FS sample, and middle for the CS standard. The specimen chemistry was analyzed using ThermoFisher K-Alpha X-Ray Photoelectron Spectroscopy (XPS) with 1486.7 keV x-ray photon energy and 400μm spot size. Three spots were mapped at different sections of the cross-section area: cathode, middle, and anode. After completion of a survey scan over a binding energy range from 1350 eV – 0 eV with 1 eV step size, the specific regions 298 eV – 279 eV (C1s), 475 eV – 448 eV (Ti2p), and 545 eV – 525 eV (O1s) were scanned in detail (see Fig. 40) for each position.

(e)	Cathode (eV)	Middle (eV)	Anode (eV)
O1s metal oxide	530.22	530.14	530.12
O1s metal carbonate	531.73	531.77	531.78
Ti2p3/2	458.88	458.78	458.71
Ti2p1/2	464.57	464.49	464.44
Ti2p satellite	471.94	471.81	471.79
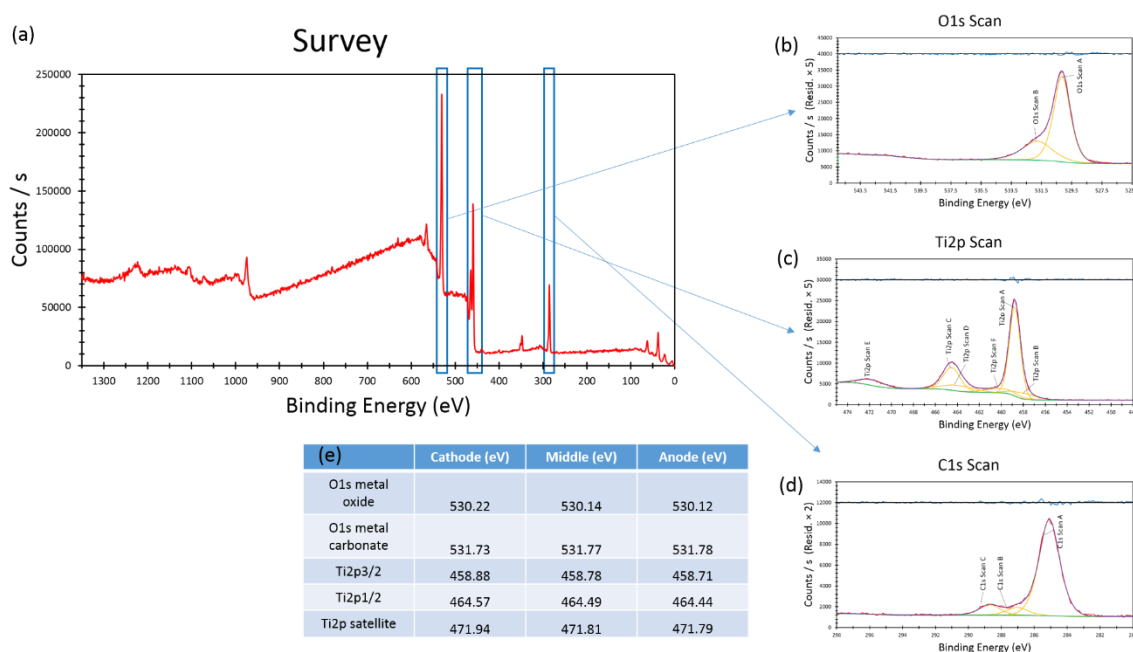
Figure 39: XPS survey plot (a) and detailed fitting for binding energies for (b) O1s, (c) Ti2p, and (d) C1s core level excitations. (e) The binding energies for selected O1s and Ti2p peaks have been estimated for cathode, middle, and anode.

After completion of analysis with Raman Spectroscopy and XPS, the samples were both thermally etched at 900 °C for 1 h to reveal the grain boundaries for the SEM micrographs. The samples were coated with 10 nm of gold and a Zeiss Sigma Field Emission SEM with 5 kV electron gun was used to characterize the microstructures. Separately, a FS specimen under the same conditions was prepared for imaging under transmission electron microscopy (TEM). The sample was sectioned to create plan-view samples of the cathode, middle and anode. Each section was ground, polished and dimpled, followed by final polishing done using a precision ion milling machine, PIPS II, Gatan. Microstructural characterization was completed by the FEI TALOS F200X TEM operated at 200 kV.

5.1.4 Results

The three stages of flash sintering (212) were shown in Fig. 41. In stage I, the sample temperature rose high enough for necking to occur between grains. The necking created conduction paths for a small current, which resulted in modest dimensional shrinkage. As a constant voltage was applied to the shrinking sample, the apparent electric field increased and, combined with increased conductivity due to densification and heating, an exponential rise in current necessitated a current limit to avoid thermal runaway. This stage is where most of the densification occurred along with pore closure (80). In the final stage of flash sintering the electric field gradually declined to a steady state to maintain constant current. Final densification and grain growth were characteristic of this stage. With significant grain growth pore breakaway occurred, resulting in round intragranular pores (213).
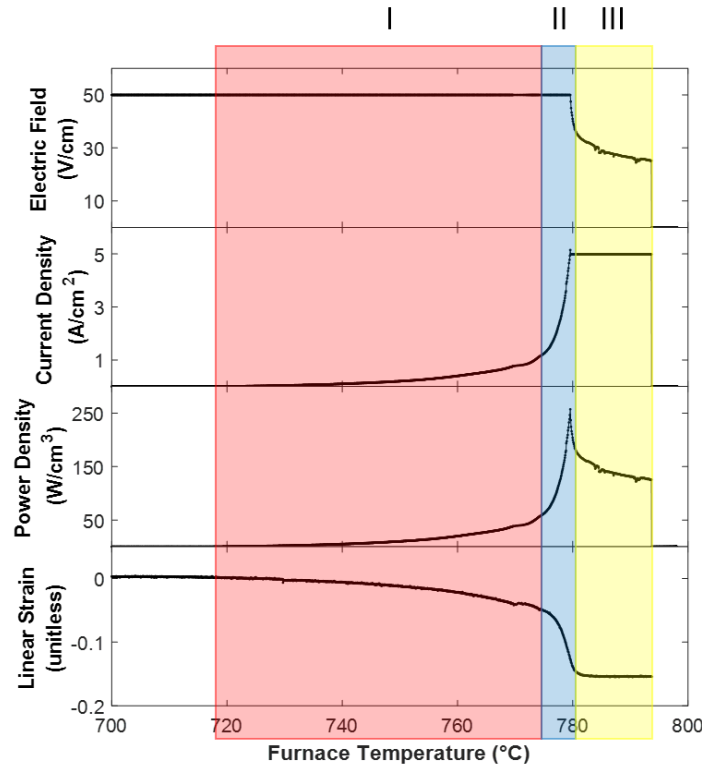
Figure 40: An electric field is applied as TiO_2 is heated, resulting in a nonlinear rise in current, which is limited to a maximum value of $5A/cm^2$ by limiting the applied electric field. The resulting power density (P=EJ) causes rapid densification, represented by linear strain. The three stages of flash (I, II, and III) are labelled. While most of the densification occurs in stage II, grain growth continues in stage III.

The microstructure, indicated in Figure 42, showed three distinct regions. At the cathode, Figure 42(a) and (d), pore closure was incomplete and grain growth was limited (0.41 ± 0.15 μm). In the middle region, Figure 42(b) and (e), most pores had been eliminated and gradual grain growth (0.90 ± 0.43 μm) occurred, indicated by limited intragranular porosity. Large grains (1.34 ± 0.66 μm), intragranular porosity, and regions of abnormal grain growth were evident at the anode, Figure 42(c) and (f). A summary of these results and comparison to conventional sintering is given in Fig. 43.
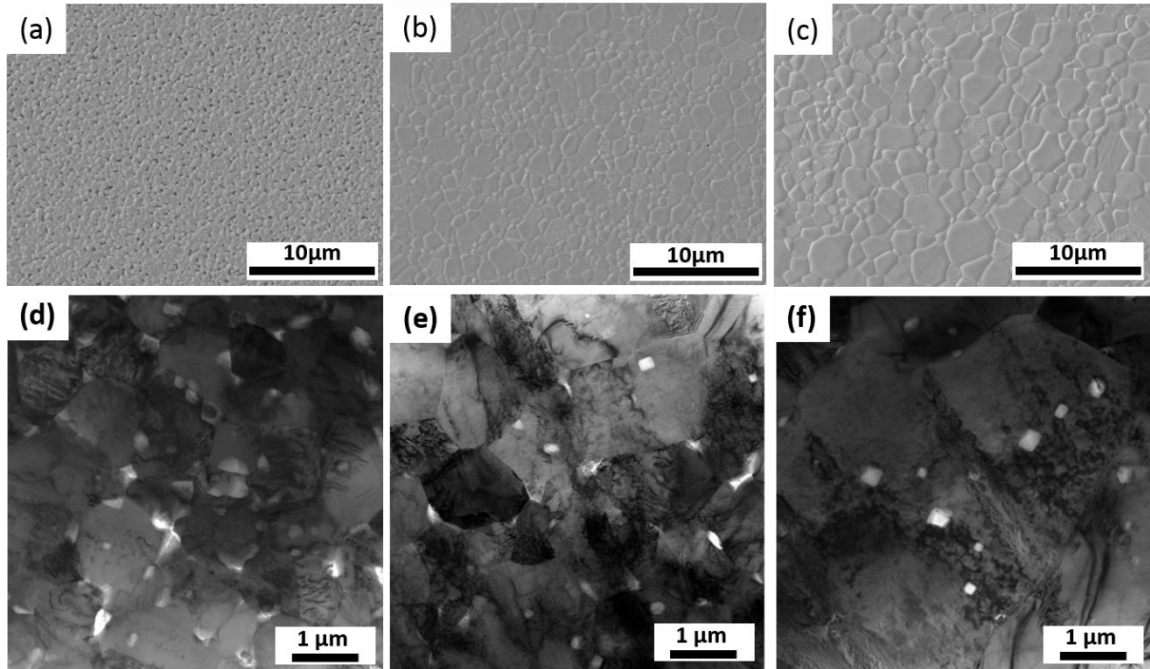
Figure 41: Significant electrode effect revealed in microstructure for flash sintering at the (a) cathode, (b) middle, and (c) anode. TEM microstructure reveals high intergranular porosity at the cathode (d) with limited grain growth compared with rapid, abnormal grain growth at the anode (f) and high intragranular porosity, which is not found in SEM due to filling of intragranular pores during polishing and thermal etching. The middle region (e) has characteristics of both anode and cathode. TEM images are shown, with permission, by Dr. Haiyan Wang's group at Purdue University.
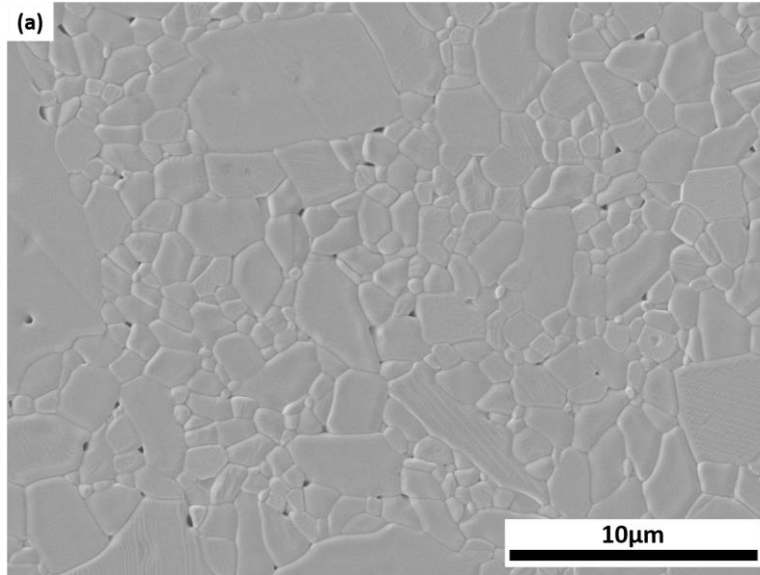
(b)	Mean grain size (μm)	Standard Deviation (μm)	Apparent Porosity (SEM) (%)
CS	1.352	1.033	1%
FS-Cathode	0.405	0.148	6-7%
FS-Middle	0.896	0.434	<1%
FS-Anode	1.343	0.656	<1%

Figure 42: (a) Microstructure of rutile TiO_2 sintered by heating conventionally to 1150°C. (b) Comparison of mean grain size for CS and for the three regions of FS has been included.

A cross section of the profile of the pellet is shown in Figure 44(a) with cathode, middle, and anode corresponding to white, grey, and dark grey coloration. Three fundamental Raman vibration modes were identified for rutile: B_{1g} = 144 cm^{-1} O-Ti-O bending mode, E_g = 448 cm^{-1} O c-axis liberation mode, and A_{1g} = 612 cm^{-1} Ti-O stretch mode (214-216). Comparison of the cathode, anode, and CS reference indicated no visible Raman peak shift for the three identified fundamental Raman modes, Figure 44(b). However, Raman peak reduction and broadening (Figure 44(c)), especially at the anode, indicated a decrease in crystallinity (217-219) which is counterintuitive considering the increase in grain size and corresponding reduction in the number of grain boundaries.

XPS analysis of three positions corresponding to measurements from cathode to middle to anode indicated a downshift of the binding energies for the $Ti2p_{3/2}$ (458.9 eV to 458.7 eV), $Ti2p_{1/2}$ (464.6 eV to 464.4 eV), and O1s metal oxide bonds (530.2 eV to 530.1 eV), shown in Figure 44(d) and (e). XPS downshift, corresponding to reduction of a portion of Ti^{4+} ions to Ti^{3+}, indicated an increase of $V_O^{\bullet\bullet}$ defects (220, 221).
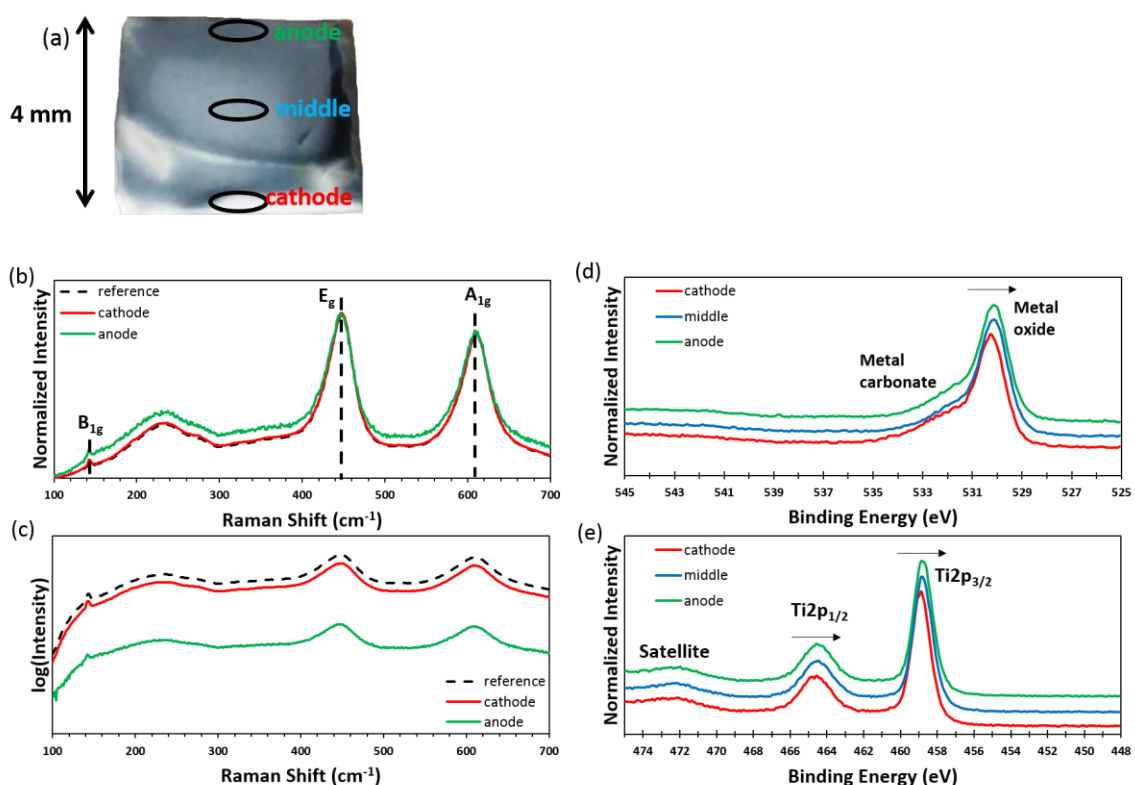
Figure 43: (a) Cross section of the sintered pellet with different levels of blackening. Normalized Raman Spectroscopy (b) indicates no shift of the Raman vibrational modes despite change in stoichiometry. Decrease in intensity (c) is caused by reduced crystallinity. Normalized XPS intensity, with background removed, are shown for (d) O1s peaks and (e) Ti2p peaks.

5.1.5 Discussion

Three possible explanations are provided for the gradient of oxygen vacancies corresponding with enhanced sintering and grain growth:

1) Oxygen depletion changes the stoichiometry of TiO_2 at the grain boundaries resulting in enhanced sintering and grain growth. However, oxygen vacancies move towards the negative electrode as they are positively charged so the direction of the reduction and grain growth should be opposite to that observed.

2) The electric field causes vacancy-interstitial pair formation (Frenkel pairs) that under sintering pressure diffuse to the grain boundaries and pores, respectively, resulting in enhanced diffusion kinetics (43, 211). The titanium cations are relatively less mobile and remain in the structure while some oxygen anions are released into the environment (84). The question remains as to why there would be a microstructure gradient.

3) A temperature gradient from cathode to anode enhances grain growth. This can be caused by a Peltier effect, also seen in SPS with the same orientation (2, 3). The resulting grain growth increases ion mobility by decreasing the number of grain boundaries and corresponding space charge layers which act as oxygen vacancy traps (222).

In situ energy dispersive X-ray diffraction (EDXRD) during FS of TiO_2 shows that there was an inhomogeneous lattice expansion across the length of the specimen, parallel to the electric field (169). The lattice expansion was largest near the anode and smallest at

the cathode. As the ionic bonds in ceramics expand in length during heating, this lattice expansion is an indication of differential heating.

To explain this temperature gradient we hypothesize a Peltier effect, which occurs due to the temperature gradient formed by current flow across two different conductors (or semiconductors) (223),

$$\dot{Q} = (\Pi_A - \Pi_B)I \sim (S_A - S_B) \,, \tag{5.1.1}$$

where $\dot{Q}$ is the heat generated (or expended) per unit time, Π is the material dependent Peltier coefficient, and I is the current flowing through the circuit.

More commonly known from studies of thermoelectric materials, the Seebeck coefficient related to the Peltier coefficient by the Thomson relation, $S = \frac{\Pi}{T}$. Thus,

$$\dot{Q} \sim (S_A - S_B) \,, \tag{5.1.2}$$

Seebeck coefficients for metals are typically orders of magnitude lower than those for semiconductors (224). Thus, we can approximate $\dot{Q} \sim -S_{TiO_2}$ for anode and $\dot{Q} \sim +S_{TiO_2}$ for cathode. As the Seebeck coefficient for TiO_2 is negative (225) we find qualitatively that there will be heating of the anode and cooling of the cathode.

In n-type semiconductors, such as TiO_2 and ZnO, the predominant charge carriers are electrons and, in agreement with predictions by Yu, et al. (189) this causes heating near the positive electrode (anode) and cooling near the negative electrode (cathode), which causes charge. Abnormal grain growth at the anode side of ZnO pellets sintered under flash conditions has also been observed independently by two groups (99, 175).

5.1.6 Summary

In summary, the findings demonstrate a reduction of TiO_2 due to the directional conduction of oxygen ions under the applied DC electric field as determined by Raman and X-Ray Photoelectron Spectroscopy. The microstructural gradient across the sample thickness from anode to cathode is explained by differential heating due to the Peltier effect, which causes heating at the anode and cooling at the cathode. This abnormal grain growth at the anode depletes the number of grain boundaries, which act as oxygen vacancy traps, and cause further non-stoichiometry (blackening) at the anode.

5.2 In situ Measurement of Temperature and Reduction of Rutile Titania using Energy Dispersive X-ray Diffraction

5.2.1 Disclaimer

This work has been submitted to the Journal of the European Ceramic Society (169). The author constructed the experimental apparatus and performed the experiments with the help of Dr. Shikhar K. Jha. The principal investigator of this work is Dr. Thomas Tsakalakos. Part of the analysis was performed at Purdue University by Han Wang and Xin Li Phuah under the direction of Dr. Haiyan Wang. This work was funded by the Office of Naval Research under subaward Contract No. 4104-78982-820133 for Rutgers University and N00014-17-1-2087 for the flash sintering effort and N00014-16-1-2778 for the TEM work. The other part was performed with the help of Dr. John Okasinski at

5.2.2 Introduction

Flash Sintering is a new technique first developed by Cologna, et al. to sinter 3mol% yttria stabilized zirconia at 850 °C in seconds (6). Since the development of this technique many oxides have been successfully sintered including 3YSZ (17, 18, 212), ZnO (94, 95), TiO_2 (79, 83), Y_2O_3 (102), SnO_2 (90), 8YSZ (49, 50, 53), Al_2O_3 (43), CeO_2 (67-69), $SrTiO_3$ (70, 72), $BaTiO_3$ (87), Co_2MnO_4 (66), KNN (106), HA (108), LSGM (114), $MgAl_2O_4$ (113), $BiFeO_3$ (117, 118), ZrO_2 (93, 119), and UO_2 (122).

In non-isothermal flash sintering experiments the furnace temperature ramps up at a fixed rate with an electric field is applied across the two ends of the ceramic green compact. The three stages of flash sintering of titania have been explained in another work (176). In brief, the temperature of the specimen rises in Stage I, allowing a small, linear rise in current due to higher electrical conductivity. After a short incubation time, which is determined by the material composition, applied electric field, and furnace temperature, the current density begins to rise and causes noticeable Joule heating, which marks the start of Stage II. There will be an increase in current density with rising electrical conductivity, which in turn induces more current to pass through with the same applied voltage. The feedback loop will limit the current at a fixed value, leading to runaway Joule heating and consequently an increase in the specimen temperature. The power supply switches into current control at the current limit and the electric field drops in response to increasing conductivity. Once the material reaches its highest conductivity, the electrical field reaches the steady state of Stage III.

In isothermal flash sintering experiments, where the furnace temperature is held at a given temperature, the incubation time of Stage I can be skipped altogether by applying a sufficient electric field to cause a nonlinear rise in conductivity and feedback loop. In this case, the current density is still limited at a user defined current limit, initiating Stage III, but the furnace temperature remains fixed and the electric field can reach steady state more rapidly. Isothermal flash experiments are more suitable when attempting to study properties in situ by eliminating an additional variable.

The mechanism(s) responsible for rapid densification in flash sintering remain highly debated, Proposed mechanisms include Joule heating above the conventional sintering temperature (16, 56, 62, 94), rapid heating which destabilizes the grain boundaries (37, 99, 100, 175), the generation of defects as a result of the applied electric field (29, 43, 155, 211), pore migration caused by surface cation diffusion (50, 55), and local melting or softening at the grain boundaries which induces liquid phase sintering (156, 158). Two in particular, defect generation and Joule heating, make predictions about specimen temperature below (155) and above (62) conventional sintering temperatures, respectively. However, studies of flash sintering in ZnO (170, 175) have shown that the flash sintering temperature approaches the conventional sintering temperature.

Rutile TiO_2 is a model system for flash sintering studies (79, 80, 82-84, 86) due to its stable crystal structure. It is an n-type semiconductor, similarly to ZnO, which likely undergoes a similar densification mechanism during flash sintering.

Energy Dispersive X-Ray Diffraction (EDXRD) is a unique tool that uses a stationary detector to measure a complete x-ray diffraction pattern in real time. EDXRD is a special case where there is no monochromator, i.e. the full spectrum of white light x-ray

radiation is utilized such that a particular x-ray photon energy is analogous to a 2θ angle. Thus, the detector can be placed in a stationary position and the same spectrum is measured throughout the experiment. In addition, utilizing the high intensity X-ray source at the synchrotron facility at Argonne National Laboratory (ANL) Advanced Photon Source (APS) gives data at a high acquisition rate so the flash event and changes in crystal structure can be tracked in situ.

Another advantage of EDXRD is that it allows the user to select a diffraction volume within the sample and collect data only within the volume with size determined by the cross sectional area of the beam and the relative position and orientation of the detector with the incident radiation. The outer surface of the sample within the beam path is not collected unless desired and, thus, the data collected is the bulk data unlike the case of a pyrometer, which only collects surface data.

Using this tool, the temperature can be approximated by comparing the lattice expansion of the specimen to the lattice expansion of a conventionally heated standard. In addition, if the lattice goes through significant reduction, the lattice parameter of some unit cells changes in response to the change in bond length caused by reduction of metal cations.

Another means of calculating the specimen temperature, which assumes that the emission of energy in the form of radiation matches the additional thermal energy absorbed by the specimen due to Joule heating is known as the blackbody radiation model (62, 95, 118, 155) such that

$$I_o + I = \sigma T^4, \tag{5.2.1}$$

where $I_o = \sigma T_o^4$ is the blackbody radiation generated by the sample in the furnace before flash, I is the additional power (W) per unit surface area (A) expended due to the resistance of the sample, σ is the Stefan-Boltzmann constant (5.67 x 10^{-12} W·cm^{-2}·K^{-4}), and T is the sample temperature (K).

This is a straightforward model which gives a simple expression for the specimen temperature (155),

$$T = [T_o{}^4 + \frac{W}{A\sigma}]^{1/4} \ . \tag{5.2.2}$$

However, this model omits the fact that ceramics are not perfect blackbodies. In addition, while dogbone specimens have limited thermal conduction as the only connection to the dogbone are two thin platinum wires, pellets are generally sandwiched between electrodes in a stage with bottom base and top pushrod. Incorporating these factors gives a greybody radiation model with thermal conduction for the average specimen temperature,

$$I_o + I = \epsilon\sigma T^4 + k\frac{\Delta T}{L}, \tag{5.2.3}$$

where $I_o = \epsilon\sigma T_o^4$, ϵ is the material emissivity, generally ~ 0.9 for oxides (37, 79), k is the material dependent thermal conductivity (W·cm^{-1}·K^{-1}), $\Delta T = T - T_o$ is the difference in temperature between sample and furnace, and L is the pellet thickness. Derivation of this model is given in Appendix B.

In addition, for n and p-type semiconductors, there is a significant Peltier effect caused by the flow of charge carriers that creates an inhomogeneous temperature distribution through the length of the pellet,

$$T(x) = -\frac{a}{6k}x^3 - \frac{b}{2k}x^2 + \left(\frac{T_2 - T_1}{L} + \left(\frac{aL}{3} + b\right)\frac{L}{2k}\right)x + T_1 , \tag{5.2.4}$$

where a and b are fitting constants for the power density per unit volume at a position, x along the thickness of the specimen, T_2 is the temperature at x=L, and T_1 is the temperature at x=0. This function suggests the temperature has a cubic trend with maximum near the anode for n-type semiconductors $(T_2 - T_1 > 0)$ and near the cathode for p-type semiconductors $(T_2 - T_1 < 0)$.

Furthermore, microstructural characterization can be used to compare conventional sintering (CS) to flash sintering (FS) to help determine whether the sintering has a different character and what can be determined about the predominant mechanism responsible for the diffusion kinetics of TiO_2 during flash sintering.

5.2.3 Experimental Methods

Powder Processing, Conventional Heating, and Flash Sintering

Titania nanopowder (~50nm) from Inframat Advanced Materials, Product #22N-0814R was pressed in a 6mm die with 200MPa uniaxial force. Green bodies with 4mm thickness, 6mm diameter, and 52-53% density were heated overnight in a drying oven at 130 °C to remove excess moisture on the surface of the grains.

During the CS experiment the pellet was heated at a rate of 10 °C $\cdot$ min^{-1} from room temperature to 1200 °C. For the FS experiments the sample was heated to 850 °C at a rate of 10 °C$\cdot$min^{-1} and held for 5 minutes to stabilize the temperature before the electric field was applied. This temperature is too low for significant sintering to occur.

Three FS experiments were run in succession with a five minute gap between runs to allow the specimen to cool to furnace temperature. An electric field of 200 V $\cdot$ cm^{-1} was applied, higher than needed based on the literature (150 V$\cdot$cm^{-1}) (79), to allow the sample

to rapidly go into current control. Three FS experiments were run in succession with three different current density limits: 1 A·cm^{-2}, 3 A·cm^{-2}, and 5 A·cm^{-2}. The specimen predominantly densifies to >90% of theoretical density during the first run and mostly undergoes grain growth during the second and third runs. At the end of the experiment the furnace was turned off and the furnace cooled to room temperature.

The samples prepared for SEM analysis were run separately in the laboratory. The CS samples were prepared by heating at a rate of 10 °C·min^{-1} to 1000 °C, 1050 °C, 1100 °C, and 1150 °C, holding for 1 minute, and cooling at a rate of 10 °C·min^{-1} to room temperature. The FS samples were separately heated to 850 °C at a rate of 10 °C·min^{-1}, held for 5 minutes, and then 200 V·cm^{-1} was applied with a preset current density limit, 1 A·cm^{-2}, 3 A·cm^{-2}, and 5 A·cm^{-2}, with three-minute hold time in current control to match the synchrotron conditions, after which the electric field was turned off and the samples were cooled at a rate of 10 °C·min^{-1}.

Energy Dispersive X-Ray Diffraction

The detector was placed at an angle, in this case $2\theta \sim 3°$, measuring one portion of the diffraction ring. For nanometer and submicron sized particles the gauge volume contains enough grains with random orientations so texturing did not affect the intensity of the collected beam. However, as grain size increased to microns or tens of microns the orientation of the large grains affected the counts collected at that particular site on the diffraction ring. The slits were limited to 2 mm x 0.2 mm to balance intensity requirements, for which a larger beam size increases intensity, to the constraints of the furnace such that the gauge volume was small enough to avoid collecting data from the surrounding stage.

For conventional heating counts were collected over a 60 second period, roughly coinciding to 1 scan / 10 °C. Since conventional sintering is a slow process 60 seconds was still a fast enough acquisition rate to track the sample properties. For the profile scans collected over the specimen length, from positive to negative electrode, a 1 second acquisition time was taken per position with a 5 second delay to change the sample position using the automated xyz stage. Each scan covered a full, 0.2 mm section of the sample and the stage was shifted by 0.2 mm vertical steps for the remaining scans.

X-rays were collected in a germanium detector at different penetration depths, or channels, such that channel number is proportional to the frequency of the x-ray. These frequencies, corresponding to energies, are reciprocal to the d-spacing in real space and calibration standards were used to convert the data from channel to energy to d-spacing. Using 8YSZ and CeO2 as calibration standards yielded the following fitting constants (see Appendix A, Equations (5.2.7.2) and (5.2.7.3)): $A = 0.1840$ keV, $B = 0.0349$ keV, and $2\theta = 3.004°$. The spectra were fitted using a purpose built MATLAB fitting program approximating the peaks to a Pseudo-Voigt shape.

This process is summarized schematically in Fig. 45 and 46 and has been used in other publications (52, 112, 170, 171). The results, including fitting of the a and c lattice parameters versus temperature during conventional heating, are given in Fig. 47. The electric field, current density, and power density for each experiment are shown in Fig. 48(a) while the response of the a and c lattice parameters during FS are shown in Fig. 48(b) and (c).
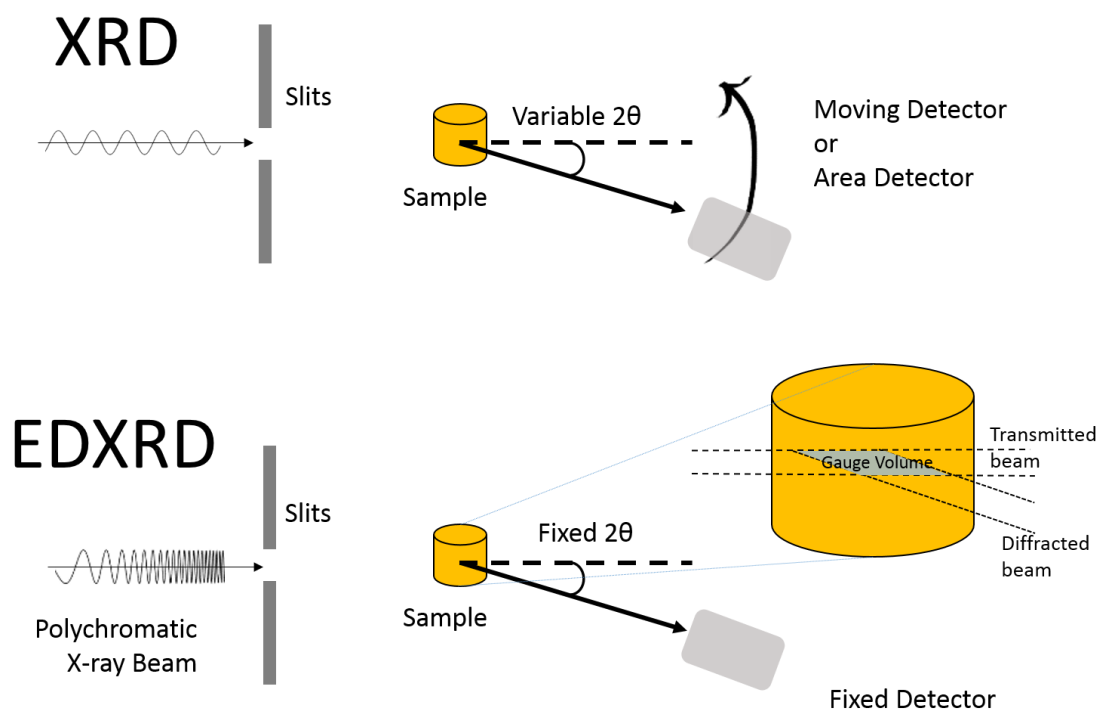
Figure 44: Schematic summary of energy dispersive x-ray diffraction (EDXRD) contrasted with traditional, monochromatic x-ray diffraction (XRD).
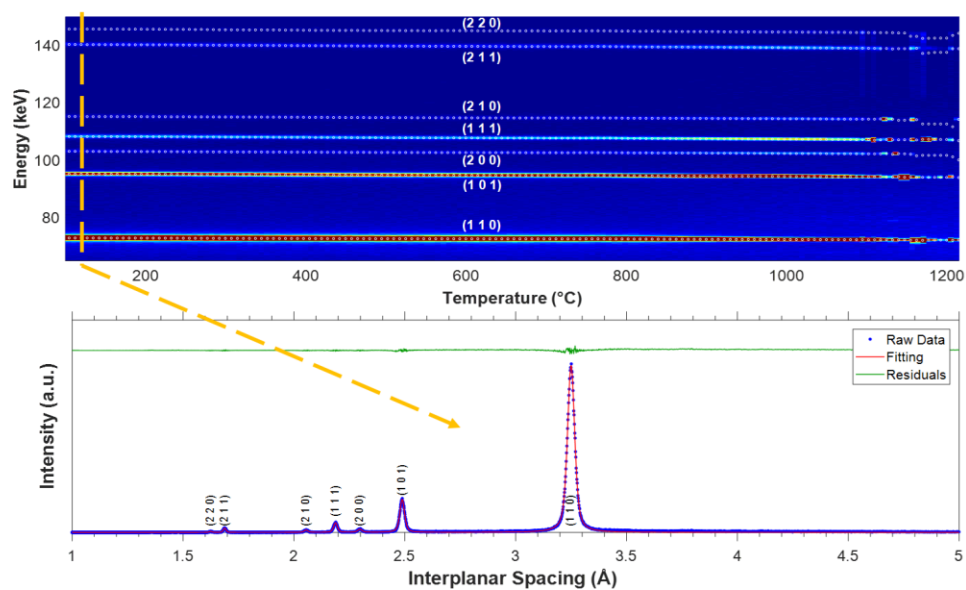
Figure 45: The fitting process of the EDXRD spectra involves the conversion of channel number to energy in reciprocal space to d-spacing. The spectra are then fit with a Pseudo-Voigt function. The contour plot is taken for conventional heating of TiO2 to 1200 °C.
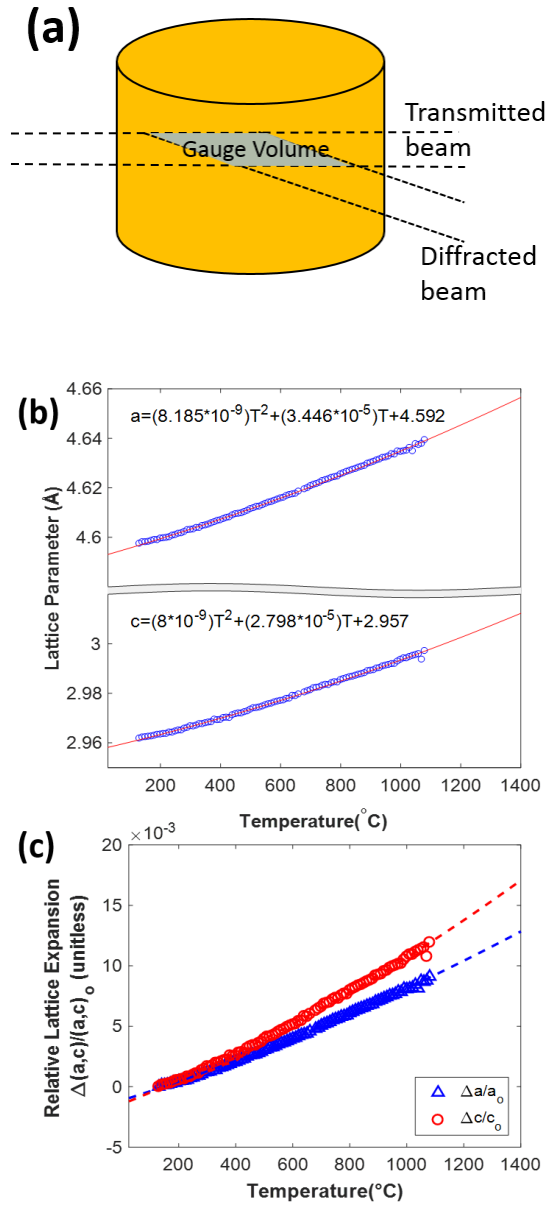
Figure 46: Using a gauge volume defined by collimating beam slits (a), a bulk section of the specimen has its Miller indices tracked allowing for calculation of lattice parameters (b), a and c, as well as the relative lattice expansions (c), $\Delta a/a_o$ and $\Delta c/c_o$, during conventional heating of rutile TiO_2.

Microstructural Characterization

Fracture surfaces were prepared for each of the four CS and three FS samples. SEM analysis of the anode, middle, and cathode were performed for the FS specimens due to the

microstructural variation throughout the sample. TEM analysis was also performed for the anode side of the 5 A·cm^{-2} FS specimen. The plan-view TEM sample was prepared through the conventional approach which includes manual grinding, polishing, dimpling and final polishing in an ion milling system (PIPS II, Gatan). FEI TALOS TEM operated at 200 kV was used in this study for microstructure characterization.

5.2.4 Results

Energy Dispersive X-Ray Diffraction – Peltier Effect, Reduction, and Temperature Approximation Methods

The majority of the sintering occurred at a current density as low as 1 A/cm^2 as shown in Fig. 52. Initial sample size of 4 mm decreased to 3.4 mm due to densification. The next two experiments further increased the density to >95% although this small change in thickness did not change the number of profile steps.

At J = 1 A·cm^{-2} two effects were apparent (Fig. 48 (b) and (c)): an asymmetric expansion of the lattice towards the anode, near the positive electrode, compared with the cathode, near the negative electrode, and a contraction of the lattice at the two ends in contact with the electrodes. The asymmetric lattice expansion suggests an asymmetric temperature distribution, which agrees with results from another study (176) where this effect was attributed to a continuous Peltier effect in agreement with predictions from a review by Yu, et al. (226). The lattice contraction at the ends suggests cooling due to thermal conduction.
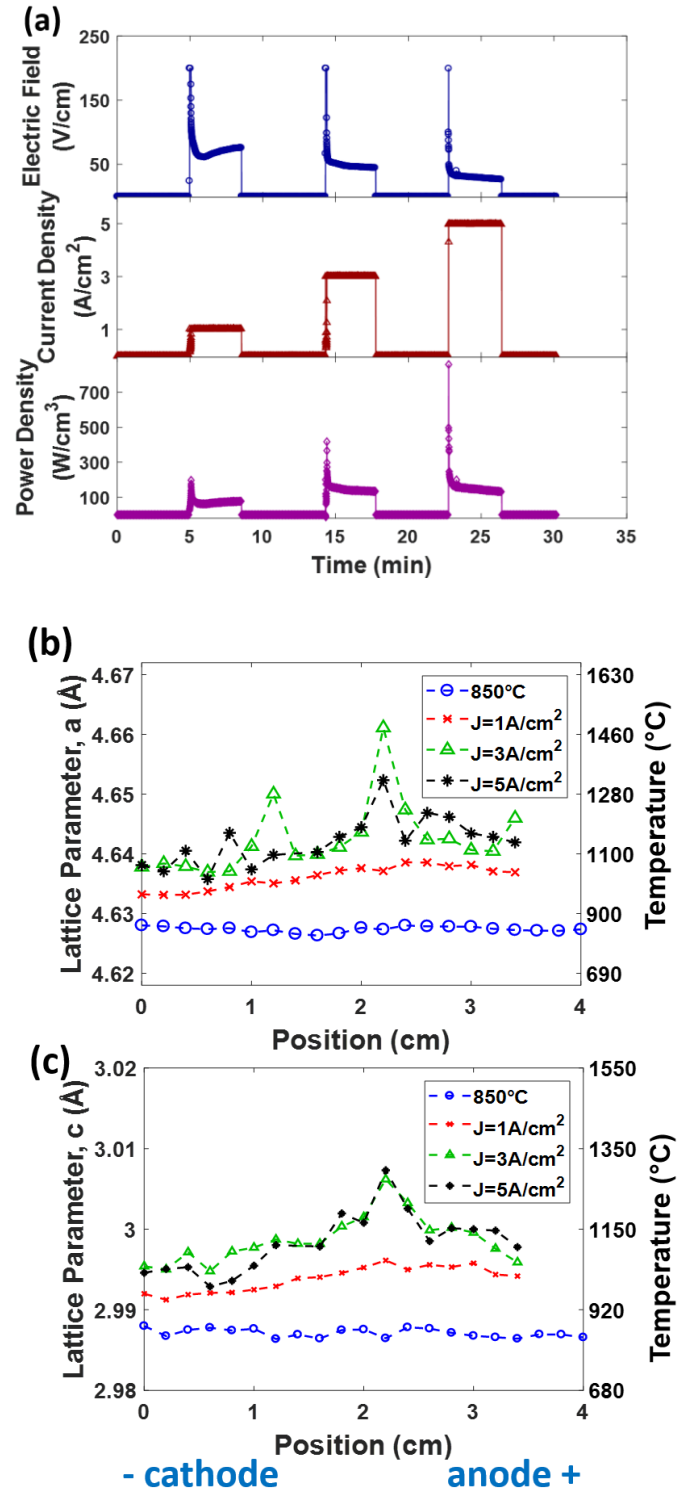
Figure 47: (a) Electric field, current density, and power density during 3 current limit regimes: 1 A·cm⁻², 3 A·cm⁻², and 5 A·cm⁻². Comparison of (b) lattice parameter, a, (c) and lattice parameter, c, before flash at T = 850 °C and at steady state J = 1 A·cm⁻², 3 A·cm⁻², and 5 A·cm⁻².

For J = 3 A·cm^{-2} the lattice expansion increased compared with 1 A·cm^{-2}. However, for J = 5 A·cm^{-2} only a small lattice expansion was observed compared with 3 A·cm^{-2}. Furthermore, the electric field in the steady state at 5 A·cm^{-2} was actually lower than the electric field at 3 A·cm^{-2} (Fig. 48(a)), which resulted in slightly higher power density. Since the conductivity of ceramics generally increases with temperature, this effect mitigated most of the Joule heating.

As indicated in Fig. 49, for higher current densities some positions displayed a peak shoulder formation which distorted the peak shape and created the appearance of a much larger heating effect. The shoulders were treated as secondary peaks of lower intensity which indicated longer bond lengths for a fraction of the unit cells. This effect can be attributed to the expansion of the ionic radius of Ti^{3+} (0.67A) in comparison to Ti^{4+} (0.605A), which resulted in lattice expansion of some of the unit cells during the transient period of flash (227).
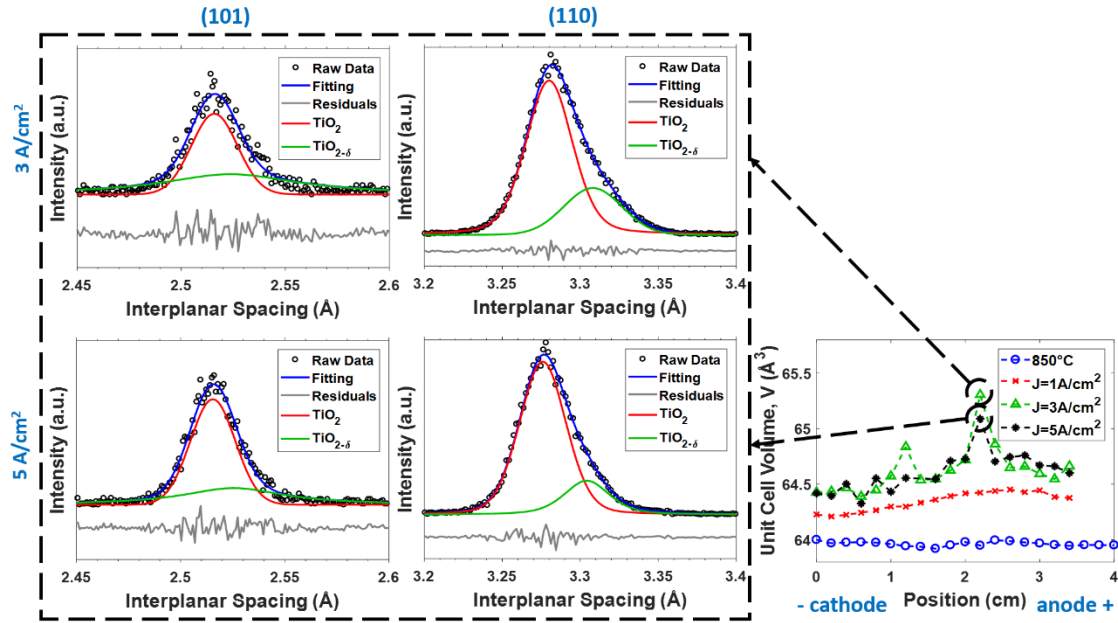
Figure 48: Shoulder formation occurs due to second peak formation. Fitted peaks modeled as a Pseudo-Voigt (Gaussian + Lorentzian) shape. The larger ionic radius of Ti^{3+} compared with Ti^{4+} causes a lattice expansion in the positions where oxygen vacancies have formed.

Using the calibration based on lattice expansion in conventional heating the temperature during steady state flash sintering was estimated experimentally (Fig. 50 and Table 5). The results showed that the blackbody radiation model overestimated the temperature beyond the maximum limit. Using a greybody radiation model, where the emissivity is approximated to ~ 0.9, the difference became even more evident.
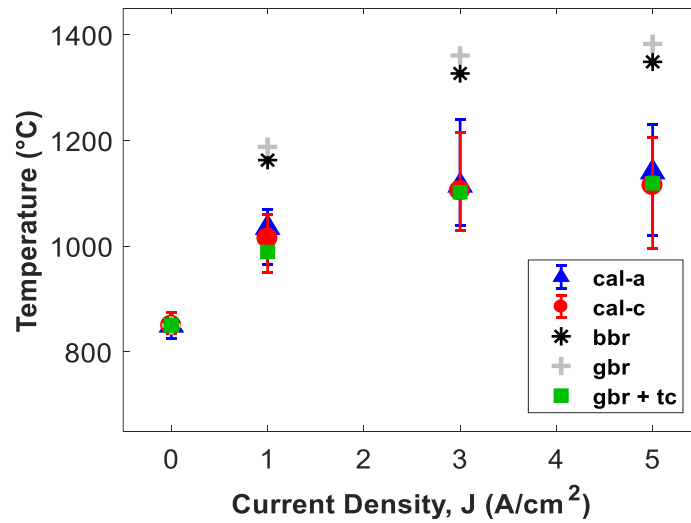
Figure 49: Temperature approximation at the middle of the specimen using calibration of lattice parameters a (cal-a) and c (cal-c) compared with black body radiation model (bbr), greybody radiation model (gbr), and greybody radiation model + thermal conduction (gbr+tc).

Table 5: Lattice parameters, a and c, and temperatures approximated using lattice calibration and blackbody radiation model.

	a		c		blackbody	greybody	greybody+ conduction
	Å	T (°C)	Å	T (°C)	T (°C)	T (°C)	T (°C)
850°C	4.6274	850	2.9870	850	850	850	850
Flash 1A	4.6367	1040	2.9941	1010	1163	1188	1001
Flash 3A	4.6409	1120	2.9982	1105	1327	1361	1124
Flash 5A	4.6421	1140	2.9984	1110	1349	1383	1143

Incorporating thermal conduction is somewhat more complicated. Thermal conductivity increases with density due to increased grain-grain contacts at higher density, but the thermal conductivity was approximated to $k = 0.033472 \, W \cdot cm^{-1} \cdot K^{-1}$ from the

literature (162) with 0% porosity rutile TiO_2 from 600 °C - 1200 °C. The difference in thermal conductivity at 90%+ compared with 100% is assumed to be small.

In addition, as the temperature of the specimen increased during flash the temperature of the electrodes in contact with the specimen increased as a result of thermal conduction. Thus, the value of T_o at the interfaces is power density dependent. A rough approximation was made by scaling the increase in interface temperature by ~5 times the power density through the specimen. This is by no means an exhaustive approach and steps can be taken to approximate the interface temperatures experimentally. Calculating the flash temperatures using Eq. (5.2.3) gave more reasonable values compared with consideration of radiation alone (Fig. 50).

Microstructure Analysis

The microstructure at the cathode and anode (Fig. 51) confirms that the temperature was lower at the ends during flash, which is expected considering thermal conduction from the sample to the electrodes. The anode for all three conditions is composed of larger grains than the cathode, confirming a Peltier effect with thermal conduction at the two ends is the largest factor in grain growth during flash and a temperature profile is qualitatively shown in Fig. 52 fitting to the lattice expansion. TEM analysis (Fig. 53) of the microstructure at the anode with $J = 5$ A·cm^{-2} indicates that abnormal grain growth occurred, with abnormal grain boundary migration potentially forming stacking faults and trapping many intragranular pores. Furthermore, bimodal grain size distribution, marked by red dashed lines, is evident in the microstructure with large grains adjacent to small grains.
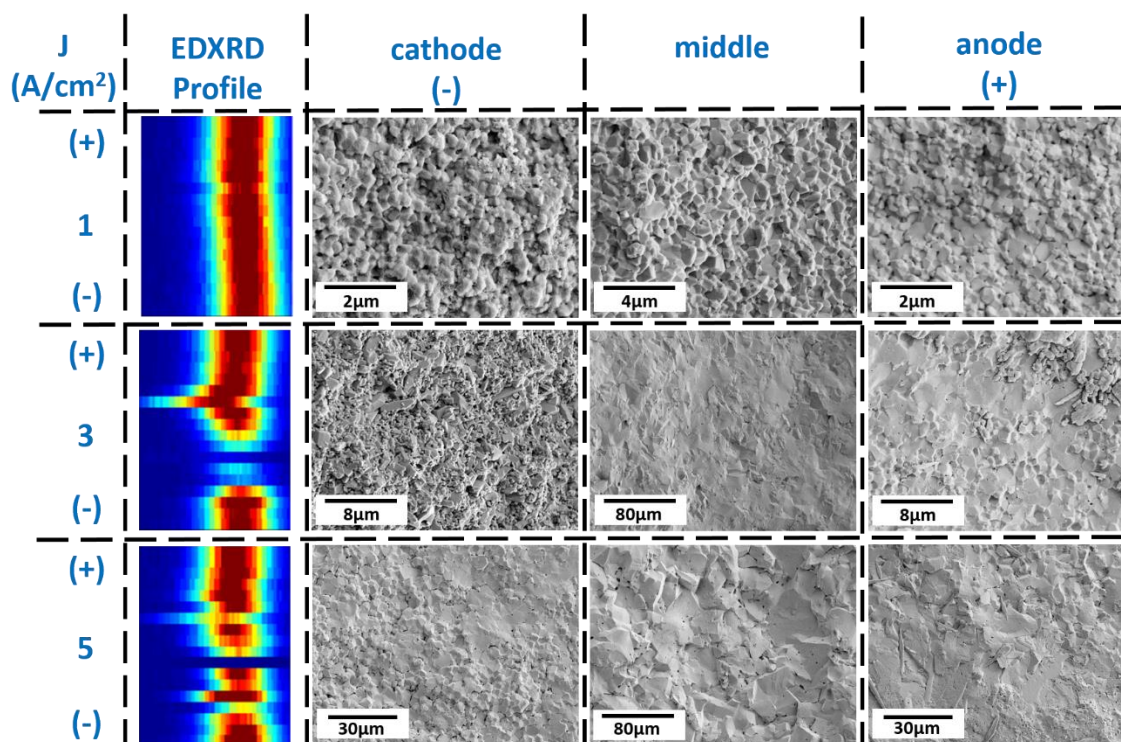
Figure 50: Profile contour maps of the strain in the diffraction peak from Miller index (101) of TiO_2 flashed at 1 A·cm^{-2}, 3 A·cm^{-2}, and 5 A·cm^{-2}. Accompanying fracture surfaces showing the grain sizes at the in the anode, middle, and cathode regions.
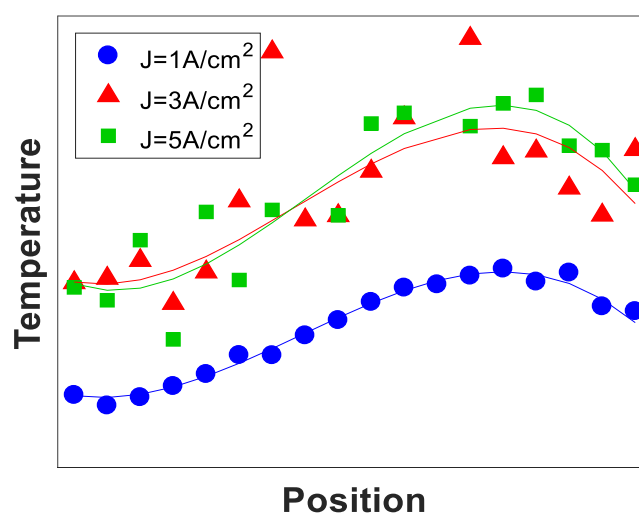
Figure 51: Cubic fitting of temperature distribution for profiles 1 A·cm^{-2}, 3 A·cm^{-2}, and 5 A·cm^{-2} based on cubic solution to the heat equation with linear Peltier effect.
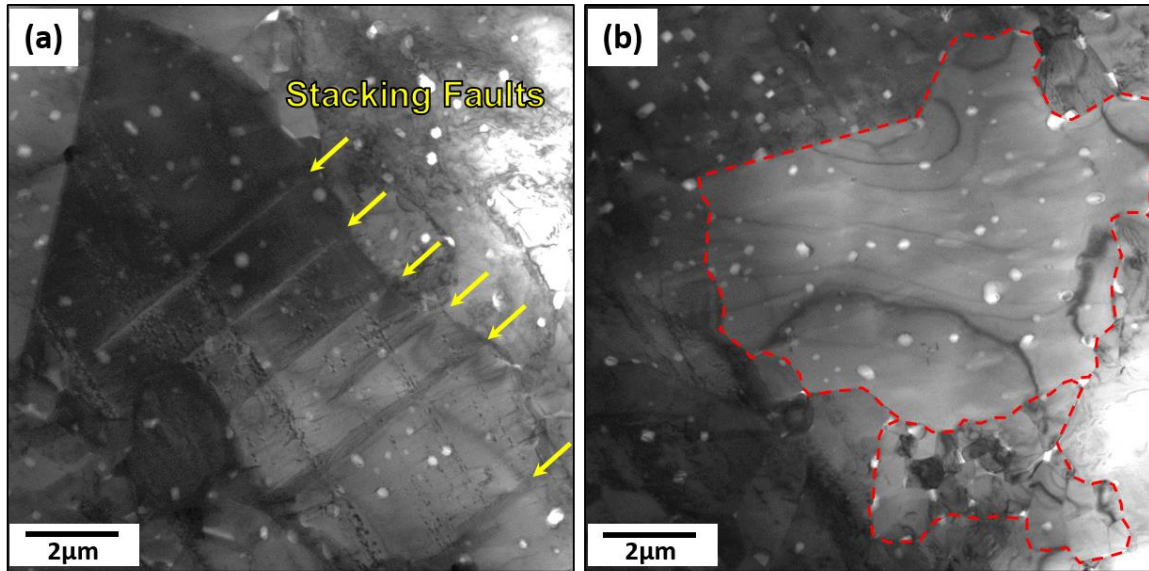
Figure 52: (a)-(b) TEM images from the anode side of J = 5 A·cm^{-2} specimen. Stacking faults are marked by yellow arrows (a) and bimodal grain size distribution are marked by red dash line (b). High density of intragranular pores is evident in large grains. TEM images are shown, with permission, by Dr. Haiyan Wang's group at Purdue University.

In comparison with the microstructure in FS, the same behavior was apparent in CS (Fig. 54). Submicron grains and remaining open porosity at 1000 °C became ~1 μm and low porosity at 1050 °C. As the maximum sintering temperature increased to 1100 °C abnormal grain growth along with bimodal grain size distribution occurred, which is comparable to microstructure near the anode for FS at 5 A·cm^{-2}. Heating to 1150 °C caused a huge grain growth to ~18.5 μm. In this context the huge difference in grain size for FS samples at different regions is comparable to the sudden grain growth with relatively small change in CS temperature.
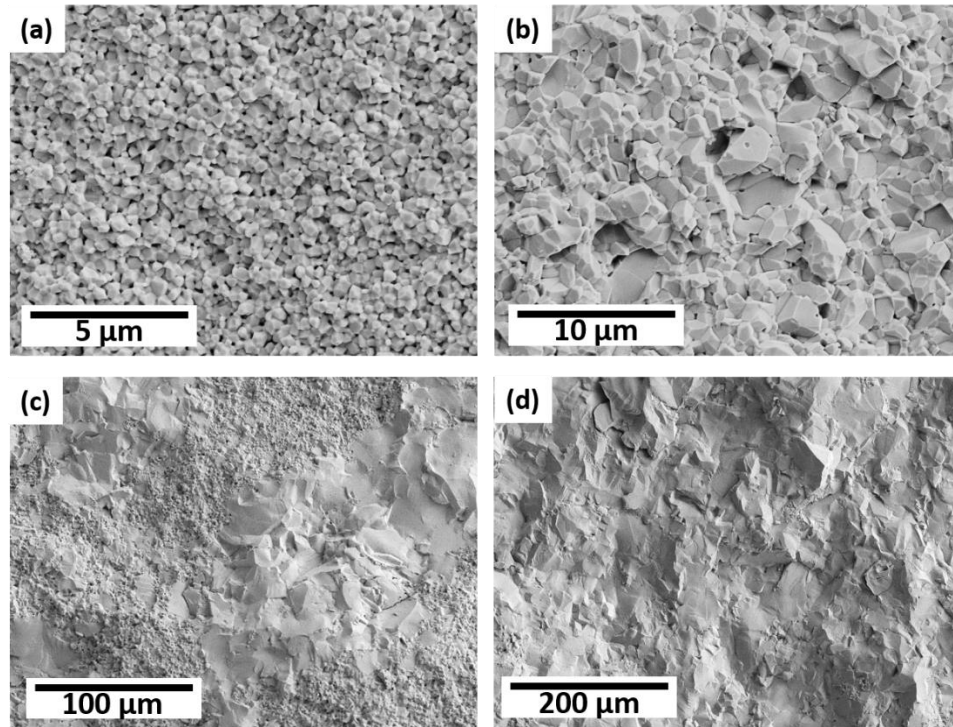
Figure 53: Comparison of microstructure during conventional sintering to (a) 1000°C, (b) 1050°C, (c) 1100°C, and (d) 1150°C. Runaway grain growth, (c) and (d), and bimodal grain size distribution, (c), evident in conventional sintering when heating past required sintering temperature.
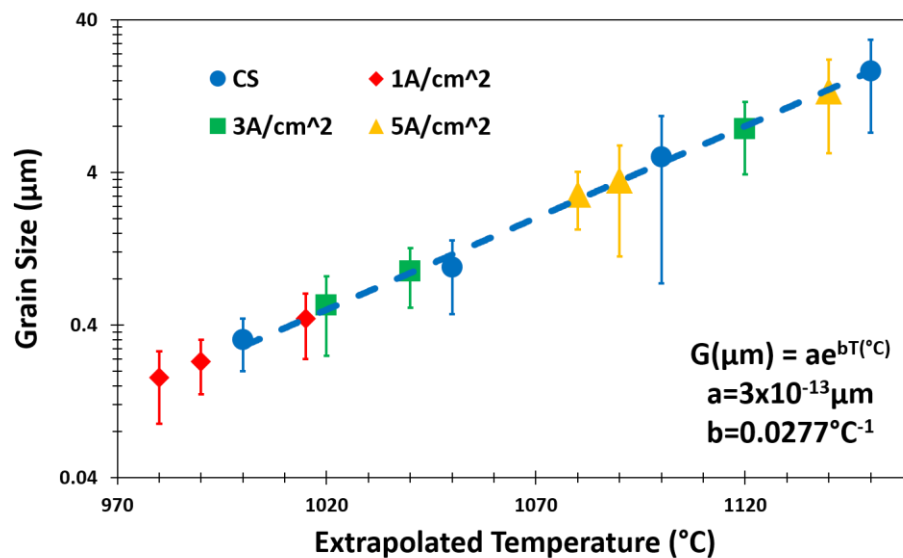
Figure 54: Fitting of exponential growth of grain size with respect to temperature for conventional sintering. Grain size of cathode, middle, and anode for 1 A·cm^{-2}, 3 A·cm^{-2}, and 5 A·cm^{-2} fitted to curve, which allows for extrapolation of temperature approximation.

By fitting an exponential function to the average grain size of the CS samples,

$$G(\mu m) = ae^{bT(°C)}, \text{ with } a = 3 \times 10^{-13} \text{ } \mu m \text{ and } b = 0.0277 \text{ } °C^{-1},$$ (5.2.5)

the temperatures for the cathode, middle, and anode of the FS samples can be extrapolated (Fig. 55 and Table 6). These temperatures are in agreement with the temperatures derived from the EDXRD temperature calibration.

Table 6: Average grain size along with standard deviation approximated using Lince software. Using exponential growth model allows temperature extrapolation of cathode, middle, and anode for 1 A·cm^{-2}, 3 A·cm^{-2}, and 5 A·cm^{-2}.

Condition	Average Grain Size (μm)	Standard Deviation (μm)	Extrapolated Temperature (°C)
CS-1000°C	0.32	0.12	1000
CS-1050°C	0.95	0.48	1050
CS-1100°C	5.06	4.31	1100
CS-1150°C	18.47	11.17	1150
FS-1 A·cm^{-2} cathode	0.18	0.09	980
FS-1 A·cm^{-2} middle	0.44	0.20	1015
FS-1 A·cm^{-2} anode	0.23	0.09	990
FS-3 A·cm^{-2} cathode	0.54	0.29	1020
FS-3 A·cm^{-2} middle	7.75	3.86	1120
FS-3 A·cm^{-2} anode	0.90	0.38	1040
FS-5 A·cm^{-2} cathode	2.87	1.18	1080
FS- 5 A·cm^{-2} middle	13.59	8.27	1140
FS-5 A·cm^{-2} anode	3.55	2.43	1090

Geometric measurements of overall sample density were also performed. For the FS experiments, 1 A·cm^{-2}, 3 A·cm^{-2}, and 5 A·cm^{-2}, the specimen density measured 91%, 96%, and 98%, respectively. For the CS experiments, 1000 °C, 1050 °C, 1100 °C, and 1150 °C, the specimen density measured to 88%, 94%, 96%, and 96%, respectively.

5.2.5 Discussion

The asymmetric lattice expansion can be modeled with a cubic function as given in Eq. (5.2.4) according to the heat equation with internal heat generation and the Peltier effect. Furthermore, the grain size at the cathode, middle, and anode confirm that the differential heating is the predominant factor controlling the microstructure under flash conditions. As the Peltier effect is a Joule heating effect this suggests that the predominant mechanism in flash sintering of TiO_2 is Joule heating.

To achieve uniform microstructure use of an AC power supply is preferable as the Peltier effect does not cause an asymmetric heating profile due to the constantly changing direction of the electric field. In this case there will be less sintering at the two ends due to the temperature drop from thermal conduction, but these can be ground away in post processing.

EDXRD temperature calibration confirms that a purely radiative temperature model will overestimate the temperature for specimen inside a stage due to thermal conduction. However, dogbone specimens were not tested and their temperatures may be approximated with greybody radiation as there is minimal contact for thermal conduction since the dogbone is suspended with thin wires through holes at the two ends.

For the observed shoulder formation in Fig. 49, we present three possible explanations:

1- The current may have taken preferred paths through the sample, which will give higher than average temperatures where current localizes and lower than average temperatures where there is no power. As EDXRD takes the sum of the statistics from a gauge volume, with cross section 2 mm x 0.2 mm in this case, the counts will come from both parts of the volume, yielding a range of bond lengths corresponding to different temperatures. However, in this case, SEM analysis should yield microstructural inhomogeneity in regions parallel to the path of the current, which was not observed.

2- Local heating at the grain boundaries results in two peaks: one for the bulk and one for the grain boundaries. This would support predictions of grain boundary melting (156) or softening (158), which would greatly enhance the sintering rate through liquid phase sintering. However, the volume fraction of peaks at higher temperature is too high to be coming from grain boundary melting, which would only affect a small portion of the volume near the grain boundaries. In addition, liquid phase sintering should be visible in the microstructure. A previous study with CeO_2 (171) shows a more distinct double peak formation towards the cathode which has an inverse relationship with grain growth/sintering in contradiction to the previous prediction. In addition, such a high temperature rise at the grain boundaries (Table 7) should distribute to the bulk quickly (37, 175).

Table 7: Peak positions and temperature from temperature calibration, for main peak and shoulder peak maxima at 3 A·cm^{-2} and 5 A·cm^{-2}.

Current Density (A/cm^2)		Unit Cell Volume (Å^3)	Temperature (°C)
3	TiO_2	64.8510	1225
	$TiO_{2-\delta}$	66.1593	1700
5	TiO_2	64.5174	1090
	$TiO_{2-\delta}$	67.1227	2015

3- Reduction of a percentage of the unit cells of TiO_2 due to oxygen ion conduction causes bifurcation to two peaks: stoichiometric TiO_2 and nonstoichiometric $TiO_{2-\delta}$. This result is in agreement with the aforementioned study of CeO_2.

Reduction of TiO_2, is likely the cause of the peak splitting. However, this does not infer enhanced sintering as the rate limiting step is diffusion of the larger Ti^{4+} ions and is likely the byproduct of the high temperature at those positions, as higher temperature also enhances oxygen ion transport under the applied electric field either directly, through enhanced diffusion kinetics in the bulk, or indirectly through abnormal grain growth, which reduces the number of grain boundaries and, thus, oxygen vacancy traps (222).

It has also been observed (176) that there are two types of charge transfer during flash sintering of TiO_2, electrons and O^{2-} ions, the latter of which results in a visible blackening nearer to the positive electrode and has been confirmed using X-ray photoelectron spectroscopy (XPS) and Raman spectroscopy. This blackening coincides with enhanced densification and grain growth.

Comparison of microstructure for FS to the grain growth model from CS shows that the level of grain growth is in line with CS at the same temperatures. The abnormal

grain growth and bimodal grain size distribution that occurs with sufficiently high current density is also found in CS with sufficiently high temperature. Approximation of temperatures from EDXRD further confirms this conclusion.

One key difference is the shorter sintering times due to the rapid heating to maximum specimen temperature during flash. Fast heating rates are known to enhance the grain boundary diffusion leading to enhanced densification during flash sintering at temperatures comparable to conventional sintering (37, 99, 175). In addition, numerous results on conventional fast firing have demonstrated this effect without applied electric field (166-168). Proposed theories for this effect include the avoidance of grain coarsening due to the rapid heating to sintering temperature and destabilization of the grain boundaries from their equilibrium states, producing grain boundaries with diffusive structures that allow enhanced mass transport.

5.2.6 Conclusions

In this work we present an alternative route to measuring the temperature of the specimen during flash by calibrating the lattice parameters during FS to CS. This approach allows bulk measurement, unlike pyrometers which measure surface temperature. The temperatures for FS have been confirmed to be comparable to CS as has also been reported for ZnO (170). In addition, by using synchrotron radiation rapid measurements can be made including profile scans, which have shown a significant Peltier effect in TiO_2 which corresponds to microstructure inhomogeneity in the sample. Thus, for n-type semiconductor oxide ceramics Joule heating appears to be the dominant mechanism of sintering. The time required for sintering is lowered, but this is in line with other reported results of fast firing, potentially due to the destabilization of grain boundary "complexions"

during rapid heating (37). Use of an AC power supply is recommended to achieve uniform microstructure by avoiding the Peltier effect or directional reduction.

5.2.7 Appendix A – Energy Dispersive X-Ray Diffraction

According to Bragg's law,

$$n\lambda = 2d_{hkl} \sin \theta, \qquad (5.2.7.1)$$

where n is a positive integer, taken as 1, λ is the incident wavelength d_{hkl} is the d-spacing of the Miller index, hkl.

Since the energy of a photon, $E = h\nu = hc/\lambda$, with Planck's constant $h = 6.626 \times 10^{-34}$ J·s,

$$E_{hkl}(keV) = \frac{hc}{2d_{hkl} \sin \theta} = \frac{6.1992(keV \cdot Å)}{d_{hkl} \sin \theta}, \qquad (5.2.7.2)$$

The x-rays are collected in a germanium detector where penetration depth (channel #) into the detector is proportional to the energy of the x-ray. Thus,

$$E_{hkl} = A + B * channel, \qquad (5.2.7.3)$$

from which the d-spacing of the diffracted beam can be calculated using equation 5.2.7.2.

After tracking the d-spacing of the diffracted peaks, the lattice parameters can be calculated depending on the geometry of the unit cell. Rutile TiO2 has a tetragonal unit cell. The lattice parameters can be solved using the following equation,

$$\frac{1}{d^2} = \frac{h^2 + k^2}{a^2} + \frac{l^2}{c^2}, \qquad (5.2.7.4)$$

with two equations from the d-spacings of the Miller indices (110) and (101). From these parameters the unit cell volume is determined,

$$V = a^2 c .$$ (5.2.7.5)

Calculation of fitting equation during conventional heating gives a and c lattice parameters, unit cell volume, and c/a ratio.

$$a = (8.185 \times 10^{-9})T^2 + (3.446 \times 10^{-5})T + 4.592$$ (5.2.7.6)

$$c = (8 \times 10^{-9})T^2 + (2.798 \times 10^{-5})T + 2.957$$ (5.2.7.7)

$$V = (4.159 \times 10^{-7})T^2 + (1.52 \times 10^{-3})T + 62.37$$ (5.2.7.8)

$$c/a = (5.717 \times 10^{-10})T^2 + (1.268 \times 10^{-6})T + 0.644$$ (5.2.7.9)

5.2.8 Appendix B – Greybody Radiation and Thermal Conduction Model

Starting from the blackbody radiation model presented by Yang, et al. (8),

$$I_o + I = \sigma T^4,$$ (5.2.8.1)

where $I_o = \sigma T_o^4$ is the blackbody radiation generated by the sample in the furnace without flash (W·cm^{-2}), I is the extra blackbody radiation generated due to the power dissipation during flash (W·cm^{-2}), σ is the Stefan-Boltzmann constant (5.67 x 10^{-12} W·cm^{-2}·K^{-4}), and T is the sample temperature (K). This model assumes a perfect blackbody with emissivity, $\epsilon = 1$, but we instead need to take $\epsilon \sim 0.9$ for oxides (79). It is important to note that this is an approximation since ϵ value is a function of temperature as well as wavelength.

This greybody radiation model now reads

$$I_o + I = \epsilon\sigma T^4, \tag{5.2.8.2}$$

with $I_o = \epsilon\sigma T_o^4$. This results in a modest increase in the temperature approximation.

In the case of a dogbone, hanging from two platinum wires, the effect of thermal conduction is negligible. Thus, this greybody radiation model alone is sufficient to get a good approximation of the temperature during flash sintering of dogbone specimens.

However, in the case of cylindrical pellets, the specimen is wedged between a bottom and top pushrod. In this case there can be significant thermal conduction out of the sample due to the temperature difference between sample and alumina pushrod which is at furnace temperature. We add a thermal conduction factor to modify this equation,

$$I_o + I = \epsilon\sigma T^4 + I_{conduction}(t, x), \tag{5.2.8.3}$$

where $I_{conduction}$ is the power loss per unit area (W·cm^{-2}) due to conduction to the electrodes.

In the case of the steady state of flash there are constant specimen and stage temperatures and constant cross sectional area. The temperature gradient reduces to

$$I_{conduction} \sim \frac{k}{L/2}\Delta T, \tag{5.2.8.4}$$

where k is the material dependent thermal conductivity factor (W·cm^{-1}·K^{-1}), L is the thickness of the pellet, and $\Delta T = T - T_c$, T_c is the temperature at the contacts. The final temperature can be computed using a greybody radiation and thermal conduction model,

$$I_o + I = \epsilon\sigma T^4 + \frac{2k}{L}\Delta T. \tag{5.2.8.5}$$

5.2.9 Appendix C – Temperature distribution with Peltier Effect and Thermal Conduction

The heat equation with internal heat generation takes the form,

$$\frac{dT}{dt} = \frac{k}{c_p \rho A} \nabla^2 T + \frac{P_V}{c_p \rho A} \, , \qquad (5.2.9.1)$$

where k is the thermal conductivity (W·cm^{-1}·K^{-1}), c_p is the specific heat capacity (J·K^{-1}), ρ is the material density (kg·cm^{-3}), A is the cross sectional area, $\nabla^2 T$ is the Laplacian of the temperature, and P_V is the internal power density (W·cm^{-3}) i.e. power per unit volume of specimen.

At steady state, $\frac{dT}{dt} = 0$ and taking a 1D approximation (5.2.8.4) can be simplified to (5.2.8.5)

$$\frac{d^2 T}{dx^2} = -\frac{P_V}{k} \, , \qquad (5.2.9.2)$$

where P_V is generally taken as constant over the specimen length. However, this is misleading as the power density predicted by the continuous Peltier effect (Thomson effect) is higher towards the anode (+) for n-type semiconductors. A linear power gradient through the specimen,

$$P_V = f(x) = ax + b \, , \qquad (5.2.9.3)$$

where a and b are fitting constants, results in the ODE of the form,

$$\frac{d^2 T}{dx^2} = -\frac{1}{k}(ax + b) \, . \qquad (5.2.9.4)$$

The solution to this equation is cubic,

$$T = -\frac{a}{6k}x^3 - \frac{b}{2k}x^2 + C_1 x + C_2 \,, \tag{5.2.9.5}$$

which can be solved with the boundary values $T(0) = T_1$ and $T(L) = T_2$,

$$T(x) = -\frac{a}{6k}x^3 - \frac{b}{2k}x^2 + \left(\frac{T_2 - T_1}{L} + \left(\frac{aL}{3} + b\right)\frac{L}{2k}\right)x + T_1 \,. \tag{5.2.9.6}$$

For AC electric field, Peltier effect does not apply so $T(0) = T_o$ and $T(L) = T_o$ giving a quadratic solution to Equation (5.2.9.2) with $P_V = $ constant such that

$$T(x) = -\frac{P_V}{2k}x^2 + \frac{P_V L}{2k}x + T_o \,. \tag{5.2.9.7}$$

6. CeO₂ – Preferential Non-stoichiometry and Temperature Approximation

6.1 In-situ Observation of Oxygen Mobility and Abnormal Lattice Expansion in Ceria during Flash Sintering

6.1.1 Disclaimer

6.1.2 Introduction

Sintering is the prime method in manufacturing ceramic components, wherein powders are compacted and heated to a suitably high temperature for solid state diffusion of particles along the grain boundaries, which results in densification. Although sintering polycrystalline materials has provided a cheaper alternative to single crystal ceramics at the expense of somewhat deteriorated properties, it is still a slow and energy intensive process. In addition, problems arise due to grain growth, chemical decomposition, and impurity segregation, among other issues. Many methods of sintering, such as spark plasma sintering (SPS), hot pressing (HP), and microwave sintering (MW) were developed to alleviate these problems. Flash sintering is one of the latest sintering techniques, (6) which lowers the sintering temperature and enhances the kinetics of densification. A wide range of ceramic materials, including insulators and high dielectric materials (43, 70, 87, 113, 115, 147, 228), semiconductors (79, 90, 94, 99, 175, 176, 179), electronic conductors (66) and ionic conductors (6, 49, 54, 66-69, 78, 125, 229) have been sintered using this technique. The enhanced kinetics at lower temperatures have given rise to a debate about the mechanism(s) responsible for flash sintering. Recent papers have proposed mechanisms such as local Joule heating (30, 63, 95, 131, 151, 170), pore migration (50, 55, 131), liquid phase sintering (145, 156, 230), fast heating rates (37, 130) and defect generation (27, 29, 43, 64, 70, 71, 80, 84, 117, 155, 192).

Flash sintering has found applications in co-sintering of composites (54, 71, 80, 86, 92, 111, 112, 117, 120, 177) and difficult-to-sinter ceramics (106, 107, 118, 172, 231). While presently studied ceramics seem to make the transition into the flash state at comparable electrical power densities of $10 - 50$ W/cm^3 (192), it is notable that the

contribution of Joule heating differs from one material to another. For example, while flash sintering of ZnO, an electronic conductor, has been determined to be predominantly caused by Joule heating (95, 96, 99, 169, 170), the sintering of ionic conductors is predicted to be caused or aided by defect generation (6, 22, 29, 43, 49, 54, 64, 68, 70, 78, 125, 232). Regardless of the mechanism proposed, flash sintering has been related to the conductivity of the specimen, which can be altered by either doping (43, 49, 67-69, 73, 78, 83, 90, 115, 125) or changing the oxygen partial pressure or environment (38, 94, 96, 99). For non-oxide ceramics, a modified spark plasma sintering has been developed and named flash spark plasma sintering (FSPS) (135, 139, 233). A few literature review works (4, 189, 194) on flash sintering also provide a good overview of flash sintering progress to date.

In the current study, the effect of electric field on undoped ceria, CeO_2, was studied since it is predominantly an ionic conductor, at lower temperatures than 8 mol.% yttria stabilized zirconia (8YSZ), and does not have extrinsic defects resulting from doping. In the first in-situ work on flash sintering by Akdoğan et al. (52), abnormal peak broadening was observed during flash sintering of 8YSZ. Since then, many in-situ diffraction measurements have been performed for TiO_2, and composites containing TiO_2 (82, 84, 86, 176), YSZ (27, 29, 32, 173), TiB_2 (112), $BiFeO_3$ (172) and ZnO (170) in which peak positions of certain planes are used to relate the thermal expansion during flash sintering. The effect of an electric field was investigated along the path of the current (i.e. across the height) through the specimen and a resulting directionality effect, which has been linked to non-stoichiometry. Microstructural comparison corroborates the theory of ionic diffusion as the primary mechanism for conductivity and mechanism for densification and grain growth.

6.1.3 Experimental Procedure

Commercially available nanopowder of ceria (CeO_2) was obtained from Sigma Aldrich (Cerium (IV) oxide, nanopowder, 99.95% (trace rare earth metal basis) <50 nm APS, BET). The powder was pressed under a uniaxial pressure of 200 MPa at room temperature to an average density of 52.5% ± 2.1 in a cylindrical die. The cylindrical green compacts were measured with diameter of 0.6 cm and height varying from 0.37-0.40 cm.

The temperature of the furnace was held at 900 °C during the flash experiments. An electric field of 100 V/cm was applied across the two faces of the ceria cylinder, as shown in Fig. 57. AC and DC power supplies (Pacific Power Sources, model ACX 118 and B&K Precision power supply) were used with maximum current density of 10 A/cm^2.

For the in-situ experiments that were run at the synchrotron facility at Argonne National Laboratory, the furnace was placed in the path of a white X-ray beam (a schematic diagram is shown in another work (170)) and the detector was placed 3 degrees from the path of the beam. The experiments were carried out in transmission geometry with the diffraction volume determined by the parallelepiped geometry. Two kinds of diffraction data acquisition were used. In type I, the diffraction volume was brought into the center of the specimen and the sample temperature was tracked during flash sintering. This provided time-resolved diffraction peaks during flash sintering. To obtain the spatial lattice expansion during the flash, the sample stage was moved vertically in the y-direction to obtain a profile from top electrode to bottom electrode. Since movement of the stage takes time, it can be obtained before the flash, during flash in the steady state (stage III) (31), and after turning off the electric field, but not during the transition stages. An acquisition time of 2 seconds with a data processing time of 0.5 second was used to obtain the Energy

Dispersive X-ray diffraction (EDXRD) spectrum. This time was chosen based on the attenuation and diffraction intensity of the X-rays passing through the furnace and specimen.

For calibration purposes, one specimen of ceria was heated up to 1300 °C under a ramp rate of 10 °C/min. As the temperature rises, the cubic ceria lattice expands. This is observed in terms of peak shift to lower energies since the interplanar spacing is inversely proportional to the energy of diffraction wavelength according to the Bragg's law $E = \frac{hc}{2\,sin\,\theta}(\frac{1}{d_{hkl}})$. This effect has been schematically represented in Fig. 56 for the (220) peak of ceria. Based on this peak shift, the interplanar spacing of the (220) plane was calculated and plotted against temperature in Fig. 56, along with its peak width. Since ceria has a cubic structure, one parameter is sufficient for calibration. The lattice expansion was verified to be homogenous in the other two calculated planes, (311) and (222). Since peak width is associated with crystallite size, larger grains produce more narrow peaks. Peak widths are also associated with strain but since ceria is a ceramic, it is largely crystalline size effect. The calibration standard of ceria shows that necking starts at 800 °C and sintering is completed by the time the furnace temperature reaches 1100 °C, based on change in full width half maxima (234). The non-linear rise in the lattice expansion has been linked with non-stoichiometry in ceria at higher temperatures (235), which results in a structural disorder of oxygen ions in ceria. The distortion is highest in the <111> direction and oxygen diffusion is facile, meaning certain planes have a higher diffusion rate than others.

Higher temperature cause lattice expansion

$T_o \longrightarrow T$

Counts

Energy (KeV)

Interplanar spacing (Å)

FWHM (keV)

Temperature (°C)

where,
h=planks constant in KeV-s
c=speed of light, m/s
θ = Diffraction angle, radian

$$E = \frac{hc}{2 Sin\theta}\left(\frac{1}{d_{hkl}}\right)$$
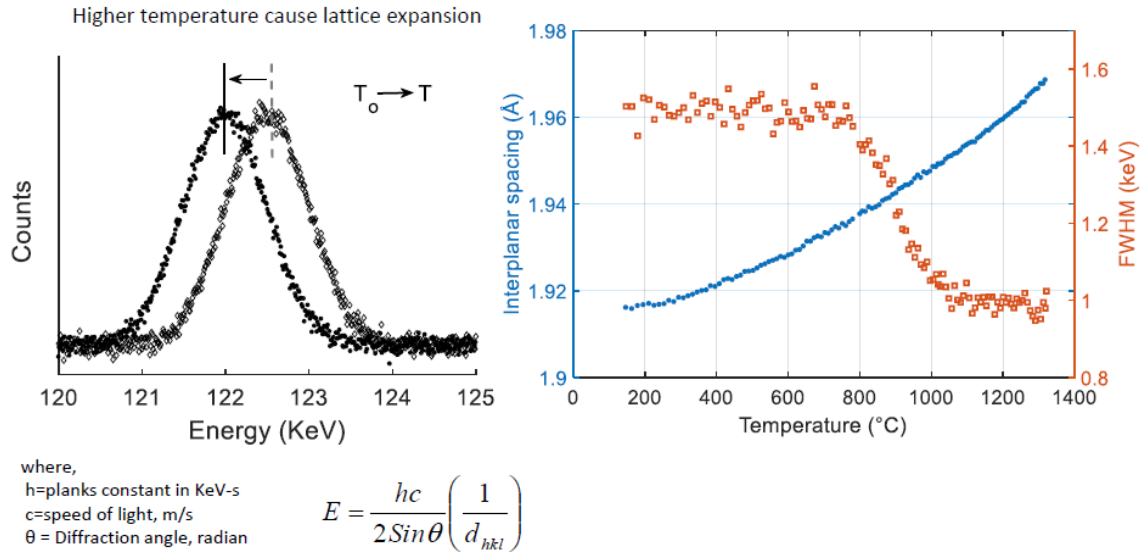
Figure 55: The effect of heating on shift of diffraction peak to a lower energy, because of lattice expansion according to the Bragg's law. (b) shows the calibration of interplanar spacing of (220) peak with temperature. The FWHM of the peak suggests that necking starts at around 800 °C on heating in conventional set-up and densification is complete by 1100 °C.

After the specimens were flash sintered, plan-view TEM samples were prepared through grinding, polishing, dimpling and final polishing in a precision ion milling system (PIPS II, Gatan). A FEI TALOS TEM/STEM with ChemiSTEM technology (X-FEG and SuperX EDS with four silicon drift detectors) operated at 200 kV was used in this study for microstructure characterization and energy-dispersive X-ray spectroscopy (EDS) chemical mapping.

6.1.4 Results

A flash sintering experiment is shown in terms of electric field, current density, and power density in Fig. 57a, with expanded view of start and end of flash sintering in Fig. 57(b) and 57(c), respectively. The sample was brought into thermal equilibrium with the furnace by holding the furnace isothermally at 900 °C for 5 minutes before applying the

electric field. The current quickly rose in response and within 10 seconds reached its predetermined current density limit of 10 A/cm^2. At this point the power supply went into current control, i.e. stage III. The specimen was held under an excited state of flash for 1000 seconds before the electric field was turned off. Using the EDXRD technique the lattice expansion was tracked during the flash transition, as shown in Fig 57(d) and 57(e). The detailed contour plot and peak fitting data used for calculation are shown in Fig. 58. The full width at half maxima (FWHM) of the peaks remained almost unchanged during flash sintering, except for a single data point that may have been the result of relatively long acquisition time of 2.5 seconds during which the interplanar spacing of (220) shifts from 1.939 Å, at 900 °C, to 1.954 Å. Fitting to the calibration curve suggests that the actual specimen temperature should have reached no higher than 1150 °C, which is in the range of the conventional sintering temperature of the ceria nanopowder. On turning off the electric field, the sample started cooling down quickly to the furnace temperature, which is noticed in terms of lattice contraction. Even after a period of ~ 50 seconds, it did not reach the equilibrium interplanar spacing of plane (220) corresponding to the furnace temperature, 900 °C. This could be either because of slow thermal relaxation time or formation of oxygen vacancies or gradual annealing of structural defects and dislocations that gets generated during flash.
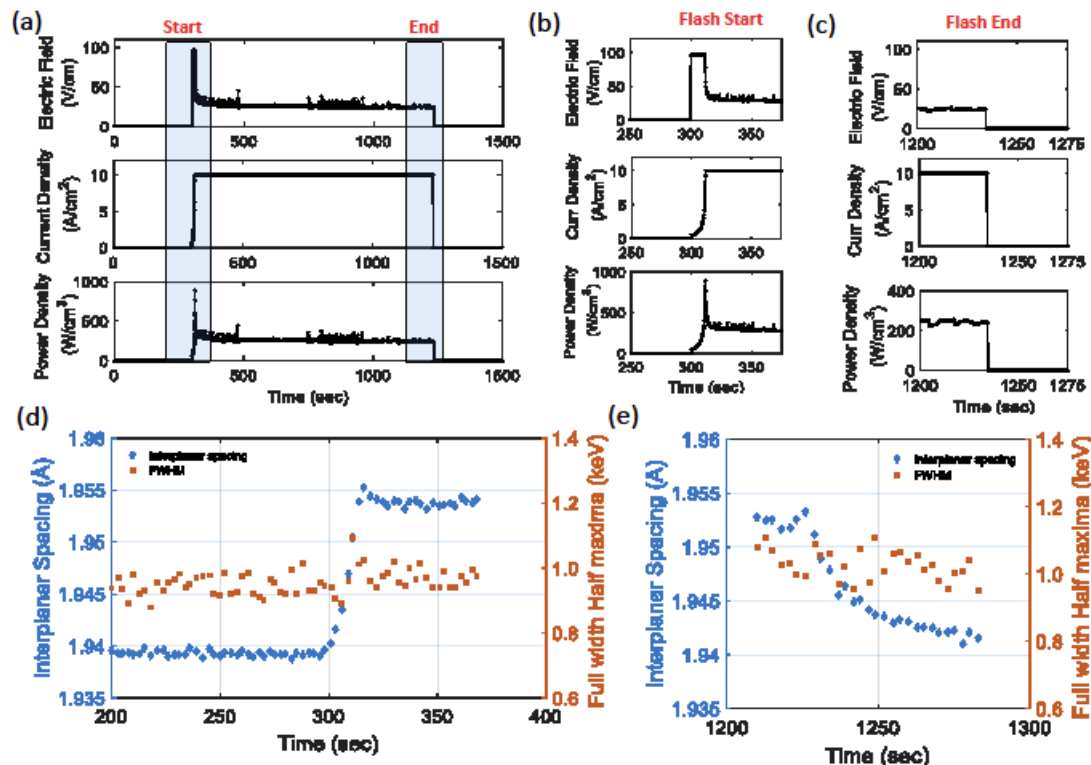
Figure 56: Flash parameters during an in-situ flash experiment under direct current (DC) electric field, the expanded time scale at start and end of flash are shown in subplots (b) and (c) with their respective interplanar spacing of (220) planes as shown in (d) and (e). Reference to the calibration plot in supplementary S1 suggests that ceria reaches conventional sintering temperature under flash.
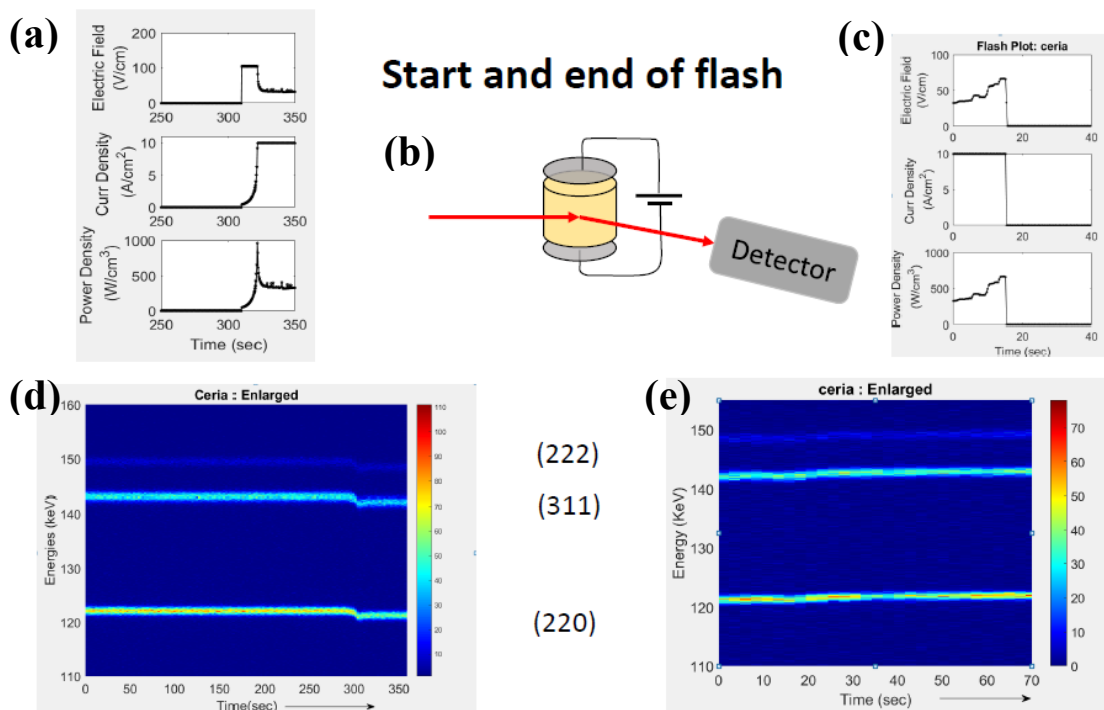
Figure 57: The mapping of XRD color contour. The Y axis is in energy (which is inverse of interplanar spacing). The change in energy after 300 s, shown by (d), corresponds to a lattice expansion. Thermal relaxation of the (220) peak after turning off the electric field, shown in (c) and (e), indicates gradual cooling down of specimen, but never reaches its equilibrium position corresponding to the furnace temperature, suggesting remnant defects in the structure.

During the 1000 s hold time under flash, profile scans were run on ceria to determine if there is an inhomogeneity in the specimen caused by an electrode effect. An abnormally large lattice expansion near the negative electrode (cathode) was observed. When the polarity of the specimen was switched in the next flash sintering experiment, the direction of the lattice expansion was reversed, as shown in Fig. 59(a), 59(b) and 59(c). Fitting of the peaks revealed that at the cathode end, the peak broadened and split into two peaks, corresponding to two different lattice parameters. The peak splitting indicated by the shoulder formation can be rationalized as the segregation of Ce^{3+} and oxygen vacancy defects that gives different lattice parameters, resulting in some unit cells having less

oxygen than others. This non-stoichiometry causes continuous lattice expansion with time, as was observed in the trend of lattice expansion with consecutive flash profiles, shown in Fig. 60. When the experiment was repeated using an AC electric field with the same electrical parameters, no such directionality was noticed during the profile scans, Fig. 61 (and Fig. 62). Another interesting observation was that platinum paste had a major influence in this abnormal lattice expansion, which disappeared when no platinum paste was used, shown in Fig. 63. Platinum paste is generally used in flash experiments to provide a good electrical contact between the electrodes and the specimen, but in this case it acted as blocking electrode. This aspect of the electrode effect has also been mentioned in the work of Biesez (46) and Caliman et. al. (103), where silver paste seemed to have facilitated cationic exchange in β –alumina in comparison with platinum paste which had a blocking effect on the flash sintering, requiring a higher temperature to sinter under the same electric field.
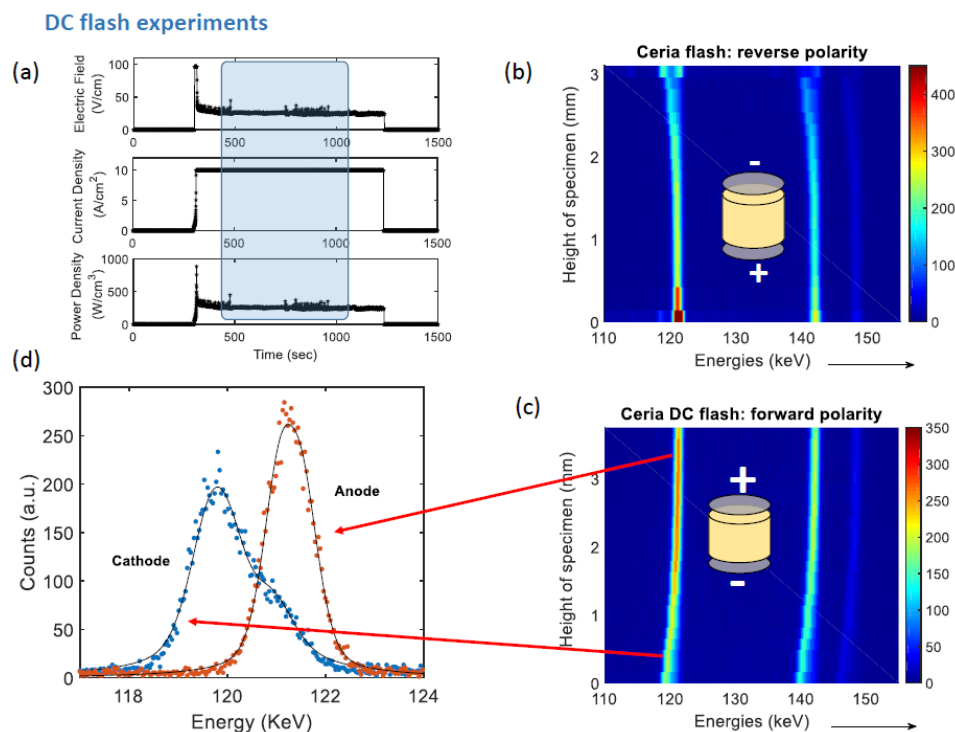
Figure 58: (a) The flash experiment parameters, where the blue shaded inset shows the time period for profile scan. (b) and (c) shows the abnormal non-thermal expansion at the cathode and the effect of switching the DC polarity. The direction of abnormal expansion reverse. (d) shows the peak profile of (220) plane at cathode end and anode end. The shoulder formation at the cathode shows the inhomogeneity of the lattice expansion in different unit cells.
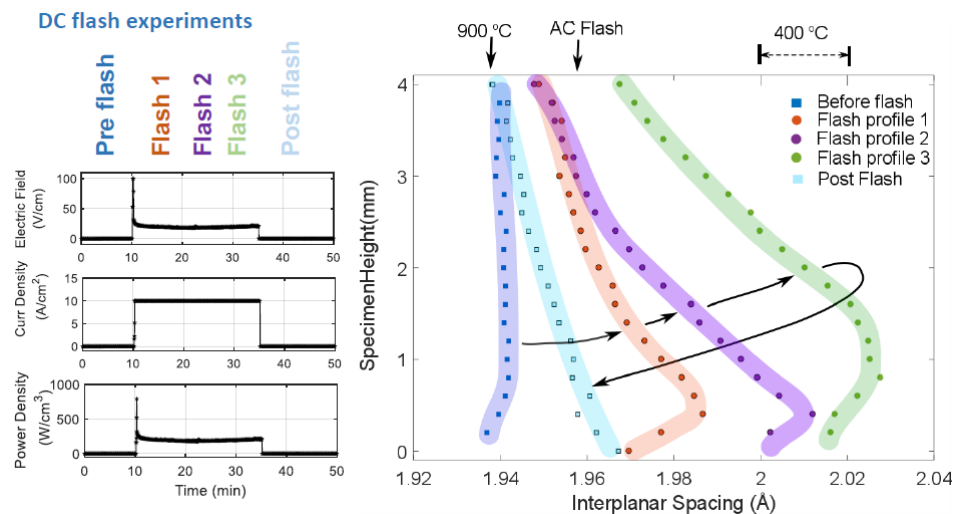
Figure 59: Based on the findings of abnormal expansion due to non-stoichiometric transition under flash, multiple profiles were run during a prolonged exposure of DC flash. The change in interplanar spacing at the cathode indicates the extent of non-stoichiometry.

Figure 60: AC flash experiment under same conditions as DC, T=900 °C, J=10 A/cm2, and f=1000 Hz. (a, b) shows the flash power density with time in two different flash experiments. Flash shown in (a) was used for timescan of lattice expansion of central point of cylindrical specimen as shown in (c) and (b) is used for lattice expansion across the

height of specimen at three stages of flash. The profile suggests no non-stoichiometry in subplot (d), i.e. homogenous densification and grain size.
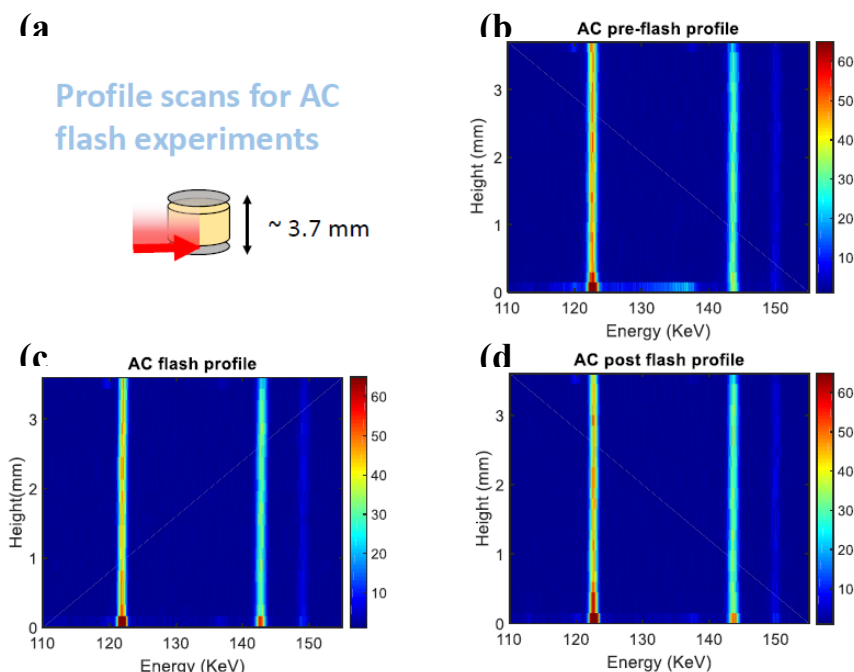
Figure 61: Contour plot of AC flash sintered sample profiles (a), (b) before flash, (c) during flash and (d) post flash sintering.
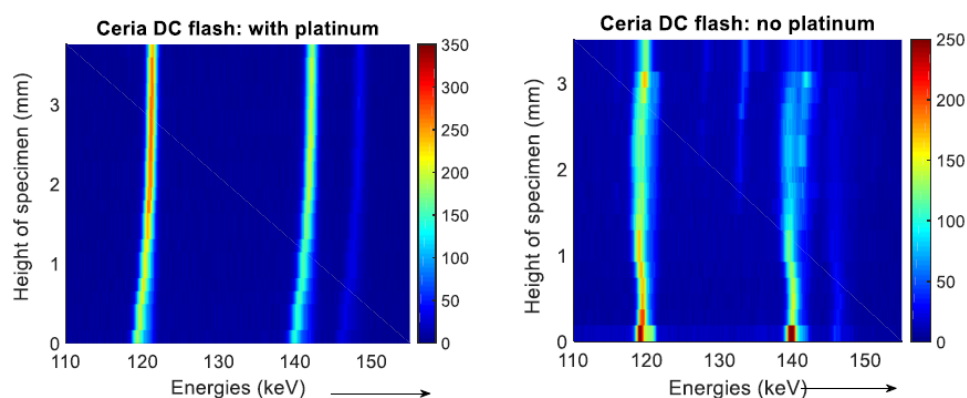
Figure 62: Platinum paste acts as the blocking electrode for oxygen ion exchange at the cathode (negative terminal), hence more lattice expansion is noticed when compared with no platinum paste conditions.

Fig. 64(a) gives a representative STEM image taken under the high angle annular dark field (HAADF) mode (also called Z-contrast imaging) from the positive side (anode). The image shows equiaxed grains with an average grain size of 10 μm. When zoomed out further, an amorphous, relatively thick grain boundary of around 2 nm was observed, (see inset Fig. 64(e)). Fig. 64(b) is the bright-field (BF) TEM images of DC flash sintered CeO_2 of the negative side (cathode). The negative side demonstrated well-defined grain boundaries with an average grain size of 3 μm. Since the negative side has a smaller average grain size than the positive side, the selected area electron diffraction (SAED) pattern showed finer diffraction spots at the cathode. The corresponding energy dispersive spectroscopy (EDS) elemental mapping of Ce and O of Fig 64(a) are shown in Fig. 64(c)-(d). Ceria deficiency and oxygen segregation can be clearly observed along the grain boundaries. To characterize the defects in the samples, a set of dark field images were taken under the $g \cdot b$ conditions. A BF image along with the corresponding dark-field (DF) TEM images taken under two different g vectors are have been previously observed in flash sintered YSZ and TiO_2 samples (209, 210).
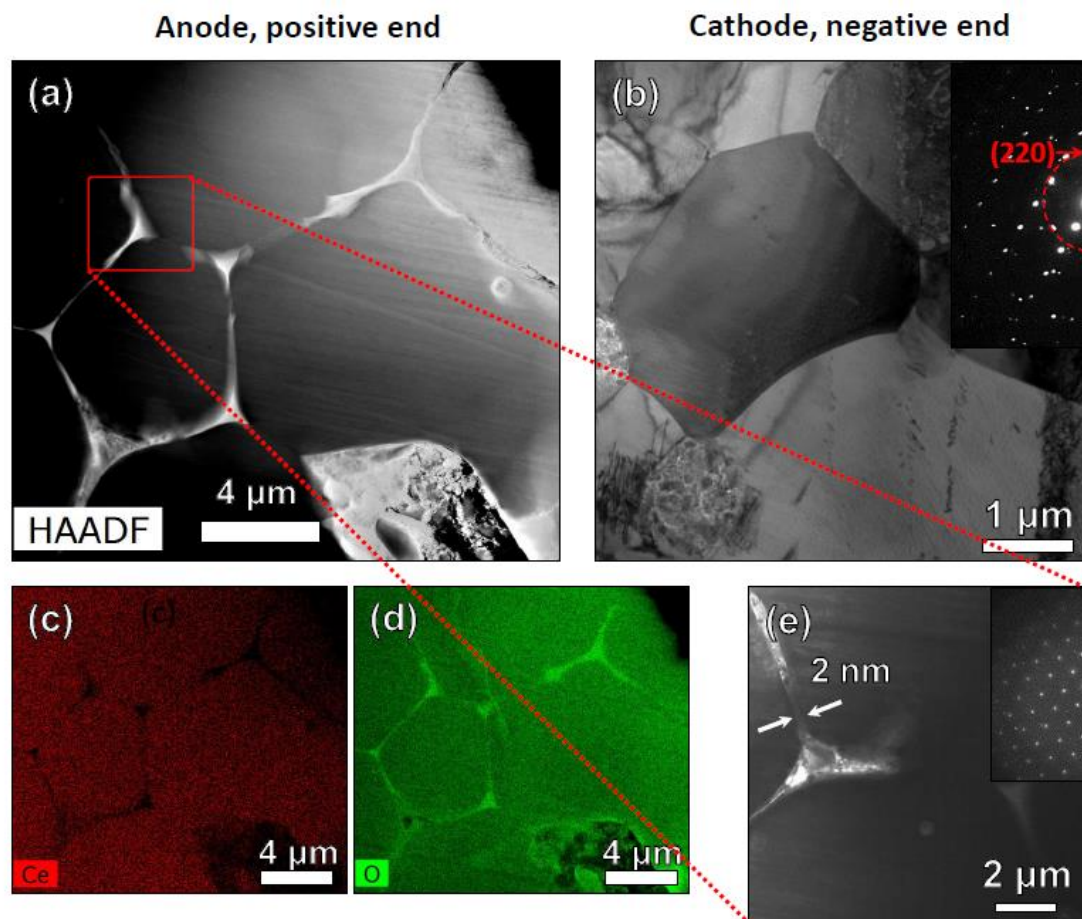
Figure 63: BF TEM images of DC flash sintered CeO_2 at the (a) positive and (b) negative ends with the diffraction pattern shown in the insets and with the corresponding elemental mapping of (c) Ce and (d) O. A magnified image of anodic side shows amorphous grain boundary with thickness ~ 2 nm. TEM images are shown, with permission, by Dr. Haiyan Wang's group at Purdue University.
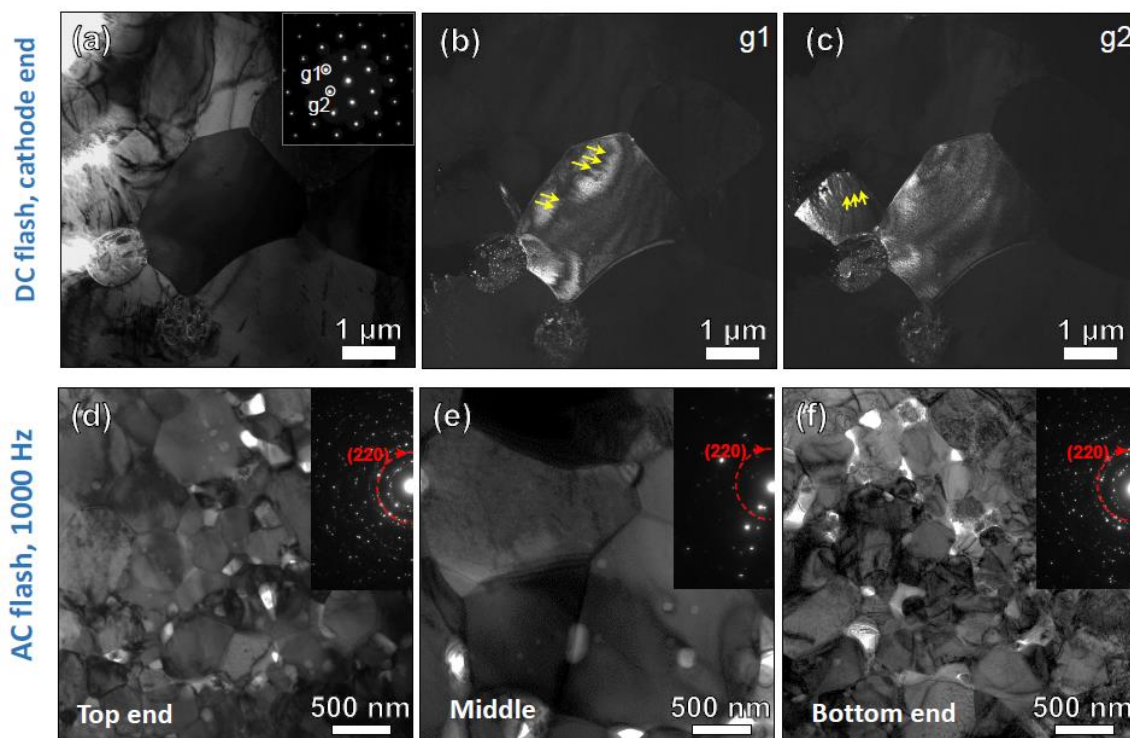
Figure 64: (a) The Bright Field TEM image with an inset of the selected area diffraction pattern of DC flash sintered CeO_2 and its corresponding Dark Field TEM images from two selected g vectors under the $g \cdot b$ conditions shown in (b) and (c). Dislocation lines are marked using the yellow arrows. Bright Field TEM images of the AC flash sintered CeO_2 at the (d) top, (e) middle and (f) bottom with corresponding diffraction patterns in the insets. TEM images are shown, with permission, by Dr. Haiyan Wang's group at Purdue University.

The microstructures of the AC flash-sintered ceria are shown in Fig. 65(d)-65(f). The grain size of the top and bottom portions are smaller than that of the middle portion, which is consistent with the SEM images shown in Fig. 66. The difference in grain size is further supported by the diffraction pattern shown in the insets. The diffraction pattern for the top and bottom portions show obvious diffraction rings, which indicate much finer grains with random orientation compared to the middle section with large grain sizes and no obvious diffraction ring. AC specimens have no preferential sintering at either electrode. Similar findings were also reported in YSZ by Qin et al. (35). The reason for this is

hypothesized to be the result of the cooling effect of the electrodes at the ends due to conduction (176).
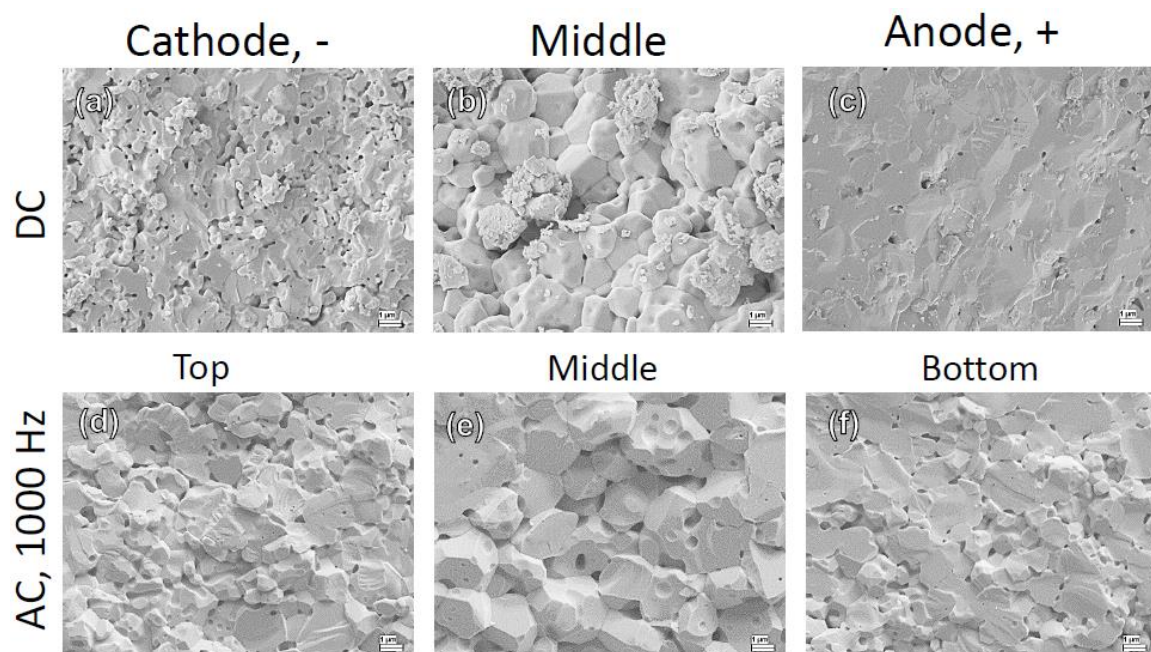
Figure 65: The SEM microstructural comparison of DC verses AC flash sintered specimens for the same current density (10 A/cm2) a same furnace temperature (900 °C).

6.1.5 Discussion

Beyond the application of electric field to densify a wide variety of ceramics (192), it is important to understand the response of individual types of ceramics to the electric field. While non-oxides can be sintered in Flash-SPS (FSPS) (233) due to their high electronic conductivity, insulators and dielectrics (such as alumina) need a high electric field due to their low electronic conductivity (43). Ceria has been chosen as an example of oxygen ionic conductors. Flash sintering of ceria, doped with various rare earth elements and composites (67, 69, 120, 125, 127), has already been investigated. However, to

understand flash behavior it is essential to dissociate the effect of extrinsic defect generation and pure ceria was investigated in this work. Ceria finds applications in solid oxide fuel cells (236-239), gas sensors (240) and as catalysts due to its high ionic conduction (229, 241). When ceria is heated to a high temperature, beyond 1200°C, it starts losing oxygen and becomes anion deficient (235) while retaining its fluorite structure. The fluorite structure, which has a simple cubic oxygen lattice and alternating body centers occupied by cations with eight coordination number (241), is commonly used as an electrolyte for fuel cells. Its chemical composition changes to CeO_{2-x} where $0<x<0.28$ and the lattice expands (235). This non-stoichiometry in ceria is a function of temperature and oxygen partial pressure. Charge neutrality is maintained by changing the oxygen state from Ce^{4+} to Ce^{3+} in order to accommodate anionic deficiency. In work by Deshpande (237), it was observed that a smaller particle size can also result in oxygen deficiency in response to the high surface strain in nanoparticles.

The flash specimen temperature for ceria has been noticeably close to conventional sintering temperature. With prolonged exposure to flash, ceria shows abnormally high lattice expansion at the anodic (positive) end. If this expansion were to be explained entirely by thermal expansion, then we estimate a temperature of above 2000 °C, however the microstructural evidences show smaller grain size at the anode. In addition, the effect is pronounced only when platinum paste is used. Also no such abnormal lattice expansion is seen under AC electric field. Since the anode is where oxygen picks up charge from negative electrode to go into the material, we believe platinum paste acts as a blocking electrode and limits the supply of oxygen. This creates non-stoichiometry and defect generation which results into reduction of Ce^{4+} to Ce^{3+} and lattice expansion (235), as

schematically shown in Fig. 67. Elemental mapping of oxygen (Fig. 64) suggest the migration of oxygen to the grain boundaries which acts as dominant charge carrier. Reversal of abnormal peak expansion direction indicates the role of non-stoichiometry, and possibly the reason for peak splitting by localized reduction. As ceria is reduced, the predominant method of conduction shifts from ionic to electronic, which reduces the effectiveness of flash sintering beyond a heating effect, which is still enough to densify ceria. This also points to the important role of ionic mobility and oxygen partial pressure for flash sintering of oxygen ion conductors and highlights the effectiveness of AC flash sintering for non-electronic conductors.
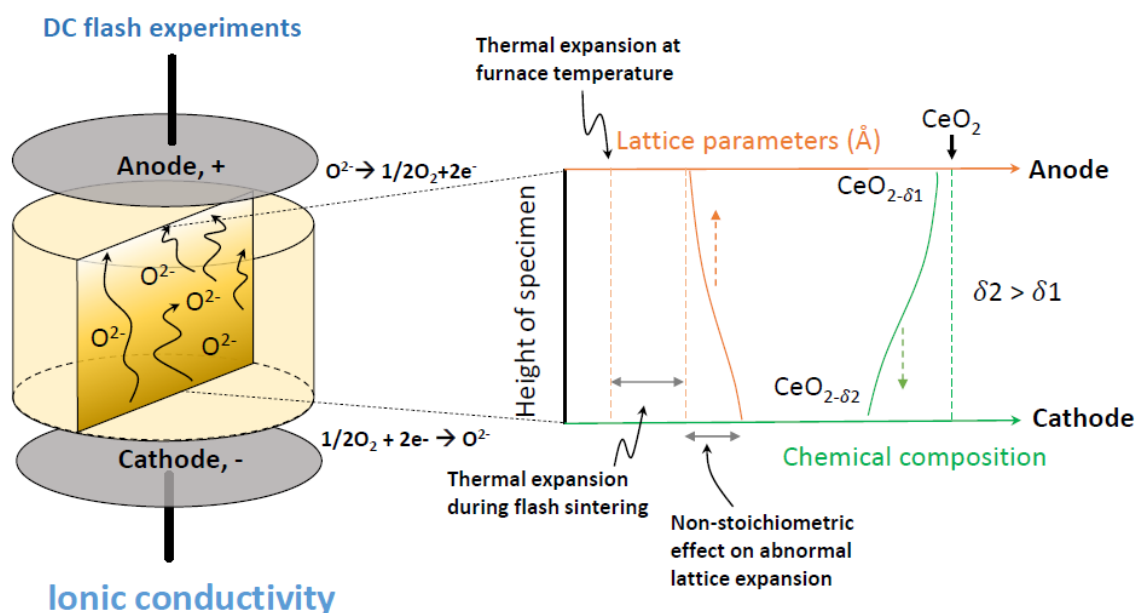
Figure 66: In response to the depleted oxygen at the anode, a chemical potential is developed and Ce^{4+} reduces to Ce^{3+}. This chemical potential hinders the sintering and results in porous microstructure. Higher lattice expansion, which normally suggests higher temperature, at the negative terminal (cathode) is relatively porous. The non-stoichiometry results in more electronic conduction on the anode side and hence less "flash" effect on densification, although since the temperature already reaching conventional sintering temperature.

7. Conclusions

7.1 Summary

A new technique utilizing EDXRD temperature calibration can be used to give an accurate measure of the temperature during flash. Based on the measured temperatures for ZnO, TiO$_2$, and CeO$_2$, a refined blackbody radiation model should be used in future works of non dogbone specimens. For dogbone specimens the greybody radiation model must be used without reverting to the assumption that emissivity, $\varepsilon = 1$. Serious effort must be put into estimating emissivity during flash as the emissivity may behave very differently due to the generation and annihilation of electron-hole pairs. For pellet specimens wedged between electrodes the addition of thermal conduction is necessary as thermal conduction causes significant overall cooling of the sample.

Infrared pyrometry will only give surface temperature measurements, which are significantly different from interior temperature measurements. A scaling of the surface temperature to interior temperature may be possible. Use of temperature approximations based on indirect data from other effects, such as thermal expansion of platinum, impedance spectroscopy, or the melting of platinum paste in reducing environment is not reliable.

In terms of the onset of flash, multiple feedback loops occur during flash sintering. Joule heating reaches a critical value that is higher than the heat released from thermal radiation. The conductivity of these ceramics increases as the temperature rises.

Densification lowers the specimen thickness so the same applied voltage divided by a smaller thickness causes greater applied electric field during flash.

Microstructural differences are dominated by temperature effects. The Peltier effect determines grain growth and sintering inhomogeneity of ZnO, and TiO_2 according to the established model. The rate of heating controls microstructure development in ZnO. Finally, CeO_2 grain growth and sintering inhomogeneity is determined by the Peltier effect rather than the observed lattice expansion caused by the change in stoichiometry. As an aside the temperature gradient across the specimen length caused by the Peltier effect can be eliminated by using an AC power supply which has a symmetric temperature profile and modest cooling at the ends due to thermal conduction.

The temperature during FS of oxide ceramics was shown to be comparable to CS temperatures. As a result sample overheating above conventional sintering is rejected for the test cases of ZnO, TiO_2, CeO_2. In order for Joule heating to be a sufficient condition for the sintering the rise in temperature would need to be significant, which is difficult to achieve due to heat loss from thermal radiation, conduction, convection, etc. The evidence of these large temperature changes are based on speculation, as with in situ thermometry, or a blackbody radiation model, where the inputs can be chosen as to support temperatures below the conventional sintering temperature or above the conventional sintering temperature depending on the desired result. The direct evidence from EDXRD does not support the claimed temperatures.

If the generation of a Frenkel defect avalanche is required to explain the enhanced densification due to the below conventional sintering temperature then there is a requirement of direct evidence that the FS temperature is below CS. However, all of the

temperature approximation methods used in support of this theory (infrared pyrometry, a blackbody radiation model, and in situ XRD calibration using synchrotron radiation) likely underestimate the specimen temperatures as explained in sections 2.5.1, 2.5.2, and 2.5.4. In addition, there is no direct evidence that metal cations have their mobility enhanced under the electric field. There is evidence that the diffusion of oxygen occurs (84, 97, 171), but this is to be expected in ionic ceramics of various ionic conductivities. As the metal cations are usually much larger than oxygen anions, the rate limiting step for sintering is the rate at which the metal cations fill in the pores.

While pore migration may seem a promising way of explaining the inhomogeneity in sintering at first, the effects can also be explained when considering differential heating. A high temperature will result in rapidly growing grain boundaries, which will tend to have irregular shapes compared to gradual sintering. In addition, regions with higher porosity can result from lower temperature with accompanying tendency to smaller grain size. The diffusion of pores over tens or even hundreds of microns seems implausible compared to much smaller diffusion distances from grain center to grain boundaries and pores or from grain boundaries to pores. Finally, preferential heating along the thickness from cathode to anode has also been observed directly in sections 4-6, which can also explain the microstructural inhomogeneity. The Peltier effect explains the microstructural inhomogeneity observed in 8YSZ better than pore migration as 8YSZ is a p-type semiconductor and higher temperature expected near the cathode, in reverse of effect seen in n-type ZnO, TiO_2, and CeO_2. Pore migration over tens of microns unlikely. Also the Peltier effect is directly observed in situ while pore migration is only speculated.

Local heating at the grain boundaries cannot be ruled out from the preceding experiments, but such a high temperature gradient for nano and submicron grains is implausible. The local heating may play a role during the power spike during stage II as temperature rises $>100°C \cdot s^{-1}$, which may be fast enough for the excess heat to avoid being distributed completely. Local melting at the grain boundaries is even less likely unlikely as it requires a several hundred degree temperature gradient.

Ultra-fast heating has been demonstrated to enhance densification by orders of magnitude for both 3YSZ (37) and ZnO (99) in a comparable manner to flash sintering. Fast firing is speculated to aid in the lowering of the sintering temperature with other FAST techniques, including SPS and microwave sintering as well.

7.2 Future Work

A number of future directions would be appropriate for continued study of the flash sintering mechanisms and behavior. In addition, flash sintering needs to move beyond exploration of the mechanisms and its inherent benefits over conventional sintering need to be utilized. The following is a list of proposed projects:

Temperature approximations and inhomogeneity of 3YSZ and 8YSZ, two of the most common materials studied in FS experiments, should be explored using EDXRD. 3YSZ and 8YSZ have been observed to have the reverse inhomogeneity in grain size, suggesting they act as mixed ionic conductors and p-type semiconductors. In addition, if the Peltier effect is acting on oxide ceramics then this will be noticeable in known p-type semiconductors such as Y_2O_3 (242-244) and other newly discovered p-type semiconductor compositions (245).

SrTiO$_3$ exhibits grain growth reduction by heating to higher dwell temperaturein the range of 1350°C-1400°C (246). By tuning the current density limit based on calculation of the temperature from the greybody radiation + thermal conduction model the ceramic can be sintered with minimal grain growth using flash.

Flash sintering of higher dielectric oxides such as Y$_2$O$_3$ (242-244, 247), ZrO$_2$ is not well studied. In addition, flash sintering needs to move beyond simple binary and ternary systems to find wide applications. Flash sintering of composites can be explored to study the effects of constrained sintering and diffusion kinetics, i.e. ZnO-TiO$_2$, ZrO$_2$-TiO$_2$, and BaTiO$_3$-SrTiO$_3$.

References

1.	Hulbert DM, Anders A, Dudina DV, Andersson J, Jiang D, Unuvar C, et al. The absence of plasma in "spark plasma sintering". Journal of Applied Physics. 2008;104(3):033305.

2.	Maizza G, Mastrorillo GD, Grasso S, Ning H, Reece MJ. Peltier effect during spark plasma sintering (SPS) of thermoelectric materials. Journal of Materials Science. 2017;52(17):10341-52.

3.	Becker A, Angst S, Schmitz A, Engenhorst M, Stoetzel J, Gautam D, et al. The effect of Peltier heat during current activated densification. Applied Physics Letters. 2012;101(1):013113.

4.	Guillon O, Gonzalez-Julian J, Dargatz B, Kessel T, Schierning G, Räthel J, et al. Field-Assisted Sintering Technology/Spark Plasma Sintering: Mechanisms, Materials, and Technology Developments. Advanced Engineering Materials. 2014;16(7):830-49.

5.	Agrawal D. Microwave Sintering of Ceramics, Composites and Metallic Materials, and Melting of Glasses. Transactions of the Indian Ceramic Society. 2006;65(3):129-44.

6.	Cologna M, Rashkova B, Raj R. Flash Sintering of Nanograin Zirconia in <5 s at 850°C. Journal of the American Ceramic Society. 2010;93(11):3556-9.

7.	Conrad H, Yang D. Influence of an applied dc electric field on the plastic deformation kinetics of oxide ceramics. Philosophical Magazine. 2010;90(9):1141-57.

8.	Yang D, Raj R, Conrad H. Enhanced Sintering Rate of Zirconia (3Y-TZP) Through the Effect of a Weak dc Electric Field on Grain Growth. Journal of the American Ceramic Society. 2010;93(10):2935-7.

9.	Conrad H, Chen IW. Space Charge and Grain Boundary Energy in Zirconia (3Y-TZP). Journal of the American Ceramic Society. 2011;94(11):3641-2.

10.	Yang D, Conrad H. Enhanced sintering rate and finer grain size in yttria-stablized zirconia (3Y-TZP) with combined DC electric field and increased heating rate. Materials Science and Engineering: A. 2011;528(3):1221-5.

11.	Pereira da Silva JG, Yamchelou AN, Debris A, Wieck C, Jelitto H, Al-Qureshi HA, et al. Mechanical strength and defect distributions in flash sintered 3YSZ. Journal of the European Ceramic Society. 2017;37(8):2901-5.

12.	Yadav D, Raj R. Two unique measurements related to flash experiments with yttria-stabilized zirconia. Journal of the American Ceramic Society. 2017;100(12):5374-8.

13.	Ghosh S, Chokshi AH, Lee P, Raj R. A Huge Effect of Weak dc Electrical Fields on Grain Growth in Zirconia. Journal of the American Ceramic Society. 2009;92(8):1856-9.

14.	Yang D, Conrad H. Enhanced sintering rate of zirconia (3Y-TZP) by application of a small AC electric field. Scripta Materialia. 2010;63(3):328-31.

15.	Cologna M, Raj R. Surface Diffusion-Controlled Neck Growth Kinetics in Early Stage Sintering of Zirconia, with and without Applied DC Electrical Field. Journal of the American Ceramic Society. 2011;94(2):391-5.

16.	Grasso S, Sakka Y, Rendtorff N, Hu C, Maizza G, Borodianska H, et al. Modeling of the temperature distribution of flash sintered zirconia. Journal of the Ceramic Society of Japan. 2011;119(1386):144-6.

17.   Francis JSC, Cologna M, Raj R. Particle size effects in flash sintering. Journal of the European Ceramic Society. 2012;32(12):3129-36.
18.   Francis JSC, Raj R, Chen IW. Flash-Sinterforging of Nanograin Zirconia: Field Assisted Sintering and Superplasticity. Journal of the American Ceramic Society. 2012;95(1):138-46.
19.   Obare J, Griffin WD, Conrad H. Effects of heating rate and DC electric field during sintering on the grain size distribution in fully sintered tetragonal zirconia polycrystals stabilized with 3% molar yttria (3Y-TZP). Journal of Materials Science. 2012;47(13):5141-7.
20.   Conrad H, Yang D. Effect of the strength of an AC electric field compared to DC on the sintering rate and related grain size of zirconia (3Y-TZP). Materials Science and Engineering: A. 2013;559:591-4.
21.   Francis JSC, Raj R, Halloran J. Influence of the Field and the Current Limit on Flash Sintering at Isothermal Furnace Temperatures. Journal of the American Ceramic Society. 2013;96(9):2754-8.
22.   M'Peko JC, Francis JSC, Raj R, Lupascu D. Impedance Spectroscopy and Dielectric Properties of Flash Versus Conventionally Sintered Yttria-Doped Zirconia Electroceramics Viewed at the Microstructural Level. Journal of the American Ceramic Society. 2013;96(12):3760-7.
23.   Wang J, Yang D, Conrad H. Transient-regime grain growth in nanocrystalline yttria-stabilized zirconia annealed without and with a DC electric field. Scripta Materialia. 2013;69(5):351-3.
24.   Conrad H, Wang J. Equivalence of AC and DC electric field on retarding grain growth in yttria-stabilized zirconia. Scripta Materialia. 2014;72-73:33-4.
25.   Lebrun J-M, Raj R, van der Biest O. A First Report of Photoemission in Experiments Related to Flash Sintering. Journal of the American Ceramic Society. 2014;97(8):2427-30.
26.   Caliman LB, Bichaud E, Soudant P, Gouvea D, Steil MC. A simple flash sintering setup under applied mechanical stress and controlled atmosphere. MethodsX. 2015;2:392-8.
27.   Lebrun J-M, Morrissey TG, Francis JSC, Seymour KC, Kriven WM, Raj R, et al. Emergence and Extinction of a New Phase During On-Off Experiments Related to Flash Sintering of 3YSZ. Journal of the American Ceramic Society. 2015;98(5):1493-7.
28.   Majidi H, van Benthem K. Consolidation of Partially Stabilized ZrO_{2} in the Presence of a Noncontacting Electric Field. Phys Rev Lett. 2015;114(19):195503.
29.   Terauds K, Lebrun J-M, Lee H-H, Jeon T-Y, Lee S-H, Je JH, et al. Electroluminescence and the measurement of temperature during Stage III of flash sintering experiments. Journal of the European Ceramic Society. 2015;35(11):3195-9.
30.   Todd RI, Zapata-Solvas E, Bonilla RS, Sneddon T, Wilshaw PR. Electrical characteristics of flash sintering: thermal runaway of Joule heating. Journal of the European Ceramic Society. 2015;35(6):1865-77.
31.   Jha SK, Terauds K, Lebrun J-M, Raj R. Beyond flash sintering in 3 mol % yttria stabilized zirconia. Journal of the Ceramic Society of Japan. 2016;124(4):283-8.
32.   Lebrun J-M, Jha SK, McCormack SJ, Kriven WM, Raj R, Chan H. Broadening of Diffraction Peak Widths and Temperature Nonuniformity During Flash Experiments. Journal of the American Ceramic Society. 2016;99(10):3429-34.

33.   Morisaki N, Yoshida H, Matsui K, Tokunaga T, Sasaki K, Yamamoto T. Synthesis of zirconium oxynitride in air under DC electric fields. Applied Physics Letters. 2016;109(8):083104.
34.   Qin W, Majidi H, Yun J, van Benthem K. Electrode Effects on Microstructure Formation During FLASH Sintering of Yttrium-Stabilized Zirconia. Journal of the American Ceramic Society. 2016;99(7):2253-9.
35.   Qin W, Yun J, Thron AM, van Benthem K. Temperature Gradient and Microstructure Evolution in AC Flash Sintering of 3 mol% YttriA-Stabilized Zirconia. Materials and Manufacturing Processes. 2016;32(5):549-56.
36.   Gao Y, Liu F, Liu D, Liu J, Wang Y, An L. Electrical-field induced nonlinear conductive behavior in dense zirconia ceramic. Journal of Materials Science & Technology. 2017;33(8):897-900.
37.   Ji W, Parker B, Falco S, Zhang JY, Fu ZY, Todd RI. Ultra-fast firing: Effect of heating rate on sintering of 3YSZ, with and without an electric field. Journal of the European Ceramic Society. 2017;37(6):2547-51.
38.   Liu D, Cao Y, Liu J, Gao Y, Wang Y. Effect of oxygen partial pressure on temperature for onset of flash sintering 3YSZ. Journal of the European Ceramic Society. 2018;38(2):817-20.
39.   Yoshida H, Sasaki Y. Low temperature and high strain rate superplastic flow in structural ceramics induced by strong electric-field. Scripta Materialia. 2018;146:173-7.
40.   Ren K, Wang Q, Lian Y, Wang Y. Densification kinetics of flash sintered 3mol% Y2O3 stabilized zirconia. Journal of Alloys and Compounds. 2018;747:1073-7.
41.   Yanhao D, Haoren W, I-Wei C. Electrical and hydrogen reduction enhances kinetics in doped zirconia and ceria: I. grain growth study. Journal of the American Ceramic Society. 2017;100(3):876-86.
42.   Carvalho S, Muccillo E, Muccillo R. Electrical Behavior and Microstructural Features of Electric Field-Assisted and Conventionally Sintered 3 mol% Yttria-Stabilized Zirconia. Ceramics. 2018;1(1):2.
43.   Cologna M, Francis JSC, Raj R. Field assisted and flash sintering of alumina and its relationship to conductivity and MgO-doping. Journal of the European Ceramic Society. 2011;31(15):2827-37.
44.   Biesuz M. Flash Sintering of Alumina Based Ceramics. Trento, Italy: University of Trento; 2017.
45.   Biesuz M, Luchi P, Quaranta A, Sglavo VM. Theoretical and phenomenological analogies between flash sintering and dielectric breakdown in α-alumina. Journal of Applied Physics. 2016;120(14):145107.
46.   Biesuz M, Sglavo VM. Flash sintering of alumina: Effect of different operating conditions on densification. Journal of the European Ceramic Society. 2016;36(10):2535-42.
47.   Biesuz M, Luchi P, Quaranta A, Martucci A, Sglavo VM. Photoemission during flash sintering: An interpretation based on thermal radiation. Journal of the European Ceramic Society. 2017;37(9):3125-30.
48.   Biesuz M, Sglavo VM. Current-induced abnormal and oriented grain growth in corundum upon flash sintering. Scripta Materialia. 2018;150:82-6.

49.	Cologna M, Prette ALG, Raj R. Flash-Sintering of Cubic Yttria-Stabilized Zirconia at 750°C for Possible Use in SOFC Manufacturing. Journal of the American Ceramic Society. 2011;94(2):316-9.

50.	Kim S-W, Kim SG, Jung J-I, Kang S-JL, Chen IW, Roedel J. Enhanced Grain Boundary Mobility in Yttria-Stabilized Cubic Zirconia under an Electric Current. Journal of the American Ceramic Society. 2011;94(12):4231-8.

51.	Muccillo R, Kleitz M, Muccillo ENS. Flash grain welding in yttria stabilized zirconia. Journal of the European Ceramic Society. 2011;31(8):1517-21.

52.	Akdoğan EK, Şavklıyıldız I, Biçer H, Paxton W, Toksoy F, Zhong Z, et al. Anomalous lattice expansion in yttria stabilized zirconia under simultaneous applied electric and thermal fields: A time-resolved in situ energy dispersive x-ray diffractometry study with an ultrahigh energy synchrotron probe. Journal of Applied Physics. 2013;113(23):233503.

53.	Downs JA, Sglavo VM, Raj R. Electric Field Assisted Sintering of Cubic Zirconia at 390°C. Journal of the American Ceramic Society. 2013;96(5):1342-4.

54.	Francis JSC, Cologna M, Montinaro D, Raj R, Wei WC. Flash Sintering of Anode-Electrolyte Multilayers for SOFC Applications. Journal of the American Ceramic Society. 2013;96(5):1352-4.

55.	Kim S-W, Kang S-JL, Chen IW, Lara-Curzio E. Electro-Sintering of Yttria-Stabilized Cubic Zirconia. Journal of the American Ceramic Society. 2013;96(5):1398-406.

56.	Park J, Chen IW, Clarke D. In SituThermometry Measuring Temperature Flashes Exceeding 1,700°C in 8 mol% Y2O3-Stablized Zirconia Under Constant-Voltage Heating. Journal of the American Ceramic Society. 2013;96(3):697-700.

57.	I.-Wei C, Seung-Wan K, Ju L, L. KSJ, Fuqiang H. Ionomigration of Neutral Phases in Ionic Conductors. Advanced Energy Materials. 2012;2(11):1383-9.

58.	Seung-Wan K, L. KSJ, I-Wei C. Ionomigration of Pores and Gas Bubbles in Yttria-Stabilized Cubic Zirconia. Journal of the American Ceramic Society. 2013;96(4):1090-8.

59.	Steil MC, Marinha D, Aman Y, Gomes JRC, Kleitz M. From conventional ac flash-sintering of YSZ to hyper-flash and double flash. Journal of the European Ceramic Society. 2013;33(11):2093-101.

60.	Muccillo R, Muccillo ENS. Shrinkage control of yttria-stabilized zirconia during ac electric field-assisted sintering. Journal of the European Ceramic Society. 2014;34(15):3871-7.

61.	Muccillo R, Muccillo ENS. Light emission during electric field-assisted sintering of electroceramics. Journal of the European Ceramic Society. 2015;35(5):1653-6.

62.	Pereira da Silva JG, Lebrun J-M, Al-Qureshi HA, Janssen R, Raj R, Olevsky E. Temperature Distributions During Flash Sintering of 8% Yttria-Stabilized Zirconia. Journal of the American Ceramic Society. 2015;98(11):3525-8.

63.	Du Y, Stevenson AJ, Vernat D, Diaz M, Marinha D. Estimating Joule heating and ionic conductivity during flash sintering of 8YSZ. Journal of the European Ceramic Society. 2016;36(3):749-59.

64.	Yadav D, Raj R. The onset of the flash transition in single crystals of cubic zirconia as a function of electric field and temperature. Scripta Materialia. 2017.

65.   Yanhao D, I-Wei C. Electrical and hydrogen reduction enhances kinetics in doped zirconia and ceria: II. Mapping electrode polarization and vacancy condensation in YSZ. Journal of the American Ceramic Society. 2018;101(3):1058-73.

66.   Prette ALG, Cologna M, Sglavo V, Raj R. Flash-sintering of Co2MnO4 spinel for solid oxide fuel cell applications. Journal of Power Sources. 2011;196(4):2061-5.

67.   Hao X, Liu Y, Wang Z, Qiao J, Sun K. A novel sintering method to obtain fully dense gadolinia doped ceria by applying a direct current. Journal of Power Sources. 2012;210:86-91.

68.   Gaur A, Sglavo VM, Olevsky E. Flash Sintering of (La, Sr)(Co, Fe)O3-Gd-Doped CeO2Composite. Journal of the American Ceramic Society. 2015;98(6):1747-52.

69.   Jiang T, Wang Z, Zhang J, Hao X, Rooney D, Liu Y, et al. Understanding the Flash Sintering of Rare-Earth-Doped Ceria for Solid Oxide Fuel Cell. Journal of the American Ceramic Society. 2015;98(6):1717-23.

70.   Karakuscu A, Cologna M, Yarotski D, Won J, Francis JSC, Raj R, et al. Defect Structure of Flash-Sintered Strontium Titanate. Journal of the American Ceramic Society. 2012;95(8):2531-6.

71.   Naik K, Jha SK, Raj R. Correlations between conductivity, electroluminescence and flash sintering. Scripta Materialia. 2016;118:1-4.

72.   Lemke F, Rheinheimer W, Hoffmann MJ. A comparison of power controlled flash sintering and conventional sintering of strontium titanate. Scripta Materialia. 2017;130(Supplement C):187-90.

73.   Muccillo R, Muccillo ENS, Kleitz M. Densification and enhancement of the grain boundary conductivity of gadolinium-doped barium cerate by ultra fast flash grain welding. Journal of the European Ceramic Society. 2012;32(10):2311-6.

74.   Zapata-Solvas E, Bonilla S, Wilshaw PR, Todd RI. Preliminary investigation of flash sintering of SiC. Journal of the European Ceramic Society. 2013;33(13-14):2811-6.

75.   Grasso S, Saunders T, Porwal H, Milsom B, Tudball A, Reece M. Flash Spark Plasma Sintering (FSPS) of α and β SiC. Journal of the American Ceramic Society. 2016;99(5):1534-43.

76.   Gaur A, Sglavo VM. Flash-sintering of MnCo2O4 and its relation to phase stability. Journal of the European Ceramic Society. 2014;34(10):2391-400.

77.   Gaur A, Mohiddon MA, Sglavo VM. Phenomenological understanding of flash sintering in MnCo2O4. Journal of the European Ceramic Society. 2018.

78.   Gaur A, Sglavo VM. Densification of La0.6Sr0.4Co0.2Fe0.8O3 ceramic by flash sintering at temperature less than 100 °C. Journal of Materials Science. 2014;49(18):6321-32.

79.   Jha SK, Raj R. The Effect of Electric Field on Sintering and Electrical Conductivity of Titania. Journal of the American Ceramic Society. 2014;97(2):527-34.

80.   Jha SK, Raj R. Electric Fields Obviate Constrained Sintering. Journal of the American Ceramic Society. 2014;97(10):3103-9.

81.   Pcheliakov DA, Yurlova MS, Grigoryev EG, Olevsky EA. Influence of Pressure in Flash Sintering Technique. Physics Procedia. 2015;72:374-7.

82.   Jha SK, Lebrun JM, Seymour KC, Kriven WM, Raj R. Electric field induced texture in titania during experiments related to flash sintering. Journal of the European Ceramic Society. 2016;36(1):257-61.

83.   Zhang Y, Nie J, Luo J. Effects of phase and doping on flash sintering of TiO$_2$. Journal of the Ceramic Society of Japan. 2016;124(4):296-300.
84.   Yoon B, Yadav D, Raj R, Sortino EP, Ghose S, Sarin P, et al. Measurement of O and Ti atom displacements in TiO2 during flash sintering experiments. Journal of the American Ceramic Society. 2018;101(5):1811-7.
85.   Shikhar F. A study on flash sintering and related phenomena in titania and its composite with alumina: University of Colorado, Boulder; 2015.
86.   Jha SK, Lebrun JM, Raj R. Phase transformation in the alumina–titania system during flash sintering experiments. Journal of the European Ceramic Society. 2016;36(3):733-9.
87.   M'Peko J-C, Francis JSC, Raj R. Field-assisted sintering of undoped BaTiO3: Microstructure evolution and dielectric permittivity. Journal of the European Ceramic Society. 2014;34(15):3655-60.
88.   Uehashi A, Sasaki K, Tokunaga T, Yoshida H, Yamamoto T. Formation of grain boundary second phase in BaTiO3 polycrystal under a high DC electric field at elevated temperature. Journal of the Ceramic Society of Japan. 2016;124(4):388-92.
89.   Nakagawa Y, Yoshida H, Uehashi A, Tokunaga T, Sasaki K, Yamamoto T. Electric current-controlled synthesis of BaTiO3. Journal of the American Ceramic Society. 2017;100(9):3843-50.
90.   Muccillo ENS, Muccillo R. Electric field-assisted sintering of tin dioxide with manganese dioxide addition. Journal of the European Ceramic Society. 2014;34(15):3699-706.
91.   Naik KS, Sglavo VM, Raj R. Flash sintering as a nucleation phenomenon and a model thereof. Journal of the European Ceramic Society. 2014;34(15):4063-7.
92.   Naik KS, Sglavo VM, Raj R. Field assisted sintering of ceramic constituted by alumina and yttria stabilized zirconia. Journal of the European Ceramic Society. 2014;34(10):2435-42.
93.   Bichaud E, Chaix JM, Carry C, Kleitz M, Steil MC. Flash sintering incubation in Al2O3/TZP composites. Journal of the European Ceramic Society. 2015;35(9):2587-92.
94.   Schmerbauch C, Gonzalez-Julian J, Röder R, Ronning C, Guillon O. Flash Sintering of Nanocrystalline Zinc Oxide and its Influence on Microstructure and Defect Formation. Journal of the American Ceramic Society. 2014;97(6):1728-35.
95.   Zhang Y, Jung J-I, Luo J. Thermal runaway, flash sintering and asymmetrical microstructural development of ZnO and ZnO–Bi2O3 under direct currents. Acta Materialia. 2015;94:87-100.
96.   Zhang Y, Luo J. Promoting the flash sintering of ZnO in reduced atmospheres to achieve nearly full densities at furnace temperatures of <120°C. Scripta Materialia. 2015;106:26-9.
97.   Gao H, Asel TJ, Cox JW, Zhang Y, Luo J, Brillson LJ. Native point defect formation in flash sintered ZnO studied by depth-resolved cathodoluminescence spectroscopy. Journal of Applied Physics. 2016;120(10):105302.
98.   Nie J, Zhang Y, Chan JM, Jiang S, Huang R, Luo J. Two-step flash sintering of ZnO: Fast densification with suppressed grain growth. Scripta Materialia. 2017;141:6-9.
99.   Zhang Y, Nie J, Chan JM, Luo J. Probing the densification mechanisms during flash sintering of ZnO. Acta Materialia. 2017;125:465-75.

100. Luo J. The scientific questions and technological opportunities of flash sintering: From a case study of ZnO to other ceramics. Scripta Materialia. 2018;146:260-6.

101. Nie J, Zhang Y, Chan JM, Huang R, Luo J. Water-assisted flash sintering: Flashing ZnO at room temperature to achieve ~98% density in seconds. Scripta Materialia. 2018;142:79-82.

102. Yoshida H, Sakka Y, Yamamoto T, Lebrun J-M, Raj R. Densification behaviour and microstructural development in undoped yttria prepared by flash-sintering. Journal of the European Ceramic Society. 2014;34(4):991-1000.

103. Caliman LB, Bouchet R, Gouvea D, Soudant P, Steil MC. Flash sintering of ionic conductors: The need of a reversible electrochemical reaction. Journal of the European Ceramic Society. 2016;36(5):1253-60.

104. Hao X, Han D, Wang J, Liu Y, Rooney D, Sun W, et al. Co-tape casting fabrication, field assistant sintering and evaluation of a coke resistant La0.2Sr0.7TiO3–Ni/YSZ functional gradient anode supported solid oxide fuel cell. International Journal of Hydrogen Energy. 2015;40(37):12790-7.

105. Rosenberger A, Gao Y, Stanciu L. Field-assisted sintering of Li1.3Al0.3Ti1.7(PO4)3 solid-state electrolyte. Solid State Ionics. 2015;278:217-21.

106. Shomrat N, Baltianski S, Randall CA, Tsur Y. Flash sintering of potassium-niobate. Journal of the European Ceramic Society. 2015;35(7):2209-13.

107. Corapcioglu G, Gulgun MA, Kisslinger K, Sturm S, Jha SK, Rishi R. Microstructure and microchemistry of flash sintered K0. 5Na0. 5NbO3. Journal of the Ceramic Society of Japan. 2016;124(4):P4-1-P4-.

108. Bajpai I, Han Y-H, Yun J, Francis J, Kim S, Raj R. Preliminary investigation of hydroxyapatite microstructures prepared by flash sintering. Advances in Applied Ceramics. 2016;115(5):276-81.

109. Jesus LM, Silva RS, Raj R, M'Peko J-C. Electric field-assisted ultrafast synthesis of nanopowders: a novel and cost-efficient approach. RSC Advances. 2016;6(109):107208-13.

110. Liu D, Gao Y, Liu J, Li K, Liu F, Wang Y, et al. SiC whisker reinforced ZrO2 composites prepared by flash-sintering. Journal of the European Ceramic Society. 2016;36(8):2051-5.

111. Liu D, Gao Y, Liu J, Liu F, Li K, Su H, et al. Preparation of Al2O3–Y3Al5O12–ZrO2 eutectic ceramic by flash sintering. Scripta Materialia. 2016;114:108-11.

112. Özdemir TE, Akdoğan EK, Şavklıyıldız İ, Biçer H, Örnek M, Zhong Z, et al. Electric field effect on chemical and phase equilibria in nano-TiB2–TiO2–TiBO3 system at <650 °C: an in situ time-resolved energy dispersive x-ray diffraction study with an ultrahigh energy synchrotron probe. Journal of Materials Research. 2016:1-13.

113. Yoshida H, Biswas P, Johnson R, Mohan MK. Flash-sintering of magnesium aluminate spinel (MgAl2O4) ceramics. Journal of the American Ceramic Society. 2016;100(2):554-62.

114. Sun K, Zhang J, Jiang T, Qiao J, Sun W, Rooney D, et al. Flash-Sintering and Characterization of La0.8Sr0.2Ga0.8Mg0.2O3-δ Electrolytes for Solid Oxide Fuel Cells. Electrochimica Acta. 2016;196:487-95.

115. Yoshida H, Morita K, Kim B-N, Sakka Y, Yamamoto T. Reduction in sintering temperature for flash-sintering of yttria by nickel cation-doping. Acta Materialia. 2016;106:344-52.

116.	Candelario VM, Moreno R, Todd RI, Ortiz AL. Liquid-phase assisted flash sintering of SiC from powder mixtures prepared by aqueous colloidal processing. Journal of the European Ceramic Society. 2017;37(2):485-98.

117.	Gil-Gonzalez E, Perejon A, Sanchez Jimenez P, Sayagues MJ, Raj R, Perez-Maqueda LA. PHASE-PURE BiFeO3 PRODUCED by REACTION FLASH-SINTERING of Bi2O3 and Fe2O3. Journal of Materials Chemistry A. 2017.

118.	Perez-Maqueda LA, Gil-Gonzalez E, Perejon A, Lebrun J-M, Sanchez-Jimenez PE, Raj R. Flash sintering of highly insulating nanostructured phase-pure BiFeO3. Journal of the American Ceramic Society. 2017;100:5.

119.	Morisaki N, Yoshida H, Tokunaga T, Sasaki K, Yamamoto T. Consolidation of undoped, monoclinic zirconia polycrystals by flash sintering. Journal of the American Ceramic Society. 2017;100(9):3851-7.

120.	Muccillo ENS, Carvalho SGM, Muccillo R. Electric field-assisted pressureless sintering of zirconia–scandia–ceria solid electrolytes. Journal of Materials Science. 2017.

121.	Raftery AM, Pereira da Silva JG, Byler DD, Andersson DA, Uberuaga BP, Stanek CR, et al. Onset conditions for flash sintering of UO2. Journal of Nuclear Materials. 2017;493:264-70.

122.	Valdez JA, Byler DD, Kardoulaki E, Francis JSC, McClellan KJ. Flash sintering of stoichiometric and hyper-stoichiometric urania. Journal of Nuclear Materials. 2018.

123.	David K, Krishn JS, Rishi R, L. MM. Flash sintering of a three-phase alumina, spinel, and yttria-stabilized zirconia composite. Journal of the American Ceramic Society. 2017;100(7):3262-8.

124.	Shomrat N, Baltianski S, Dor E, Tsur Y. The influence of doping on flash sintering conditions in SrTi1−xFexO3−δ. Journal of the European Ceramic Society. 2017;37(1):179-88.

125.	Spiridigliozzi L, Biesuz M, Dell'Agli G, Di Bartolomeo E, Zurlo F, Sglavo VM. Microstructural and electrical investigation of flash-sintered Gd/Sm-doped ceria. Journal of Materials Science. 2017:1-10.

126.	Frasnelli M, Sglavo VM. Flash sintering of tricalcium phosphate (TCP) bioceramics. Journal of the European Ceramic Society. 2018;38(1):279-85.

127.	Gaur A, Sglavo VM. Tuning the flash sintering characteristics of ceria with MnCo2O4. Materials Science and Engineering: B. 2018;228:160-6.

128.	Peiran S, Guoxing Q, Shikui C, Yijin K, Tao F, Chen X. An ultrafast synthesis method of LiNi1/3Co1/3Mn1/3O2 cathodes by flash/field-assisted sintering. Journal of the American Ceramic Society. 2018;0(0).

129.	Su X, Bai G, Jia Y, Wang Z, Wu W, Yan X, et al. Flash sintering of lead zirconate titanate (PZT) ceramics: Influence of electrical field and current limit on densification and grain growth. Journal of the European Ceramic Society. 2018.

130.	Zapata-Solvas E, Gomez-Garcia D, Dominguez-Rodriguez A, Todd RI. Ultra-fast and energy-efficient sintering of ceramics by electric current concentration. Sci Rep. 2015;5:8513.

131.	Dong Y, Chen IW. Thermal Runaway in Mold-Assisted Flash Sintering. Journal of the American Ceramic Society. 2016;99(9):2889-94.

132.	Grasso S, Kim E-Y, Saunders T, Yu M, Tudball A, Choi S-H, et al. Ultra-Rapid Crystal Growth of Textured SiC Using Flash Spark Plasma Sintering Route. Crystal Growth & Design. 2016;16(4):2317-21.

133.   Olevsky EA, Rolfing SM, Maximenko AL. Flash (Ultra-Rapid) Spark-Plasma Sintering of Silicon Carbide. Scientific Reports. 2016;6:33408.
134.   Niu B, Zhang F, Zhang J, Ji W, Wang W, Fu Z. Ultra-fast densification of boron carbide by flash spark plasma sintering. Scripta Materialia. 2016;116:127-30.
135.   Vasylkiv O, Borodianska H, Sakka Y, Demirskyi D. Flash spark plasma sintering of ultrafine yttria-stabilized zirconia ceramics. Scripta Materialia. 2016;121:32-6.
136.   Du B, Gucci F, Porwal H, Grasso S, Mahajan A, Reece M. Flash Spark Plasma Sintering of Magnesium Silicide Stannide with Improved Thermoelectric Properties. Journal of Materials Chemistry C. 2017.
137.   Manière C, Lee G, Olevsky EA. All-Materials-Inclusive Flash Spark Plasma Sintering. Scientific Reports. 2017;7(1):15071.
138.   McKinnon R, Grasso S, Tudball A, Reece MJ. Flash spark plasma sintering of cold-Pressed TiB2-hBN. Journal of the European Ceramic Society. 2017;37(8):2787-94.
139.   Yu M, Saunders T, Grasso S, Mahajan A, Zhang H, Reece MJ. Magnéli phase titanium suboxides by Flash Spark Plasma Sintering. Scripta Materialia. 2018;146:241-5.
140.   Wu J, Niu B, Zhang F, Lei L, Zhang J, Ren L, et al. Effect of titanium diboride on the homogeneity of boron carbide ceramic by flash spark plasma sintering. Ceramics International. 2018.
141.   Saunders T, Grasso S, Reece MJ. Ultrafast-Contactless Flash Sintering using Plasma Electrodes. Scientific Reports. 2016;6:27222.
142.   Wang C, Wu D, Grasso S, Saunders T, Castle E, Yan H, et al. Growth of SiC platelets using contactless flash technique. Journal of the Ceramic Society of Japan. 2016;124(9):845-7.
143.   L. JS, Ganesh V, T. HA. Flame-assisted flash sintering: A noncontact method to flash sinter coatings on conductive substrates. Journal of the American Ceramic Society. 2018;101(2):536-41.
144.   Hunt ATA, GA, US), Johnson, Stephen (Georgetown, KY, US), Venugopal, Ganesh (Johns Creek, GA, US), inventorFLAME-ASSISTED FLASH SINTERING. United States2015.
145.   Gonzalez-Julian J, Guillon O, Bordia R. Effect of Electric Field/Current on Liquid Phase Sintering. Journal of the American Ceramic Society. 2015;98(7):2018-27.
146.   Biesuz M, Sglavo VM. Liquid phase flash sintering in magnesia silicate glass-containing alumina. Journal of the European Ceramic Society. 2017;37(2):705-13.
147.   McLaren C, Heffner W, Tessarollo R, Raj R, Jain H. Electric field-induced softening of alkali silicate glasses. Applied Physics Letters. 2015;107(18):184101.
148.   Pinter L, Biesuz M, Sglavo VM, Saunders T, Binner J, Reece M, et al. DC-electro softening in soda lime silicate glass: An electro-thermal analysis. Scripta Materialia. 2018;151:14-8.
149.   Brehane TB, Byoungjin S, Jong H. Electric field assisted precipitation of lead selenide quantum dots in borosilicate glass. Journal of the American Ceramic Society. 2018;0(ja).
150.   T. MC, R. HW, Rishi R, Himanshu J. AC electric field-induced softening of alkali silicate glasses. Journal of the American Ceramic Society. 2018;101(6):2277-86.
151.   Dong Y, Chen IW, Gaukler L. Predicting the Onset of Flash Sintering. Journal of the American Ceramic Society. 2015;98(8):2333-5.

152.   Dong Y, Chen IW, Guillon O. Onset Criterion for Flash Sintering. Journal of the American Ceramic Society. 2015;98(12):3624-7.
153.   Hewitt IJ, Lacey AA, Todd RI. A Mathematical Model for Flash Sintering. Math Model Nat Phenom. 2015;10(6):77-89.
154.   Barsoum M, Barsoum MW. Fundamentals of Ceramics: CRC Press; 2002.
155.   Raj R. Joule heating during flash-sintering. Journal of the European Ceramic Society. 2012;32(10):2293-301.
156.   Narayan J. A new mechanism for field-assisted processing and flash sintering of materials. Scripta Materialia. 2013;69(2):107-11.
157.   Chaim R. Liquid Film Capillary Mechanism for Densification of Ceramic Powders during Flash Sintering. Materials. 2016;9(4):280.
158.   Chaim R. Particle Surface Softening as Universal Behaviour during Flash Sintering of Oxide Nano-Powders. Materials. 2017;10(2):179.
159.   Olorunyolemi T, Birnboim A, Carmel Y, Wilson OC, Lloyd IK, Smith S, et al. Thermal Conductivity of Zinc Oxide: From Green to Sintered State. Journal of the American Ceramic Society. 2002;85(5):1249-53.
160.   Gupta TK, Coble RL. Sintering of ZnO: I, Densification and Grain Growth*. Journal of the American Ceramic Society. 1968;51(9):521-5.
161.   Robie RA, Haselton HT, Hemingway BS. Heat capacities and entropies at 298.15 K of $MgTiO_3$ (geikielite), ZnO (zincite), and $ZnCO_3$ (smithsonite). The Journal of Chemical Thermodynamics. 1989;21(7):743-9.
162.   (Ed.) JFS, (Ed.) WA. CRC Materials Science and Engineering Handbook, Third Edition. Boca Raton: CRC Press; 2000.
163.   Heat capacities and thermodynamic functions of TiO_2 anatase and rutile: Analysis of phase stability. American Mineralogist. 2009;94(2-3):236-43.
164.   Wan C, Motohashi Y, Shibata T, Baba S, Ishihara M, Hoshiya T. Thermal Conductivity of Superplastically Deformed 3Y-TZP. MATERIALS TRANSACTIONS. 2002;43(10):2473-9.
165.   Song X, Xie M, Zhou F, Jia G, Hao X, An S. High-temperature thermal properties of yttria fully stabilized zirconia ceramics. Journal of Rare Earths. 2011;29(2):155-9.
166.   Gómez SY, da Silva AL, Gouvêa D, Castro RHR, Hotza D. Nanocrystalline yttria-doped zirconia sintered by fast firing. Materials Letters. 2016;166:196-200.
167.   Gómez SY, Farzan F, Castro RHC, Hotza D. Modeling Densification during Fast Firing of Yttria-Stabilized Zirconia. Processing, Properties, and Design of Advanced Ceramics and Composites: John Wiley & Sons, Inc.; 2016. p. 153-8.
168.   Zhang J, Meng F, Todd RI, Fu Z. The nature of grain boundaries in alumina fabricated by fast sintering. Scripta Materialia. 2010;62(9):658-61.
169.   Charalambous H, Jha SK, Wang H, Phuah XL, Okasinski J, Wang H, et al. In situ measurement of temperature and reduction of rutile titania using energy dispersive x-ray diffraction. Ceramics International. under review.
170.   Charalambous H, Jha SK, Lay RT, Cabales A, Okasinski J, Tsakalakos T. Investigation of temperature approximation methods during flash sintering of ZnO. Ceramics International. 2018;44(6):6162-9.
171.   Jha SK, Charalambous H, Wang H, Phuah XL, Mead C, Okasinski J, et al. In-situ observation of oxygen mobility and abnormal lattice expansion in ceria during flash sintering. Ceramics International. 2018.

172.   Perez-Maqueda LA, Gil-Gonzalez E, Wassel MA, Jha SK, Perejon A, Charalambous H, et al. Insight into the BiFeO 3 flash sintering process by in-situ energy dispersive X-ray diffraction (ED-XRD). Ceramics International. under review.

173.   Lebrun JM, Hellberg CS, Jha SK, Kriven WM, Steveson A, Seymour KC, et al. In-situ measurements of lattice expansion related to defect generation during flash sintering. Journal of the American Ceramic Society. 2017;100(11):4965-70.

174.   Hahn TA, Kirby RK. Thermal Expansion of Platinum from 293 to 1900 K. AIP Conference Proceedings. 1972;3(1):87-95.

175.   Charalambous H, Jha SK, Christian KH, Lay RT, Tsakalakos T. Flash Sintering using Controlled Current Ramp. Journal of the European Ceramic Society. 2018;38(10):3689-93.

176.   Charalambous H, Jha SK, Wang H, Phuah XL, Wang H, Tsakalakos T. Inhomogeneous reduction and its relation to grain growth of titania during flash sintering. Scripta Materialia. 2018;155:37-40.

177.   Kok D, Jha SK, Raj R, Mecartney M. Flash Sintering of a Three-Phase Alumina, Spinel and Yttria-Stabilized Zirconia Composite. Journal of American Ceramic Society. 2017;Accepted.

178.   Liu D, Cao Y, Liu J, Gao Y, Wang Y. Effect of oxygen partial pressure on temperature for onset of flash sintering 3YSZ. Journal of the European Ceramic Society. 2017.

179.   Muccillo R, Muccillo ENS. Electric field-assisted flash sintering of tin dioxide. Journal of the European Ceramic Society. 2014;34(4):915-23.

180.   Emanuele S, Jean-Marie L, Andrea S, Rishi R. Continuous flash sintering. Journal of the American Ceramic Society. 2018;101(4):1432-40.

181.   Advanced Photon Source [cited 2018. Available from: https://www.anl.gov/photos/advanced-photon-source.

182.   Özgür Ü, Alivov YI, Liu C, Teke A, Reshchikov MA, Doğan S, et al. A comprehensive review of ZnO materials and devices. Journal of Applied Physics. 2005;98(4):041301.

183.   Carotta MC, Cervi A, di Natale V, Gherardi S, Giberti A, Guidi V, et al. ZnO gas sensors: A comparison between nanoparticles and nanotetrapods-based thick films. Sensors and Actuators B: Chemical. 2009;137(1):164-9.

184.   Gupta TK. Application of Zinc Oxide Varistors. Journal of the American Ceramic Society. 1990;73(7):1817-40.

185.   Gupta TK, Coble RL. Sintering of ZnO: II, Density Decrease and Pore Growth During the Final Stage of the Process*. Journal of the American Ceramic Society. 1968;51(9):525-8.

186.   Dey D, Bradt RC. Grain Growth of ZnO during Bi2O3 Liquid-Phase Sintering. Journal of the American Ceramic Society. 1992;75(9):2529-34.

187.   Mazaheri M, Zahedi AM, Sadrnezhaad SK. Two-Step Sintering of Nanocrystalline ZnO Compacts: Effect of Temperature on Densification and Grain Growth. Journal of the American Ceramic Society. 2008;91(1):56-63.

188.   Moriyoshi Y, Komatsu W. Kinetics of Initial Sintering with Grain Growth. Journal of the American Ceramic Society. 1970;53(12):671-5.

189.   Yu M, Grasso S, McKinnon R, Saunders T, Reece MJ. Review of flash sintering: materials, mechanisms and modelling. Advances in Applied Ceramics. 2016:1-37.

190.   Agarwal G, Speyer RF, Hackenberger WS. Microstructural development of ZnO using a rate-controlled sintering dilatometer. Journal of Materials Research. 2011;11(3):671-9.

191.   Holland TB, Anselmi-Tamburini U, Quach DV, Tran TB, Mukherjee AK. Effects of local Joule heating during the field assisted sintering of ionic ceramics. Journal of the European Ceramic Society. 2012;32(14):3667-74.

192.   Raj R. Analysis of the Power Density at the Onset of Flash Sintering. Journal of the American Ceramic Society. 2016.

193.   Downs JA. <Thesis Downs_Mechanisms_of_Flash_Sintering.pdf> 2013.

194.   Todd RI. Flash Sintering of Ceramics: A Short Review. In: Lee B, Gadow R, Mitic V, editors. Proceedings of the IV Advanced Ceramics and Applications Conference. Paris: Atlantis Press; 2017. p. 1-12.

195.   Takahashi K, Yoshikawa A, Sandhu A. Wide bandgap semiconductors : fundamental properties and modern photonic and electronic devices. Berlin ; London: Springer; 2007. xxv, 460 p. p.

196.   Zinc oxide (ZnO) crystal structure, lattice parameters. In: Madelung O, Rössler U, Schulz M, editors. II-VI and I-VII Compounds; Semimagnetic Compounds. Berlin, Heidelberg: Springer Berlin Heidelberg; 1999. p. 1-5.

197.   Senda T, Bradt RC. Grain Growth in Sintered ZnO and ZnO-Bi2O3 Ceramics. Journal of the American Ceramic Society. 1990;73(1):106-14.

198.   Han J, Mantas PQ, Senos AMR. Grain growth in Mn-doped ZnO. Journal of the European Ceramic Society. 2000;20(16):2753-8.

199.   Roberts JP, Wheeler C. Diffusion of zinc in polycrystalline zinc oxide. Transactions of the Faraday Society. 1960;56(0):570-80.

200.   Norris LF, Parravano G. Sintering of Zinc Oxide. Journal of the American Ceramic Society. 1963;46(9):449-52.

201.   Lott K, Shinkarenko S, Kirsanova T, Türn L, Gorohova E, Grebennik A, et al. Zinc nonstoichiometry in ZnO. Solid State Ionics. 2004;173(1):29-33.

202.   Erhart P, Albe K. Diffusion of zinc vacancies and interstitials in zinc oxide. Applied Physics Letters. 2006;88(20):201918.

203.   Roy TK, Bhowmick D, Sanyal D, Chakrabarti A. Sintering studies of nano-crystalline zinc oxide. Ceramics International. 2008;34(1):81-7.

204.   Huang G-Y, Wang C-Y, Wang J-T. First-principles study of diffusion of zinc vacancies and interstitials in ZnO. Solid State Communications. 2009;149(5):199-204.

205.   Dargatz B, Gonzalez-Julian J, Bram M, Jakes P, Besmehn A, Schade L, et al. FAST/SPS sintering of nanocrystalline zinc oxide—Part I: Enhanced densification and formation of hydrogen-related defects in presence of adsorbed water. Journal of the European Ceramic Society. 2016;36(5):1207-20.

206.   Dargatz B, Gonzalez-Julian J, Bram M, Shinoda Y, Wakai F, Guillon O. FAST/SPS sintering of nanocrystalline zinc oxide—Part II: Abnormal grain growth, texture and grain anisotropy. Journal of the European Ceramic Society. 2016;36(5):1221-32.

207.   Kim S, Maier J. Electrical Properties of ZnO: Nanocrystalline vs. Microcrystalline Ceramics. Electrochemical and Solid-State Letters. 2003;6(11):J7-J9.

208.   Sedghi A, Riyahi Noori N. Comparison of electrical properties of zinc oxide varistors manufactured from micro and nano ZnO powder2011. 752-5 p.

209. Cho J, Li Q, Wang H, Fan Z, Li J, Xue S, et al. High temperature deformability of ductile flash-sintered ceramics via in-situ compression. Nature Communications. 2018;9(1):2063.

210. Wang H, Phuah X, Li J, Holland TB, Li Q, Hellberg CS, et al. Key microstructural characteristics in flash sintered 3YSZ critical for enhanced sintering process. Journal of the American Ceramic Society. in preparation.

211. Raj R, Cologna M, Francis JSC, Green DJ. Influence of Externally Imposed and Internally Generated Electrical Fields on Grain Growth, Diffusional Creep, Sintering and Related Phenomena in Ceramics. Journal of the American Ceramic Society. 2011;94(7):1941-65.

212. Jha S, Terauds K, Lebrun J-M, Raj R. Beyond flash sintering in 3 mol % yttria stabilized zirconia2016. 283-8 p.

213. SAKARCAN M, HSUEH CH, EVANS AG. Experimental Assessment of Pore Breakaway During Sintering. Journal of the American Ceramic Society. 1983;66(6):456-61.

214. Balachandran U, Eror NG. Raman spectra of titanium dioxide. Journal of Solid State Chemistry. 1982;42(3):276-82.

215. Li J, Li F, Li C, Yang G, Xu Z, Zhang S. Evidences of grain boundary capacitance effect on the colossal dielectric permittivity in (Nb + In) co-doped TiO2 ceramics. Scientific Reports. 2015;5:8295.

216. Frank O, Zukalova M, Laskova B, Kurti J, Koltai J, Kavan L. Raman spectra of titanium dioxide (anatase, rutile) with identified oxygen isotopes (16, 17, 18). Physical Chemistry Chemical Physics. 2012;14(42):14567-72.

217. Yang C, Wang Z, Lin T, Yin H, Lü X, Wan D, et al. Core-Shell Nanostructured "Black" Rutile Titania as Excellent Catalyst for Hydrogen Production Enhanced by Sulfur Doping. Journal of the American Chemical Society. 2013;135(47):17831-8.

218. Sang-Joon P, Jeong-Pyo L, Jong Shik J, Hyun R, Hyunung Y, Byung Youn Y, et al. In situ control of oxygen vacancies in TiO 2 by atomic layer deposition for resistive switching devices. Nanotechnology. 2013;24(29):295202.

219. Yan J, Wu G, Guan N, Li L, Li Z, Cao X. Understanding the effect of surface/bulk defects on the photocatalytic activity of TiO2: anatase versus rutile. Physical Chemistry Chemical Physics. 2013;15(26):10978-88.

220. Bharti B, Kumar S, Lee H-N, Kumar R. Formation of oxygen vacancies and Ti3+ state in TiO2 thin film and enhanced optical properties by air plasma treatment. Scientific Reports. 2016;6:32355.

221. Kang Q, Cao J, Zhang Y, Liu L, Xu H, Ye J. Reduced TiO2 nanotube arrays for photoelectrochemical water splitting. Journal of Materials Chemistry A. 2013;1(18):5766-74.

222. Guo X, Ding Y. Grain Boundary Space Charge Effect in Zirconia: Experimental Evidence. Journal of The Electrochemical Society. 2004;151(1):J1-J7.

223. Goldsmid HJ. The Seebeck and Peltier effects. 2017. In: The Physics of Thermoelectric Energy Conversion [Internet]. Morgan & Claypool Publishers; [1---3]. Available from: http://dx.doi.org/10.1088/978-1-6817-4641-8ch1.

224. Cardarelli F. Miscellaneous Electrical Materials. Materials Handbook: A Concise Desktop Reference. London: Springer London; 2008. p. 543-91.

225.   Liu H, Ma H, Su T, Zhang Y, Sun B, Liu B, et al. High-thermoelectric performance of TiO2-x fabricated under high pressure at high temperatures. Journal of Materiomics. 2017;3(4):286-92.

226.   Yu M, Grasso S, McKinnon R, Saunders T, Reece MJ. Review of flash sintering: materials, mechanisms and modelling. Advances in Applied Ceramics. 2017;116(1):24-60.

227.   Shannon R. Revised effective ionic radii and systematic studies of interatomic distances in halides and chalcogenides. Acta Crystallographica Section A. 1976;32(5):751-67.

228.   Rufner JF, Kaseman D, Castro RHR, van Benthem K. DC Electric Field-Enhanced Grain-Boundary Mobility in Magnesium Aluminate During Annealing. Journal of the American Ceramic Society. 2016;99(6):1951-9.

229.   Sato K. Grain-Boundary Structures Associated with Ionic Transport in Gd-Doped Ceria Nanostructured Electrolyte. The Journal of Physical Chemistry C. 2015;119(10):5734-8.

230.   Narayan J. Grain growth model for electric field-assisted processing and flash sintering of materials. Scripta Materialia. 2013;68(10):785-8.

231.   Chen K, Jiao Y, Zhao Y, Gao Y, Zhang X, An L. Non-contact electric field-enhanced abnormal grain growth in (K0.5Na0.5)NbO3 ceramics. Ceramics International. 2017;43(15):12343-7.

232.   Raj R, Ramanathan S. Flash transition as a possible origin for low open circuit voltage in thin film solid oxide fuel cells. Journal of Power Sources. 2017;359:48-51.

233.   Grasso S, Saunders T, Porwal H, Cedillos-Barraza O, Jayaseelan DD, Lee WE, et al. Flash Spark Plasma Sintering (FSPS) of Pure ZrB2. Journal of the American Ceramic Society. 2014;97(8):2405-8.

234.   Lebrun J-M, Jha SK, Naik KS, Seymour KC, Kriven WM, Raj R, et al. The Change of X-ray Diffraction Peak Width Duringin situConventional Sintering of Nanoscale Powders. Journal of the American Ceramic Society. 2016;99(3):765-8.

235.   Yashima M, Kobayashi S, Yasui T. Crystal structure and the structural disorder of ceria from 40 to 1497 °C. Solid State Ionics. 2006;177(3):211-5.

236.   Cassidy M. Trends in the processing and manufacture of solid oxide fuel cells. Wiley Interdisciplinary Reviews: Energy and Environment. 2017;6(5):e248-n/a.

237.   Cho S, Yoon J, Kim J-H, Zhang X, Manthiram A, Wang H. Microstructural and electrical properties of Ce0.9Gd0.1O1.95 thin-film electrolyte in solid-oxide fuel cells. Journal of Materials Research. 2011;26(7):854-9.

238.   Liu Z, Ding D, Liu M, Ding X, Chen D, Li X, et al. High-performance, ceria-based solid oxide fuel cells fabricated at low temperatures. Journal of Power Sources. 2013;241(Supplement C):454-9.

239.   Zha S, Xia C, Meng G. Effect of Gd (Sm) doping on properties of ceria electrolyte for solid oxide fuel cells. Journal of Power Sources. 2003;115(1):44-8.

240.   Jasinski P, Suzuki T, Anderson HU. Nanocrystalline undoped ceria oxygen sensor. Sensors and Actuators B: Chemical. 2003;95(1):73-7.

241.   Skinner SJ, Kilner JA. Oxygen ion conductors. Materials Today. 2003;6(3):30-7.

242.   Schieltz J, Patterson JW, Wilder DR. Electrolytic Behavior of Yttria. Journal of The Electrochemical Society. 1971;118(7):1140-4.

243.   TRULS N, PER K. Electrical Conductivity and Defect Structure of Y2O3 as a Function of Water Vapor Pressure. Journal of the American Ceramic Society. 1984;67(12):786-92.
244.   TRULS N, PER K. Direct-Current Conductivity of Y2O3 as a Function of Water Vapor Pressure. Journal of the American Ceramic Society. 1986;69(11):780-3.
245.   Zhenwei W, K. NP, A. CFJ, N. AH. Recent Developments in p-Type Oxide Semiconductor Materials and Devices. Advanced Materials. 2016;28(20):3831-92.
246.   Kelly MN, Rheinheimer W, Hoffmann MJ, Rohrer GS. Anti-thermal grain growth in SrTiO3: Coupled reduction of the grain boundary energy and grain growth rate constant. Acta Materialia. 2018;149:11-8.
247.   M. TN, W. VR. Electrical Properties and Defect Structure of Y2O3. Journal of the American Ceramic Society. 1966;49(8):401-4.